DEVELOPMENT AND PERFORMANCE EVALUATION OF AEROSOL PARTICLE MASS ANALYZER (APM)
(エアロゾル質量分級装置（APM）の開発と性能評価)

By
NAOKO TAJIMA
(NAOKO HATASHITA)

HIROSHIMA UNIVERSITY
SEPTEMBER 2013

DEVELOPMENT AND PERFORMANCE EVALUATION OF AEROSOL PARTICLE MASS ANALYZER (APM)
(エアロゾル質量分級装置（APM）の開発と性能評価)

A Thesis submitted to
The Department of Chemical Engineering
Graduate School of Engineering
Hiroshima University

By
NAOKO TAJIMA
(NAOKO HATASHITA)

In Partial Fulfillment of the Requirements
For the Degree of
Doctor of Engineering

Hiroshima University
September 2013

Approved by

Professor Kikuo Okuyama
Advisor

Abstract

The objective of this doctoral thesis is to develop the aerosol particle mass analyzer (APM) as well as to evaluate its performance. Two types of APM, which use a new method for classifying the aerosol particles by using a balance of centrifugal force and electrostatic force, were developed and their classification performances were carefully evaluated. The application as aerosol measurement instrument for nanoparticle physical properties was also studied. The major points of this thesis are as follows:

Chapter 1 describes the background of aerosol measurement, types of aerosol centrifuge and their principle, and includes technological advance for APM. Objective and outline of thesis are also described.

Chapter 2 describes the appropriate mass range and operating conditions for the first commercial instrument, Model 3600 APM (Kanomax Japan Inc.) to maximize the mass classification performance. Limiting factor of the APM, which were constraints of the rotation speed and the voltage, as well as requirements on the APM classification performance parameter, λ, that guarantee at least minimal performance in both resolution and penetration were also explained here. The operation diagram of APM, which is a tool to visualize the limits and mass range was introduced. In this study, APM was proposed to operate at the λ value within the range of 0.25–0.5 for optimum classification performance by balancing both resolution and penetration. The mass range for the APM, with the λ value maintained between 0.25 and 0.5, was calculated to be from 0.003 to 2000 fg, which corresponds to the diameter range from 20 to 1600 nm for the density of 1 g/cm^3. To verify the validity of the mass range and the idea of the optimized operation, experiments on an APM with polystyrene and sodium-chloride particles that were classified by electrical mobility were conducted. It was found that the APM was able to provide bell-shaped spectra down to 12 nm, and was able to perform mass classification with an accuracy better than 5 % down to 50 nm.

Underestimation of mass and reduction of resolution and penetration were observed at particle with size smaller than 30 nm.

Chapter 3 describes design and performance evaluation of the compact APM, which is the second commercial instrument. The size of Model 3600 APM is large. Therefore, it is not suitable for field measurements. We have developed an APM which is compact and more suitable for field measurements application compared to that of Model 3600 APM. Necessary parameters for the required performance in classifying particle mass were set first. Then, theoretical framework for the design parameters of an APM that satisfy the parameters was formulated. Finally, the design parameters that satisfy the condition were determined while reducing the instrument size. The necessary parameters include the classification range from 0.001 fg to 1000 fg (The size of spherical particles is about 12–1200 nm and having density of 1 g/cm^3), and the condition that both the classification resolution and particle penetration in this mass range are high enough. A prototype having the design parameters determined according to this theoretical framework was constructed, and its performance was evaluated experimentally. The external dimensions of the electrodes of the compact APM are approximately 140 mm in length and 60 mm in diameter. It was confirmed that the performance of the compact APM operated at the aerosol flow rate of 0.3 L/min was comparable to that of the Model 3600 APM operated at 1 L/min. Because of the reduced size and of the resultant improved portability, it is expected that the compact APM is readily applicable for field measurements.

Chapter 4 introduces an example of measurement of the effective density and porosity of nanoparticle agglomerates as the application of APM. Installation of APM and differential mobility analyzer (DMA) as a series system, called DMA-APM system, has been developed to obtain an in situ aerosol measurement technology for nanoparticle physical properties. This study evaluated the influence of formic acid on the electrochemical properties of high porosity titanium nitride supported platinum (Pt/TiN) nanoparticle aggregates synthesised via self-assembly assisted spray pyrolysis.

The effective density of TiN nanoparticle aggregates prepared via this method was measured using a DMA-APM system. The porosity of nanoparticle agglomerates was calculated from the effective density.

Chapter 5 summarizes the development of two types of APM and their performance.

Contents

List of Tables

List of Figures

Chapter 1

Introduction

1.1. Background

1.1.1. Aerosol properties

The microscopic particles that float in the air are of many kinds: yellow dust, diesel particulate matter (DPM), PM2.5, pollen, and viruses. They affect our health and quality of life. These airborne particles are all examples of aerosols. An aerosol is defined in its simplest form as solid or liquid particles suspended in a gas. Aerosols are usually stable for at least a few seconds and in some cases, it may last a year or more. The aerosol includes both, the particles and the suspending gas, which is usually air. Particle size ranges from 0.001 to over 100 μm. Aerosols can be subdivided according to the physical form of the particles and their method of generation.

Dust: A solid-particle aerosol formed by mechanical disintegration of a parent material, such as by crushing or grinding. The range size of particles is from sub-micrometer to visible.

Fume: A solid-particle aerosol produced by condensation of vapors or gaseous combustion products. Particle size is generally less than 1 μm.

Smoke: A visible aerosol resulting from incomplete combustion. Particles may be solid or liquid and are usually less than 1 μm in diameter.

Mist: A liquid-particle aerosol formed by condensation or atomization. Particle size ranges from sub-micrometer to about 20 μm.

Fog: A visible mist.

Smog: Photochemical reaction products, usually combined with water vapor. Particle sizes are generally less than 1 or 2 μm.

Cloud: A very dense or concentrated suspension of particles in air, often with a well-defined boundary at a macroscopic length scale.

Bio-aerosol: An aerosol of biological origin, including airborne suspension of viruses, pollen, bacteria, and fungal spores, and their fragments.

***Spray*:** Droplet aerosol formed by mechanical or electrostatic breakup of a liquid.

An understanding of the properties of aerosols is of great practical importance. It enables us to measure and control particulate pollutants in the atmosphere and in the occupational and general environments. Articles on the techniques and importance of particle size distribution measurements have been published since around 1900. Regulations and standards in Japan, such as "Ordinance on prevention of health impairment due to asbestos" (Ministry of Health, Labor and Welfare, 2005) and adding particulate matter less than 2.5 μm in diameter PM2.5 to "Environmental quality standards regarding air pollution" (Ministry of the Environment, 2009), have been newly publicized. The development of measurement methods and instruments has been required to address the above purposes. With the discovery of nanotechnology, aerosol measurement techniques are not only required on functional production of nanomaterials, but also to minimize risks from their environmental or occupational exposure. Aerosol technology is used in a various fields including industrial hygiene, air pollution, atmospheric science, material science, powder technology, nanotechnology, filtration, and drug delivery. Understanding the properties of aerosols is a big step for the measurement and control of aerosols and is important in a wide range of fields.

Particle size is the most important parameter for characterizing the behavior of aerosols. All properties of aerosols depend on particle size. Generally, dusts, ground material, and pollen are in the micrometer range or larger, and fumes and smokes are sub-micrometer in size or less. The smallest aerosol particles are having an almost similar size as large gas molecules and so do many of their properties. Usually, liquid aerosol particles are nearly spherical, while solid aerosol particles are having a complex shapes. In the theory of aerosol properties, it is usually necessary to assume that the particles are spherical. Correction factors for equivalent diameter are necessary to apply these theories to non-spherical particles. An equivalent diameter is the diameter of the sphere that would have the same value of a particular physical property as that of the irregular particle. Starting with describing aerosol properties, behavior, and relevant equivalent diameters that commonly used, some kinds of measurement technique are finally could be introduced for the background.

The drag force F_{D} on a spherical particle due to its velocity v relative to the fluid is described by the Stokes formula modified by the slip correction factor C_{c}:

$$F_{\mathrm{D}} = \frac{3\pi\mu v d}{C_{\mathrm{c}}}, \qquad (1.1)$$

where μ is the dynamic viscosity of air, v velocity of particle, and d particle diameter.

When a particle is released in air, it quickly reaches its terminal settling velocity, a condition where the drag force of the air on the particle will be exactly equal and opposite to the force of gravity F_{G}. At this condition,

$$F_{\mathrm{D}} = F_{\mathrm{G}} = mg = \frac{\rho_{\mathrm{p}} \pi d^3 g}{6}, \qquad (1.2)$$

where m is a particle mass, g the acceleration of gravity, and ρ_{p} the density of the particle. Solving Equation 1.2 for terminal settling velocity v_{TS} gives

$$v_{\mathrm{TS}} = \frac{\rho_{\mathrm{p}} d^2 g C_{\mathrm{c}}}{18\mu}. \qquad (1.3)$$

This equation can be expressed with a mechanical mobility of particle B and the *relaxation time* τ.

$$v_{\mathrm{TS}} = Bmg = \tau\, g\,. \qquad (1.4)$$

The terminal velocity for other kinds of external forces, such as centrifugal force, can be obtained by derivations similar to that given above. The centrifugal force F_{C} and the terminal velocity v_{TC} in the centrifugal force field are

$$F_{\mathrm{C}} = mr\omega^2 = \frac{m{v_{\mathrm{T}}}^2}{r}, \qquad (1.5)$$

$$v_{\mathrm{TC}} = \frac{\rho_{\mathrm{p}} d^2 r\omega^2 C_{\mathrm{c}}}{18\mu}, \qquad (1.6)$$

where r is radius position of particle, ω the rotational speed, and v_{T} the tangential velocity.

Terminal settling velocity increases rapidly with particle size, being proportional to the square of particle diameter. The equations for drag force, and settling velocity are based on spherical particles. Liquid droplets and some condensed vapors are spherical, while most of other types of particles are non-spherical. A correction factor called the *dynamic shape factor* is applied to Stokes's law to calculate the effect of shape on particle motion. Dynamic shape factor is defined as the ratio of the actual resistance force of the non-spherical particle to the resistance force of a sphere with the same volume and velocity. The dynamic shape factor χ is given by

$$\chi = \frac{F_{\mathrm{D}} C_{\mathrm{c}}}{3\pi\mu v d_{\mathrm{e}}}, \qquad (1.7)$$

where d_{e} is the volume equivalent diameter, the diameter of the sphere having the same volume as the irregular particle. And the terminal settling velocity is

$$v_{\mathrm{TS}} = \frac{\rho_{\mathrm{p}} d_{\mathrm{e}}^{2} g C_{\mathrm{c}}}{18\mu\chi}. \qquad (1.8)$$

Stokes diameter and aerodynamic diameter are two equivalent diameters that have wide applications in aerosol technology. For any particle they are defined as follows:

- The Stokes diameter d_{s} is the diameter of the sphere that has the same density and settling velocity as the particle.
- The aerodynamic diameter d_{a} is the diameter of the unit density ($\rho_{\mathrm{p}} = 1$ g/cm^3) sphere that has the same settling velocity as the particle.

Equation 1.8 can be written in terms of these diameters:

$$v_{\mathrm{TS}} = \frac{\rho_{\mathrm{p}} d_{\mathrm{e}}^{2} g C_{\mathrm{c}}}{18\mu\chi} = \frac{\rho_{\mathrm{b}} d_{\mathrm{s}}^{2} g C_{\mathrm{c}}}{18\mu} = \frac{\rho_{0} d_{\mathrm{a}}^{2} g C_{\mathrm{c}}}{18\mu}, \qquad (1.9)$$

where ρ_{b} is density of bulk materials and ρ_0 unit density, 1 g/cm^3. From Equation 1.9 it is apparent that Stokes diameter standardizes particles of various shapes to spheres having the same aerodynamic property, settling velocity. Aerodynamic diameter standardizes not only for shape but also for density. An irregular particle and its equivalent spheres are compared in Figure 1.1.

Most of aerosol particles have some electric charge. When a charged particle is placed in an electric field, the electrostatic force F_{E} on a particle and the terminal electrostatic velocity v_{TE} are

$$F_{\mathrm{E}} = neE, \tag{1.10}$$

$$v_{\mathrm{TE}} = \frac{neEC_{\mathrm{c}}}{3\pi\mu d_{\mathrm{me}}}, \tag{1.11}$$

where n is number of charge, e elementary charge, E the electric field strength, and d_{me} the mobility equivalent diameter.

Several aerosol measurements that applying these properties are described in detail in the next section.

1.1.2. Aerosol measurement

Particle size distribution of aerosols can be measured using various instrumental techniques, such as inertial classification (including cyclones, centrifuges, and inertial impactors), light-scattering particle counter (single-particle optical counters), electrical aerosol analyzer (electrical mobility analyzer), and set of diffusion battery–condensation particle counter. Many of these techniques classified aerosol based on the balance between the drag force and external force acting on the particles. The external forces are include: the centrifugal force used in cyclone [1] and various types of aerosol centrifuges [2]; inertia of various types impactors [3-5]; gravity created in the horizontal elutriator [6] and the sedimentation cell [7,8]; the electrostatic force in the electrical aerosol analyzer [9,10] and the differential mobility analyzer (DMA) [11]; the diffusion force occurred in the diffusion batteries [12]; and inertia and the diffusion force for inertial filter [13].

Ehara et al. have developed the instrument called aerosol particle mass analyzer (APM) that uses a new method for classifying the aerosol particles by using a

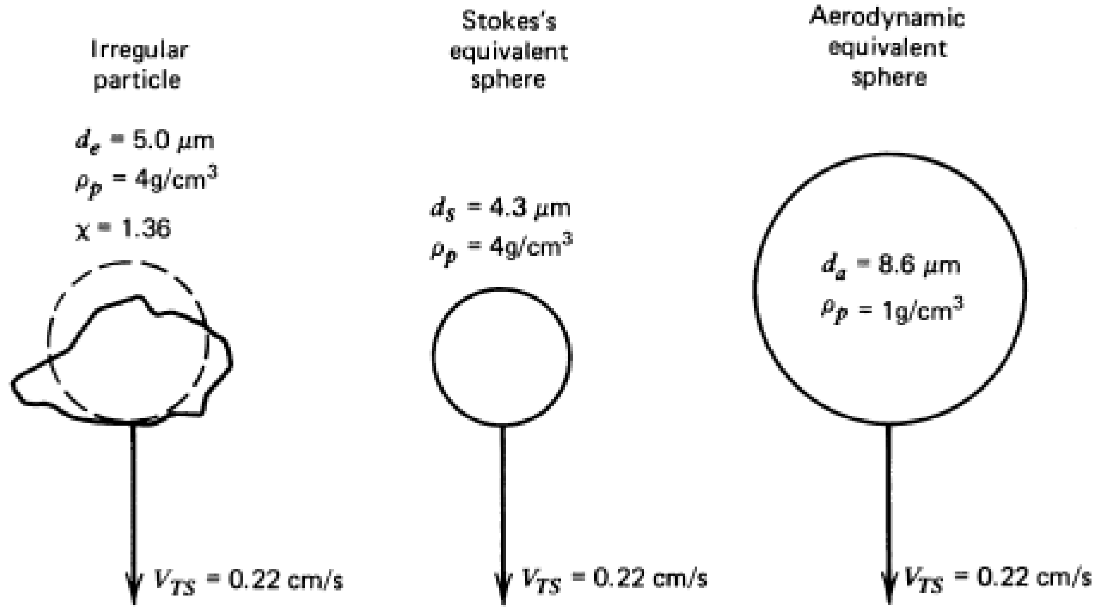

Figure. 1.1 Irregular shape of particle and its equivalent spheres.

balance of centrifugal force and electrostatic force [14]. The principle of APM is basically the similler as aerosol centrifuge, which will be described in detail in the next section.

1.2. Operation principle of aerosol centrifuge

1.2.1. Various type of aerosol centrifuges

Aerosol centrifuges are mechanical devices which spin rapidly while aerosol particles are flow through it at a controlled rate. This method may separate the small size of particle from the big one due to the application of a high centrifugal force to the passed particles. In aerosol centrifuges, clean air enters from the laminator and passes through the centrifuge duct while the centrifuge is spinning at a high rotation speed. Pre-classified particles enter the centrifuge through a narrow slit located near the inner wall of the centrifuge and are carried through the centrifuge duct. The particles are penetrate through the winnowing air as the result of the centrifugal forces until it reaches the outer wall of the centrifuge and finally deposits. At a given operating condition, the site of deposition on the outer wall depends mainly on particle size. Large particles tend to be deposited first, it is therefore placed on the top side, while the smaller particles will be deposited on the lower side. Various type of aerosol centrifuges, featuring specific aspects of the operation characteristic has been built, and it is mainly categorized into four types. The first is called "*conifuge*". It is the first generation of centrifugal aerosol spectrometer, which was built in 1950 by Sawyer and Walton [15]. Cylindrical duct aerosol spectrometer was created next. Semi-dispersive aerosol centrifuge was then introduced by the Goetz Aerosol Spectrometer as the third generation. And the last one which was inspired by the third generation centrifuge named spiral duct aerosol spectrometer is having a long rectangular duct. Operation principles of all of these instruments are similar. Thus, performance characteristics and operational limitation can be illustrated by considering a simple instrument; cylindrical duct aerosol spectrometer [2]. Details of the other types will be described in the next section.

1.2.2. Principle of aerosol centrifuge; cylindrical duct aerosol spectrometer

Figure 1.2 shows the top view of a cylindrical duct aerosol spectrometer. Several instruments have been created by adopting the principle of this device [16, 17]. Most of these instruments have a depth in the axial direction (h) which is longer than that the width in the radial direction (r_2 - r_1). The sample containing air and particles is fed from the sample inlet at the inner wall and will be passed to the deposition duct. The clean air is introduced into the duct through a laminating device. Both of the samples and clean air are drawn down the duct by applying a vacuum placed behind the filter at the bottom of the duct. Fluid flow inside the duct is laminar, therefore particles tend to remain as a thin layer on the surface of inner wall. The equation of motion for radial direction for a particle having mass *m* in the duct is given by Equation 1.5. And maximum penetration distance (l_d) for particles which entering the duct at r_1 is expressed by

$$l_d = \frac{36\mu}{\pi^2}\left(\frac{\pi^2 QI}{\rho d^2 C_c \omega^2}\right) = \frac{9\mu}{\pi^2}\left(\frac{QI}{\rho d^2 C_c v^2}\right), \tag{1.12}$$

where *Q* represents volumetric flow rate, *v* rotational speed in revolutions per unit time (= $\omega/2\pi$) and *I* the instrument geometrical constant given by

$$I = \frac{K}{h}\left\{\frac{r_2 + r_1}{(r_2 - r_1)^2} + \frac{2r_1 r_2}{(r_2 - r_1)^3}\ln\left(\frac{r_1}{r_2}\right)\right\}. \tag{1.13}$$

where *K* represents ratio of center line velocity to average velocity.

Figure 1.3 shows the penetration distance against $QI/\rho d^2 C_c v^2$ and experimental data from three different cylindrical instruments. Equation 1.12 illustrates some of the operational limitations. The total flow rate *Q* must be limited to prevent particles of interest from penetrating the deposition duct. Small particle collection requires long ducts because penetration distance is inversely proportional to particle diameter squared. The equation indicates that high flow rates and small particle sizes can be compensated for if sufficient rotational speed is used. However, some mechanical difficulties related

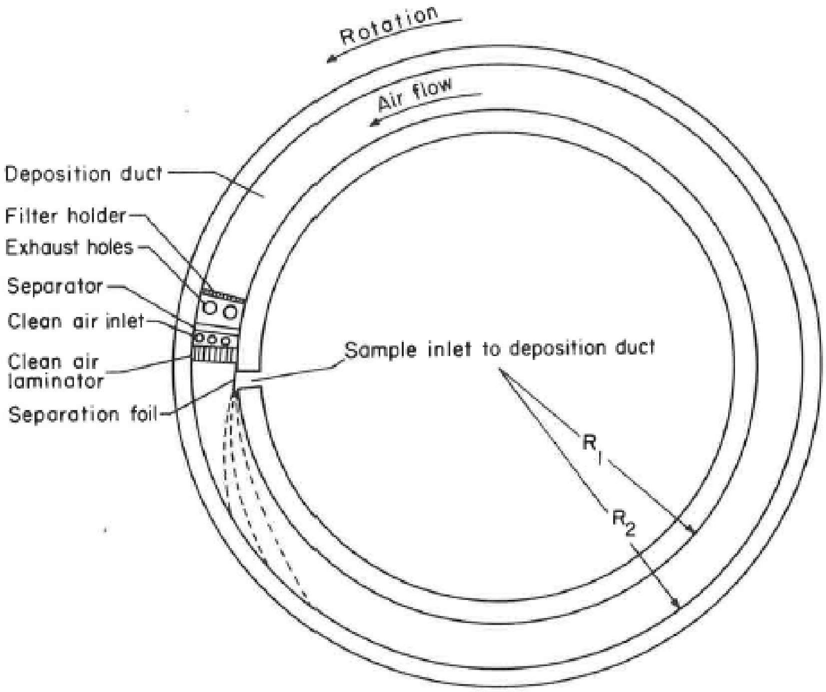

Figure. 1.2 Top view of a cylindrical duct aerosol spectrometer.

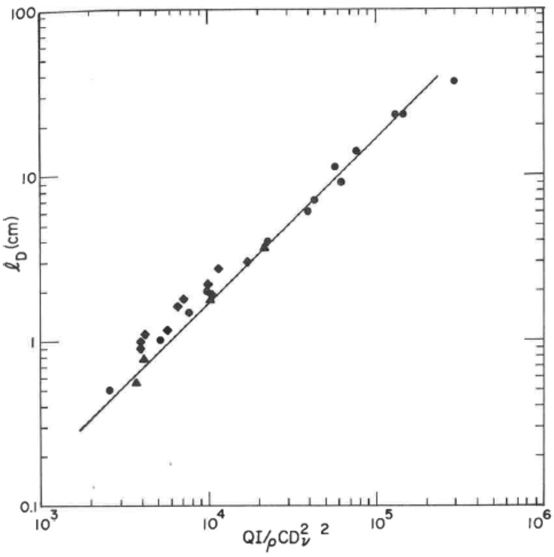

Figure. 1.3 Penetration distance as a function of $QI/\rho d^2 C_c v^2$.

to the high rotational speed such as the increase of secondary flows are occurring as a result of Coriolis forces and inertia in the rotating curved duct [18].

Penetration distance in aerosol spectrometers with more complicated geometry of duct, cannot be determined analytically. However, the parameters that affect the performance of these instruments can be determined from the equations for the cylindrical instrument. The form of I in Equation 1.12 will vary with deposition duct geometry. The penetration distance for all spectrometers of this type will be directly proportional to the flow rate through the duct and inversely proportional to the square of the rotational speed and particle diameter. The resolution of spectrometers is dependent on the ratio of the sampling rate S to the total flow rate Q (S/Q). It also depends on the width of the deposition duct (Figure 1.4). However, this effect becomes insignificant for instruments having r_2 greater than 50 mm.

1.2.3. First aerosol centrifuge: Conifuge

A schematic diagram of conifuge is shown in Figure 1.5. It consists of a narrow annulus between two right cones. The cones, in a sealed chamber, are rotated by an electric motor. The rotating cones work as a centrifugal pump pulling air from the top and release it through jets located around the cone base. Clean air recirculates through the sealed chamber and the top of the cones. When air is releasing from the sealed chamber, an equal amount of air sample is entering the aerosol inlet, spreading out in a thin layer over the inner cone before going down to the annulus covered by a much thicker layer of clean air. In the annulus, the particles are subjected to a centrifugal force which will accelerate the particles toward the outer wall, as they will pass down the channel. All particles have essentially the same distance to flow to the outer wall and deposit in a continuously graded spectrum according to radial velocity. Cascade velocity of the channel decreases with distance because of the increase of cross-sectional area. It will create larger radius and finally increase centrifugal force.

This phenomenon compresses the spectrum with respect to penetration distance. The instrument operation is limited by the condition of laminar flow in the annulus and

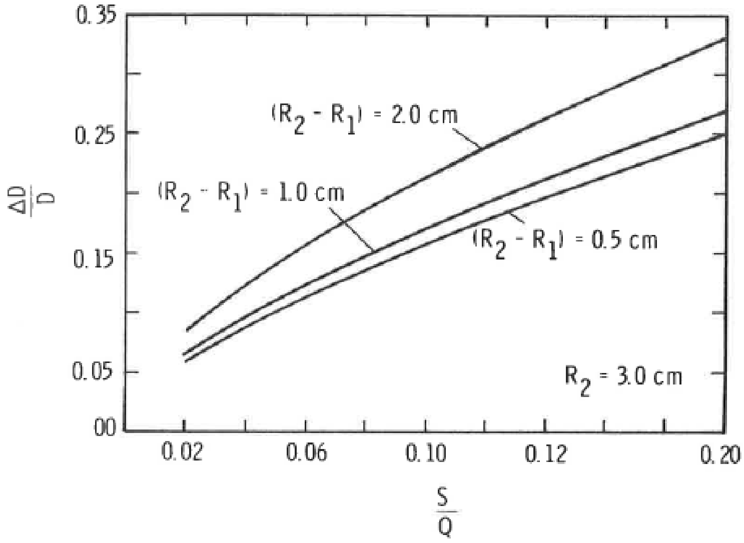

Figure 1.4 Resolution for cylindrical duct aerosol spectrometer.

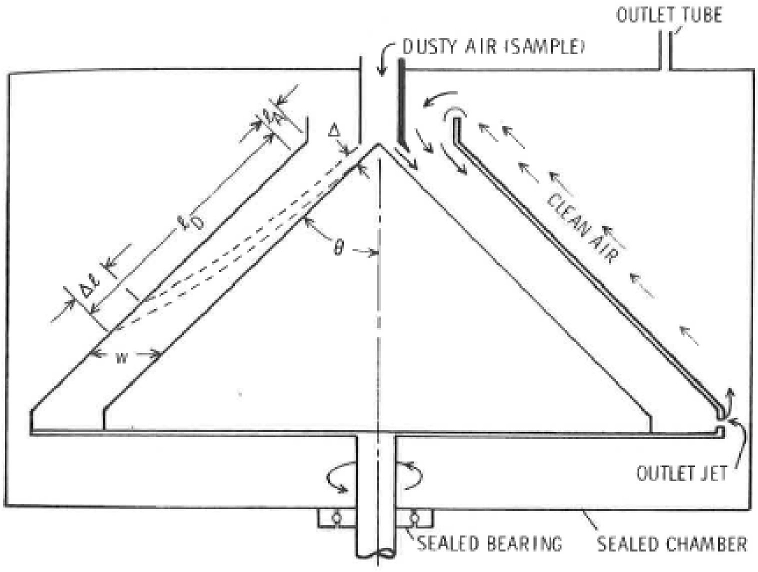

Figure 1.5 Schematic view of the conifuge.

the necessity of air sample to create a thin layer, which will limit the sampling rates. A thin layer of air sample is required to provide reasonable resolution or separation. This is illustrated by the particle trajectories shown in Figure 1.5. Same size of particles will deposit over the length of Δl depending on where they enter the annulus. Thinner layer of air sample, better resolution and lower sampling rate will be obtained.

Conifuge samples are normally collected on foils lining on the outer cone or on slides located from slots cut into the outer cone. The foil or slide can be cut into strips and analyzed to determine the mass or particle number with respect to the diameter difference across the strip given by the calibration curve of the instrument. The use of slides or foils requires area corrections. Determination of size distribution requires corrections for inlet losses and small particles that penetrate the annulus.

1.2.4. Semi-dispersive aerosol centrifuge

Several types of semi-dispersive aerosol centrifuges have been made, and Goetz Aerosol Spectrometer [19] is the most popular overall. The instrument shown in Figure 1.6 consists of two helical ducts of 2.5 turns on the outside of a 30° right cone. The radius of the cone is about 38 mm. The cone at the outer wall of the ducts is removable and could be covered by a foil or paper for collection and subsequent analysis of the deposit. The cones rotation speed can be varied up to 24000 rpm. The impeller of rotating ducts pulls the sample down the inlet and flows through the ducts. Flow rate through each duct is independently controlled by jets located at the end of the duct. The flow rate through the channels depends on the rotational speed ω and on the size O of the interchangeable orifice at the end of each channel. The farther the particles travel down the duct, the greater centrifugal force and deposition velocity are. Gerber [20] evaluated the relation between particle concentration and penetration distance using standard particles, and found a consistent pattern in all of the previous calibration work. Figure 1.7 shows the concentration curves of latex-particle as a function of deposit length. It was discovered that for any given operating condition of the centrifuge, i.e.,

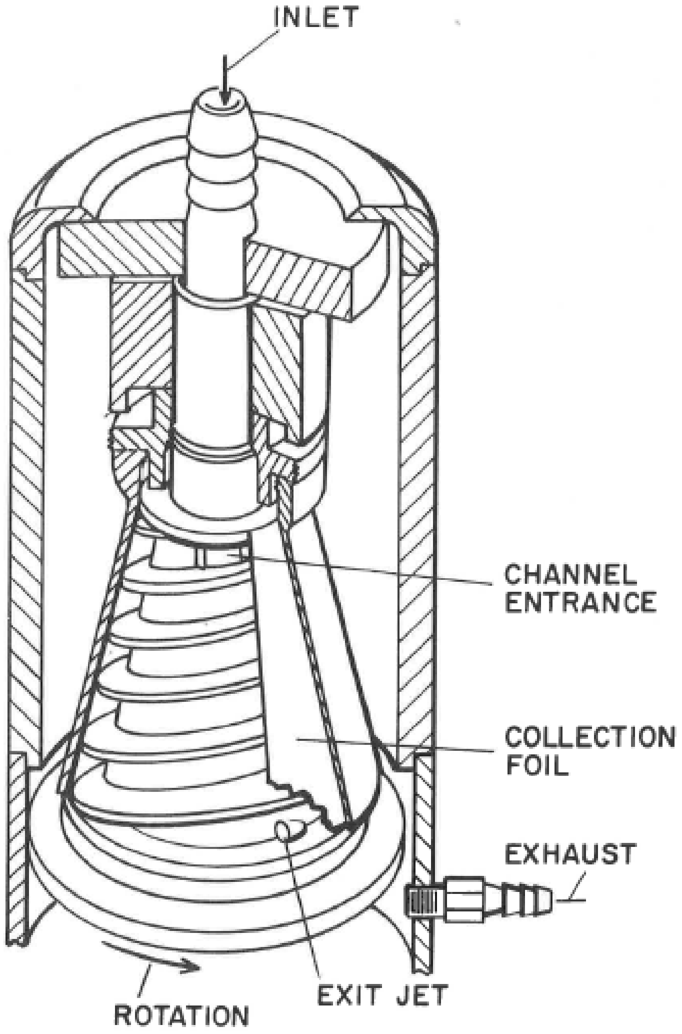

Figure 1.6 Semi-dispersive aerosol centrifuge: Goetz Aerosol “Spectrometer”

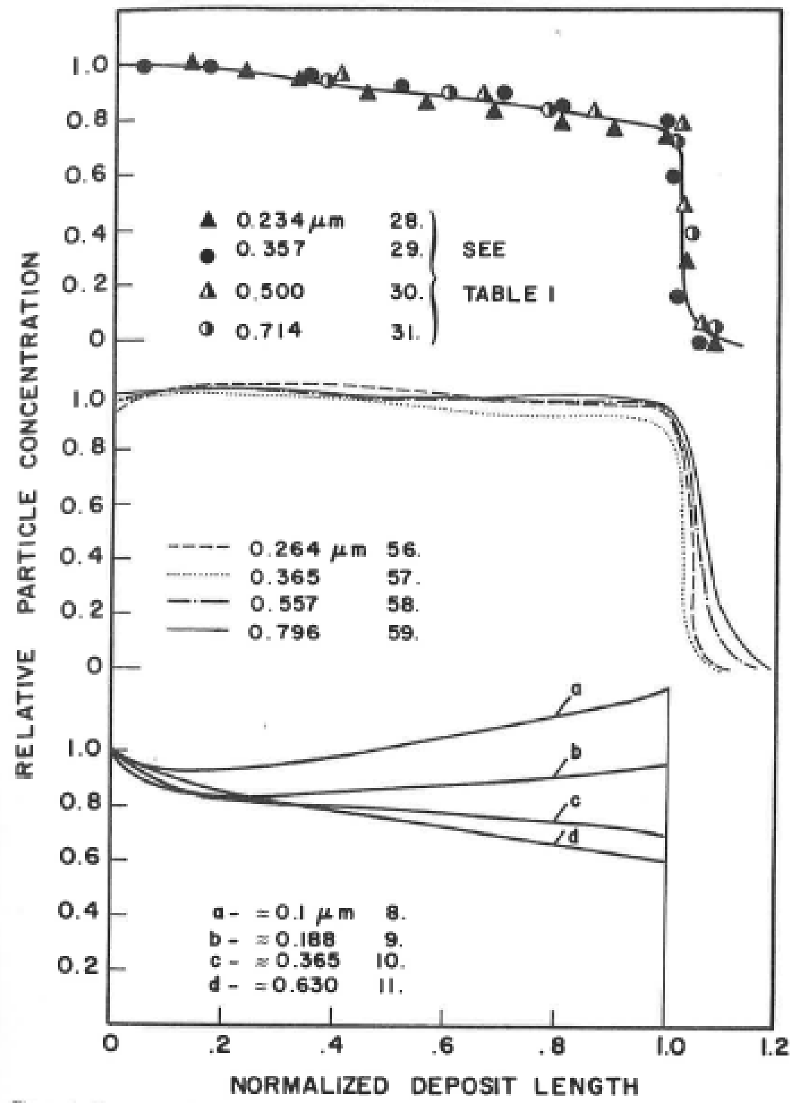

Figure 1.7 Experimental latex particle deposited concentration curves (Gerber [20], upper curve; Horvath [21], middle curve) and theoretical predictions by Stöber and Zessäck [22], lower curve. All curves were normalized over the distance l_b - l_a and they reflect the same operating conditions of the centrifuge. The instrument used by Horvath [21] differed slightly from the Goetz centrifuge in baffle geometry and channel dimensions.

any given values of ω and O, the shape of the deposited concentration curves for various values of particle diameter d was nearly invariant when the length l_b - l_a was normalized. It is clearly shown by the figure that the theory is nearly correct with cutoffs at maximum penetration distance. However, it was not as sharp as indicated by theory. Turbulent flow was occurred for a short distance below the inlet to the ducts.

Semi-dispersive centrifuges offer higher sampling rate (up to 125 L/min for Kast instrument [23]) compared to the others. However, uneven deposit concentration, poor definition of maximum penetration distance, and particle losses in the turbulent flow region, make determination of particle size distributions very difficult and susceptible to errors.

1.2.5. Spiral duct aerosol spectrometer

The low sampling rate of the conifuge and the instabilities at high rotational speeds and flow rates indicated the need of a better design. In 1969 Stöber and Flachsbart designed a centrifugal spectrometer with a spiral duct similar to a semidispersive centrifuge [18]. A blow-up view of a similar instrument is shown in Figure 1.8 [24]. The instrument has a 1800 mm length equipped with rectangular duct (33 mm deep and 10 mm wide, except for the initial part of the duct where the width is 17 mm) cut into a flat cylinder. Air flow through the instrument is controlled externally. When it is flow through ducts, it will be separated by rotating seals in the drive shaft of the instrument and in the base of the instrument. Filtered air is introduced into the deposition duct through a laminator which is consist of several parallel foils. Suction is applied at the end of the duct, and the flow rate is greater than the laminating air flow with the difference being drawn down the aerosol inlet on the axis of rotation. The center inlet directs the air sample down the deposition duct as a thin layer next to the inner wall. Particles passing down the spinning duct are subjected to an increasing centrifugal force accelerating the particles toward the outer wall where they are deposited on a collection foil. The particles are separated and deposited on the outer wall in a continuously graded spectrum according to deposition rate or aerodynamic

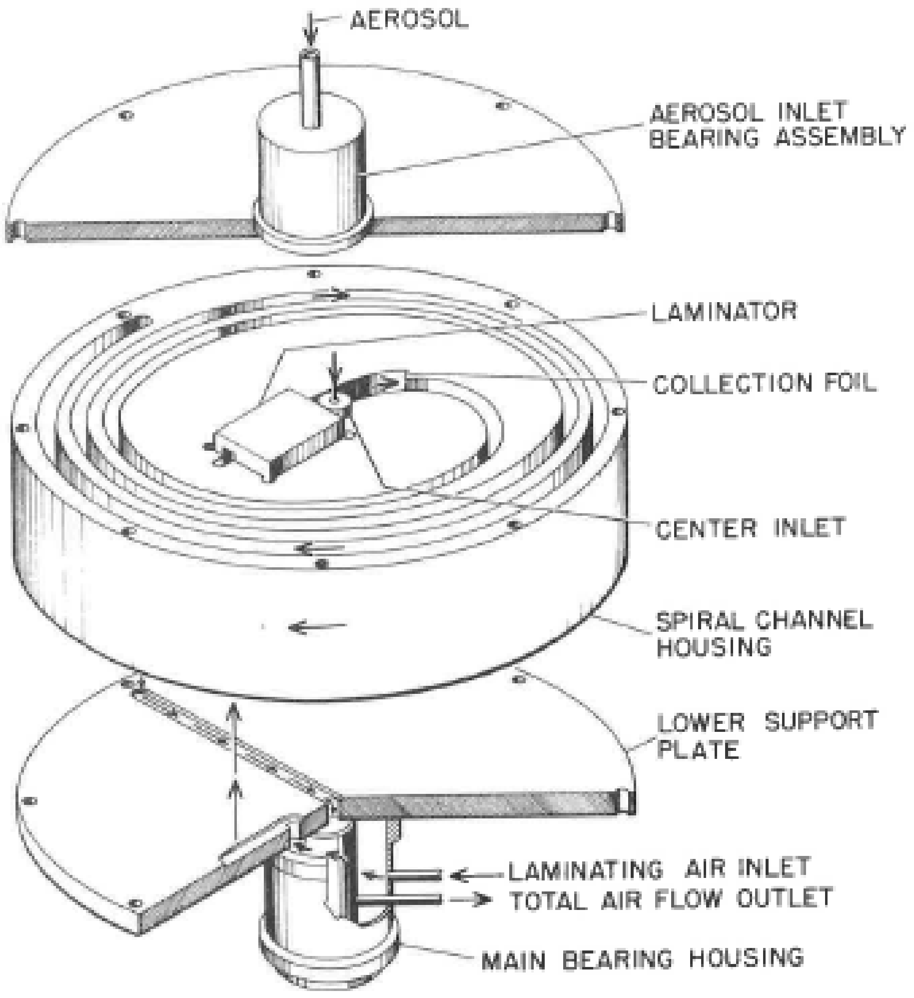

Figure 1.8 Schematic representation of the spiral duct spectrometer.

diameter.

The complicated geometry of the deposition duct limits analytical determination of particle trajectories or penetration distances. However, the functional relations between adjusted parameters and performances are similar to that of cylindrical duct instrument. Penetration distance is inversely proportional to the particle diameter squared and rotational speed squared, and is directly proportional to total flow rate. Resolution is dependent on the ratio of the thickness of the air sample layer to the thickness of the clean air layer, or the ratio of the two flow rates (S/Q). Total flow through the instrument and rotational speed are limited by the development of secondary flows that disrupt deposition patterns.

The physical size of long duct instrument and large deposition area make these instruments somewhat impractical for portable use. Several small, single turn, spiral duct spectrometers have been built for particle separation and to provide reasonably portable sampling instruments.

In all rotation, spiral duct samplers a portion of the inlet rotates so that the inlet loss corrections are necessary to determine size distributions. Losses can be calculated for well-defined rotating geometries [25]. In most cases the inlet geometry is not simple and is complicated by interfaces between fixed and rotating components so collection efficiencies must be determined experimentally. Asgharian and Godo reported that the deposition patterns on the outer wall and the deposition length as a function of particle diameter were calculated [26]. They solved the flow field in the centrifuge of Stöber and Flachsbart using a commercially available finite element software package and the flow field information was used to calculate the transport and deposition of particles and fibers in the centrifuge [18].

Table 1.1 shows the flow rate, rotational speed, and size range of collected particle of four types of aerosol centrifuges that were described above. The principal advantage of aerosol centrifuges is the collection of the sample as a continuously graded spectrum in terms of aerodynamic or inertial properties. This separation simplifies the determination of particle size distributions with respect to aerodynamic diameter for

Table 1.1 Comparison between the four types of aerosol centrifuges

Type of aerosol centrifuges	Sample Flow : S(L/min)	Total Flow: Q (L/min)	Ratio S / Q (cm)	Rotational speed (rpm)	Particle Size Range (µm)
conifuge	0.012 – 1.2	0.576 - 10	0.01 – 0.2	1500 - 10000	0.09 – 21.0
cylindrical aerosol spectrometer	0.5	5.0 - 15.4	0.02 – 0.2	1000 - 3000	0.1 – 8.0
semidispersive aerosol centrifuge	< 5 (usually) max. 125	-	-	6000 - 24000	0.11 – 1.4
spiral duct aerosol spectrometer	0.4 – 1.6	5 – 19	0.03 – 0.08	3000 - 4500	0.09 – 5.0

most parameters of interest. The resolution, or separation of particles according to aerodynamic characteristics achieved by these instruments is not attainable by any other meaning. While the disadvantages are relatively low sampling rates, collection of the sample over a large surface, and delay between the time of sampling and determination of results.

The principles and features of the centrifuge are described above. In comparison with an APM, although the sample flow rate is low, an APM can classify airborne particles in suspension without any particle collection and it is possible to measure the concentration by connecting a detector downstream of the APM. In other words, APM system is an in situ aerosol mass measurement. It also has an advantage that the center of the classification band in mass-to-charge ratio is not influenced by particle shape and is solely determined by an intrinsic particle property. The operating principles and applications of the APM are introduced in the next section.

1.3. Aerosol particle mass spectrometer (APM)

1.3.1. DMA + CPC

Principally, APM and DMA have similar characteristics. As mentioned in Section 1.1.2, DMA utilizes the drag force to balance the electrostatic force, while APM utilizes the centrifugal force. As a result, while DMA classifies particles with electrical mobility equivalent diameter, APM classifies particles with mass. Because of this feature, APM is often used in combination with DMA, since it is possible to measure the size and mass of particles at the same time, thereby determining their effective density. Since both APM and DMA are aerosol classifiers, they need a detector for measuring the classified particle concentration and a charging device as well for utilizing the electrostatic force. In the beginning section, measurement system using the DMA has been introduced. After particles to be measured are charged by introducing an aerosol charge neutralizer, they are classified by the DMA according to their size, and the concentration of each classified particle size is measured by a detector. Two types of detectors are usually used to detect mobility classified particles: a condensation particle counter (CPC) or an aerosol electrometer. The first detector is the most commonly used, due to its high counting efficiency. While, the other is used for high concentration particles, or when particles are too small to be detected by the CPC. Combining CPC with APM, creating a series of measurement system that are Aerosol charge neutralizer + DMA + APM + CPC, called DMA-APM system.

1.3.2. Classification principle of APM

The APM comprises of two coaxial cylindrical electrodes rotating at the same angular velocity. Charged particles are fed into the annular gap between the rotating electrodes, while a voltage is applied between the electrodes. The centrifugal and electrostatic forces are in balance for particles of a particular mass, allowing them to pass through the gap, while other particles are lost by colliding the surface of the electrodes. Thus the APM classifies particles according to their mass-to-charge ratio. If the number of charges on the particles is already known, the mass is also known. A typical construction of the APM and its operating principle were shown in Figure 1.9a. In this figure, the gap between the two cylindrical electrodes is the classification space. Let *r* and *z* denote the radial and axial coordinates in a cylindrical coordinate system, and let *v*(*r*) denote the air flow velocity in the classification space along *z* axis. The equations of motion for a particle having mass *m* and charge *q* in the classification space are given by

$$\frac{m}{\tau}\cdot\frac{dr}{dt} = m\cdot r\cdot\omega^2 - \frac{q\cdot V}{r\cdot\ln(r_2/r_1)}\ , \tag{1.14}$$

$$\frac{m}{\tau}\left\{\frac{dz}{dt} - v(r)\right\} = 0\,. \tag{1.15}$$

Equations 1.14 and 1.15 are for radial and axial directions, respectively. The left-hand-side term of both equations represent the drag force acting on the particle. The first and second terms on the right-hand side of Equation 1.14 represent the centrifugal and electrostatic forces, respectively. In these equations, τ is the particle relaxation time, ω the rotational speed, V the voltage between the electrodes, r_1 and r_2 the inner and outer radius of the classification space. The trajectory of a particle in the classification

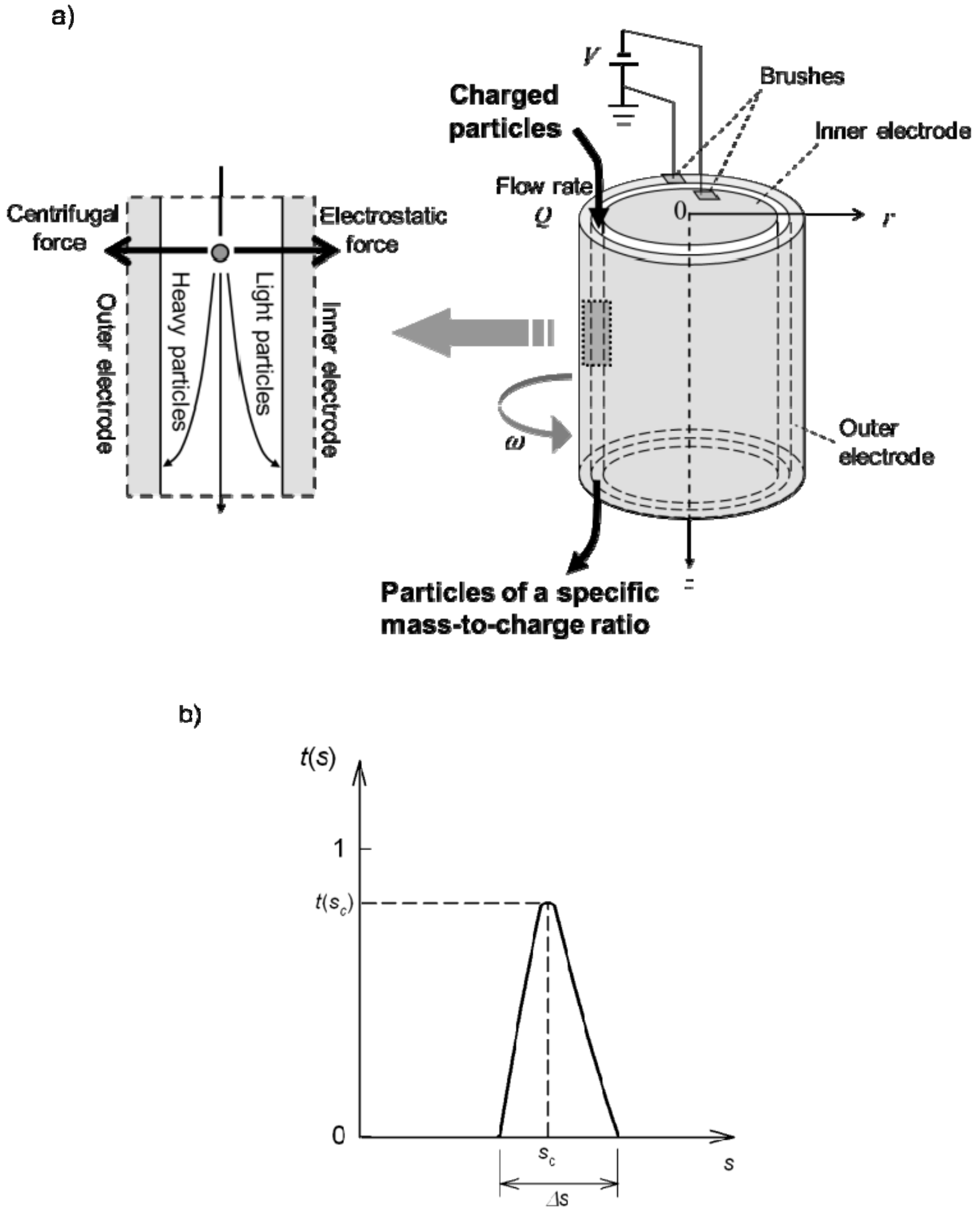

Figure 1.9 The aerosol particle mass analyzer (APM). (a) A typical construction of the APM and its operating principle, (b) a typical appearance of the APM transfer function.

space can be determined by solving the above two equations simultaneously.

For a particle of a certain mass-to-charge ratio m/q (hereafter represented by "s") in an APM that is operated at a constant rotation speed and voltage, the centrifugal and electrostatic force balance at some radius of r, which can be calculated from Equation 1.14 by setting the terminal velocity equal to zero. Let s_c denote the value of s for which the balance occurs at the center of the classification space r_c ($r_c = (r_1 + r_2) / 2$), i.e.,

$$s_c = \frac{V}{r_c^2 \cdot \omega^2 \cdot \ln(r_2 / r_1)}. \qquad (1.16)$$

Ehara et al. calculated the particle trajectory and derived transfer functions by assuming that the radial flow profile in the APM classification space is either uniform or parabolic [14]. The transfer function, $t(s)$, is defined as the probability for particles of the mass-to-charge ratio of s to pass through the classification space of an APM of a certain geometry and under a certain operating condition without being deposited on the electrode surfaces.

Figure 1.9b shows a typical appearance of the APM transfer function that is theoretically derived by assuming a parabolic flow profile in the classification space. The transfer function has the following characteristics:

- The transfer function has the maximum at the mass-to-charge ratio of s_c.
- The appearance of the transfer function is roughly symmetrical with respect to s_c.
- For an APM of a certain configuration, the appearance of the transfer function depends on non-dimensional constant λ (hereafter called "the classification performance parameter"). This parameter λ is expressed by the following equation:

  $$\lambda = \frac{2\tau \cdot \omega^2 \cdot L}{\bar{v}} \qquad (1.17)$$

  where L is the axial length of the APM classification space and $\bar{v}$ is the mean axial flow velocity in the classification space.

- The transfer function reduces both the width and height as λ increases. This means that the resolution improves while the penetration diminishes.

1.3.3. Applications using APM

The APM has been widely used in many aerosol research fields, for evaluation of various particle properties such as "effective" density [27, 28], morphology through estimation of the mass-mobility exponent [29, 30], the mixing ratio of internally-mixed particles [31, 32], material density [33], particulate mass concentration [34, 35], mass [36], volume [37], and porosity [38, 39]. The APM can also be used as a generator of particles having a specified mass [40, 41].

1.4. Objective and outline of thesis

Figure 1.10 shows the outline of this thesis. The objective of this thesis is to develop the APM as well as evaluate its performance. Two types of APM were developed and their classification performances were carefully evaluated. Chapter 1 reported the background of aerosol measurement, types of aerosol centrifuge and their principle, and outline of APM.

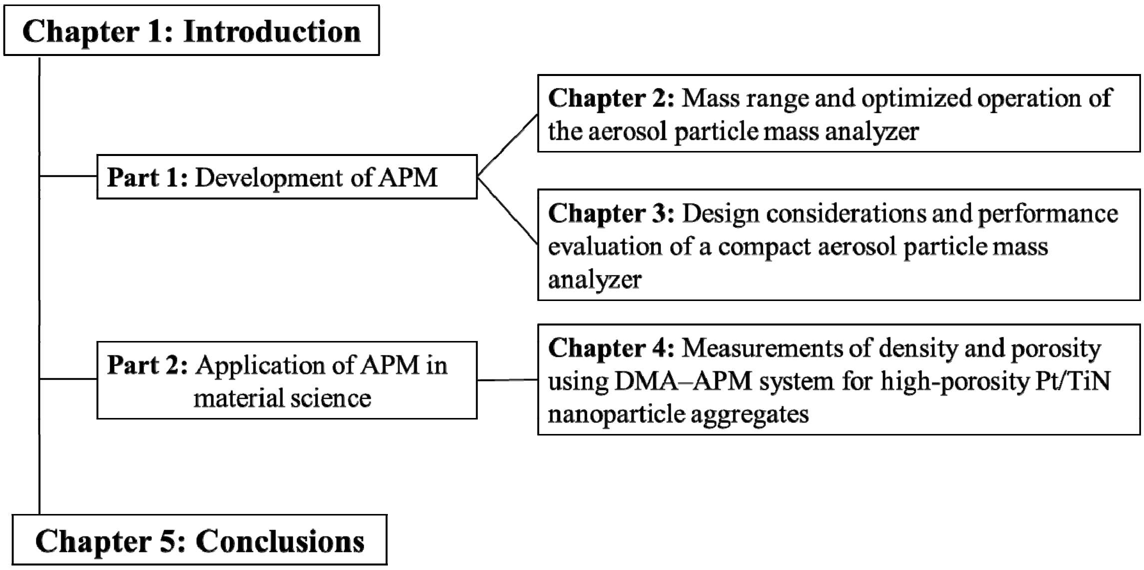

Figure. 1.10 Organization of chapters of the present thesis.

Chapter 2 describes the appropriate mass range and operating conditions for the first commercial instrument, Model 3600 APM (Kanomax Japan Inc.) to maximize the mass classification performance. I tried to list factors that set limits for the APM, which were constraints of the rotation speed and the voltage, as well as requirements on the APM classification performance parameter, λ, that guarantee at least minimal performance in both resolution and penetration were also explained here. The operation diagram of APM, which is a tool to visualize the limits and mass range was introduced. In this chapter, I proposed to operate the APM at the λ value within the range of 0.25–0.5 for optimum classification performance by balancing both resolution and penetration. The mass range for the APM, with the λ value maintained between 0.25 and 0.5, was calculated to be from 0.003 to 2000 fg. To verify the validity of the mass range and the idea of the optimized operation, experiments on an APM with monodisperse particles were conducted. It was found that the APM was able to perform mass classification with an accuracy better than 5 % down to 50 nm. Underestimation of mass and reduction of resolution and penetration were observed at particle with size smaller than 30 nm [42].

The size of Model 3600 APM is large. Therefore, it is not suitable for field measurements. I have developed an APM which is compact and more suitable for field measurements application compared to that of Model 3600 APM. Design and performance evaluation of the compact APM are reported in Chapter 3. Necessary parameters for the required performance in classifying particle mass were set first. Then, theoretical framework for the design parameters of an APM that satisfy the parameters was formulated. Finally, the design parameters that satisfy the condition were determined while reducing the instrument size. The necessary parameters include the classification range from 0.001 fg to 1000 fg, and the condition that both the classification resolution and particle penetration in this mass range are high enough. A prototype having the design parameters determined according to this theoretical framework was constructed, and its performance was evaluated experimentally. It was confirmed that the performance of the compact APM operated at the aerosol flow rate of

0.3 L/min was comparable to that of the Model 3600 APM operated at 1 L/min. Because of the reduced size and of the resultant improved portability, it is expected that the compact APM is readily applicable for field measurements [43].

Chapter 4 introduces an example of measurement of the effective density and porosity of nanoparticle agglomerates as the application of APM. This study evaluated the influence of formic acid on the electrochemical properties of high porosity titanium nitride supported platinum (Pt/TiN) nanoparticle aggregates synthesised via self-assembly assisted spray pyrolysis. The effective density of TiN nanoparticle aggregates prepared via this method was measured using a DMA-APM system (see Section 1.3.1). The porosity of nanoparticle agglomerates was calculated from the effective density [44].

Chapter 5 summarizes the development of two types of APM and their performance.

1.5. References

[1] Beeckmans, J. M. In *Aerosol Measurement* (Edited by Lundgren, D. A. et al.), (1979) p. 56. Univ. Press Florida, Gainesville.

[2] Tillery, M. I. In *Aerosol Measurement* (Edited by Lundgren, D. A. et al.), (1979) p. 3. Univ. Press Florida, Gainesville.

[3] Marple, V. A. and Willeke, K. (1979) *ibid.*, p. 90.

[4] Masuda, H., Hochrainer, D. and Stöber, W. An improved virtual impactor for particle classification and generation of test aerosols with narrow size distributions. *J. Aerosol Sci.* (1979) 10, 275-287.

[5] Marjamäki, M., Keskinen, J., Chen, D-R. and Pui, D. Y. H. Performance evaluation of the electrical low-pressure impactor (ELPI), *J. Aerosol Sci.* (2000) 31, 249-261.

[6] Stöber, W. and Flachsbart, H. High resolution aerodynamic size spectrometry of quasi-monodisperse latex spheres with a spiral centrifuge. *J. Aerosol Sci.* (1971) 2, 103-116.

[7] Allen, M. D. and Raabe, O. G. Slip correction measurements of spherical solid aerosol particles in an improved Millikan apparatus *Aerosol Sci. Technol.* (1985) 4, 269-286.

[8] Kousaka, Y., Okuyama, K., Shimada, M. and Ohshima, H. A precise method to determine the diameter of airborne latex particles. *J. Aerosol Sci.* (1988) 19, 501-509.

[9] Whitby, K. T. In *Fine Particles* (Edited by Liu, B. Y. H.), (1976) p. 584. Academic Press, New York.

[10] Liu, B. Y. H., Pui, D. Y. H. and Kapadia, A. In *Aerosol Measurement* (Edited by Lundgren, D. A. et al.), (1979) p. 341. Univ. Press Florida, Gainesville.

[11] Knutson, E. O. and Whitby, K. T. Aerosol classification by electric mobility: apparatus, theory, and applications. *J. Aerosol Sci.* (1975) 6, 443-451.

[12] Sinclair, D., Countess, R. J., Liu, B. Y. H. and Pui, D. Y. H. In *Aerosol Measurement* (Edited by Lundgren, D. A. et al.), (1979) p. 554. Univ. Press Florida, Gainesville.

[13] Otani, Y., Eryu, K., Furuuchi, M., Tajima, N. and Tekasakul, P. Inertial classification of nanoparticles with fibrous filters. *Aerosol Air Qual. Res.* (2007) 7, 343-352.

[14] Ehara, K., Hagwood, C. and Coakley, K. J. Novel method to classify aerosol particles according to their mass-to-charge ratio - Aerosol particle mass analyzer. *J. Aerosol Sci.* (1996) 27, 217-234.

[15] Sawyer, K. F. and Walton, W. H. The “Conifuge”: A size sampling device for airborne particles. *J. Sci. Instrum.* (1950) 27, 272.

[16] Hochrainer, D. A new centrifuge to measure the aerodynamic diameter of aerosol particles in the submicron range. *J. Colloid Interface Sci.* (1971) 36, 191–194.

[17] Tillery, M. I. A concentric aerosol spectrometer, *A. Ind. Hyg. Assoc. J.* (1974) 35, 62–74.

[18] Stöber, W. and Flachsbart, H. Size separating precipitation of aerosols in a spinning spiral duct. *Environ. Sci. Technol.* (1969) 3, 1280–1296.

[19] Goetz, A., Stevenson, H. J. R. and Preining, O. The design and performance of the aerosol spectrometer. *J. Air Pollition Control Assoc.* (1960) 10, 378.

[20] Gerber, H. E. On the performance of the Goetz aerosol spectrometer. *Atmos. Environ.* (1971) 5, 1009.

[21] Horvath, H. Discussions: On the performance of the Goetz aerosol spectrometer. *Atmos. Environ.,* (1973) 7, 1003-1011.

[22] Stöber, W. and Zessack, U. On the theory of a conical aerosol centrifuge. Staub-Reinhalt. Luft, (1964) 24, 295-305.

[23] Kast, W. Neues staubmessgerat zur schnellbestimmung der staubkonzentration und der komverteilung. *Staub-Reinhalt. Luft.* (1961) 21, 215.

[24] Moss, O. R., Ettinger, H. J. and Coulter, J. R. Aerosol density measurements using a modified spiral centrifuge aerosol spectrometer. *Environ. Sci. Technol.* (1972) 6, 614–617.

[25] Mercer, T. T. In *Aerosol Technology in Hazard Evaluation* (1973) New York, Academic Press.

[26] Asgharian, B. and Godo, M. N. Size separation of spherical particles and fibers in an aerosol centrifuge. *Aerosol Sci. Technol.* (1999) 30, 383-400.

[27] McMurry, P. H., Wang, X., Park, K. and Ehara, K. The relationship between mass and mobility for atmospheric particles: A new technique for measuring particle density. *Aerosol Sci. Technol.* (2002) 36, 227-238.

[28] Liu, Q., Ma, X. and Zachariah, M. R. Combined on-line differential mobility and particle mass analysis for determination of size resolved particle density and microstructure evolution. *Microporous Mesoporous Mater.* (2012) 153, 210–216

[29] Park, K., Cao, F., Kittelson, D. B. and McMurry, P. H. Relationship between particle mass and mobility for diesel exhaust particles. *Environ. Sci. Technol.* (2003a) 37, 577-583.

[30] Ku, B. K. and Evans, D. E. Investigation of aerosol surface area estimation from number and mass concentration measurements: Particle density effect. *Aerosol Sci. Technol.* (2012) 46, 473-484.

[31] Sakurai, H., Park, K., McMurry, P. H., Zarling, D. D., Kittelson, D. B. and Ziemann, P. J. Size-dependent mixing characteristics of volatile and nonvolatile components in diesel exhaust aerosols. *Environ. Sci. Technol.* (2003) 37, 5487-5495.

[32] Khalizov, A. F., Zhang, R. Y., Zhang, D., Xue, H. X., Pagels, J. and McMurry, P. H. Formation of highly hygroscopic soot aerosols upon internal mixing with sulfuric acid vapor. *J. Geophys. Res.-Atmos.* (2009) 114.

[33] Kuwata, M., Zorn, S. R. and Martin, S. T. Using elemental ratios to predict the density of organic material composed of carbon, hydrogen, and oxygen. *Environ. Sci. Technol.* (2012) 46, 787−794.

[34] Park, K., Kittelson, D. B. and McMurry, P. H. A closure study of aerosol mass concentration measurements: comparison of values obtained with filters and by direct measurements of mass distributions. *Atmos. Environ.* (2003b) 37, 1223-1230.

[35] Saito, K., Shinozaki, O., Yabe, A., Seto, T., Sakurai, H. and Ehara, K. Measuring mass emissions of diesel particulate matter by the DMA-APM method (Second report): Comparison with Filter Method. *Rev. Automotive Eng.* (2008) 29, 639-645.

[36] Kuwata, M., Kondo, Y. and Takegawa, N. Critical condensed mass for activation of black carbon as cloud condensation nuclei in Tokyo. *J. Geophys. Res.-Atmos.* (2009) 114.

[37] Lall, A. A., Rong, W., Madler, L. and Friedlander, S. K. Nanoparticle aggregate volume determination by electrical mobility analysis: Test of idealized aggregate theory using aerosol particle mass analyzer measurements. *J. Aerosol Sci.* (2008) 39, 403–417.

[38] Lee, S. Y., Widiyastuti, W., Tajima, N., Iskandar, F. and Okuyama, K. Measurement of the effective density of both spherical aggregated and ordered porous aerosol particles using mobility- and mass-analyzers. *Aerosol Sci. Technol.* 43 (2009) 136.

[39] Lee, S. Y., Chang, H., Ogi, T., Iskandar, F. and Okuyama, K. Measuring the effective density, porosity, and refractive index of carbonaceous particles by tandem aerosol techniques. *Carbon* (2011) 49, 2163–2172.

[40] Moteki, N., Takegawa, N., Koizumi, K., Nakamura, T. and Kondo, Y. Multiangle polarimetry of thermal emission and light scattering by individual particles in airflow. *Aerosol Sci. Technol.* (2011) 45, 1184–1198.

[41] Beranek, J., Imre, D. and Zelenyuk, A. Real- -time shape-based particle separation and detailed in situ particle shape characterization. *Anal. Chem.* (2012) 84, 1459-1465.

[42] Tajima, N., Fukushima, N., Ehara, K. and Sakurai, H. Mass range and optimized operation of the aerosol particle mass analyzer. *Aerosol Sci. Technol.* (2011) 45, 196-214.

[43] Tajima, N., Sakurai, H. Fukushima, N. and Ehara, K. Design considerations and performance evaluation of a compact aerosol particle mass analyzer. *Aerosol Sci. Technol,* in press.

[44] Ogi, T., Tajima, N., Balgis, R., Setyawan, H. and Okuyama, K. Influence of formic acid on electrochemical properties of high-porosity Pt/TiN nanoparticle aggregates. *AIChE Journal,* in press.

Chapter 2

Mass range and optimized operation of the aerosol particle mass analyzer

2.1 Introduction

The APM is an instrument that classifies aerosol particles according to their mass-to-charge ratio [1]. The APM can classify particles of diameters as small as 100 nm and less. It has an advantage that the center of the classification band in mass-to-charge ratio is not influenced by particle shape and is solely determined by an intrinsic particle property. Combined use of the APM and a DMA makes it possible to measure the size and mass of particles at the same time, thereby determining their effective density. The APM has been widely used in many aerosol research fields for various applications explained in Section 1.3.3.

For the DMA, which is an aerosol particle classifier similar to the APM in some aspects and is more widely used than the APM, there are several "rules of thumb" for its usage. For example, the particle size range that the DMA can be applied to is roughly from 1 nm to 1 μm, and the typical ratio of the sheath air flow rate to the aerosol flow rate is 10:1. Such practical rules, on the other hand, have not been established for the APM.

For particle mass classification by the APM, Ehara et al. [1] introduced a non-dimensional parameter λ, which characterizes the classification performance of the APM, and discussed the quantitative relationship of the resolution and penetration of the APM with the λ value. They also pointed out that there is a trade-off relationship between the resolution and the penetration while choosing the λ value, and that the conditions of both high resolution and high penetration are limited. Despite these theoretical foundations of the APM, not enough attention has been paid for operating the APM in actual measurements with its classification performance at the best. One of the reasons for this might be because I have not seen enough examples in which the theory was applied to real instruments and experimental conditions.

The objective of this study is to contribute in accumulating knowledge on how to optimize APM operations. First, by taking the first commercial model of APM as an example, I investigated theoretically the range that the APM can be used for particle classification, and then derived "standard" parameter settings recommended to maximize the performance of the APM. For the above investigation, a diagram that visualizes various constraints of the APM was developed, such as the upper and lower limits of the voltage and rotation speed. These constraints set boundary conditions and define an area in the diagram in which the APM can perform classification. The mass range that the APM can classify, which is the most fundamental parameter among several APM performance characteristics, was derived from this diagram.

The area in the diagram defined by the APM's constraints tells the maximum range of parameter settings of the APM. However, the classification performance characteristics are not uniform across the area, and, for example, the resolution is high but the penetration is too low in some part. By setting additional constraints on the λ value, I derived operation parameter settings that ensure both resolution and penetration are sufficiently high at the same time.

Following the above theoretical considerations, experiments were carried out to check whether or not the APM was able to perform classification at predicted resolution and penetration. This chapter reports results of these theoretical considerations and experiments.

2.2 Review of Particle Classification Principle of the APM

Detail explanation of the principle of APM has been described previously in Section 1.3.2. A typical appearance of the APM transfer function is shown in Figure 2.1. The center of the mass-to-charge ratio s_c is given by

$$s_{\mathrm{c}} = \frac{V}{r_{\mathrm{c}}^2 \cdot \omega^2 \cdot \ln(r_2 / r_1)}, \qquad (2.1)$$

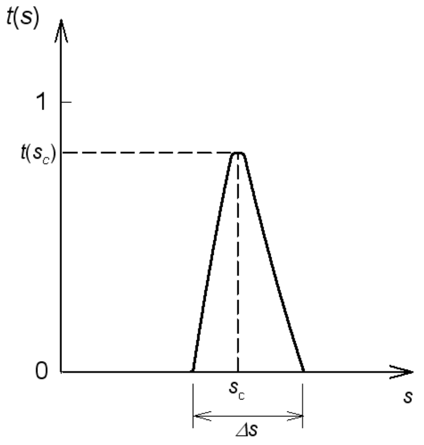

Figure 2.1 Typical appearance of the APM transfer function.

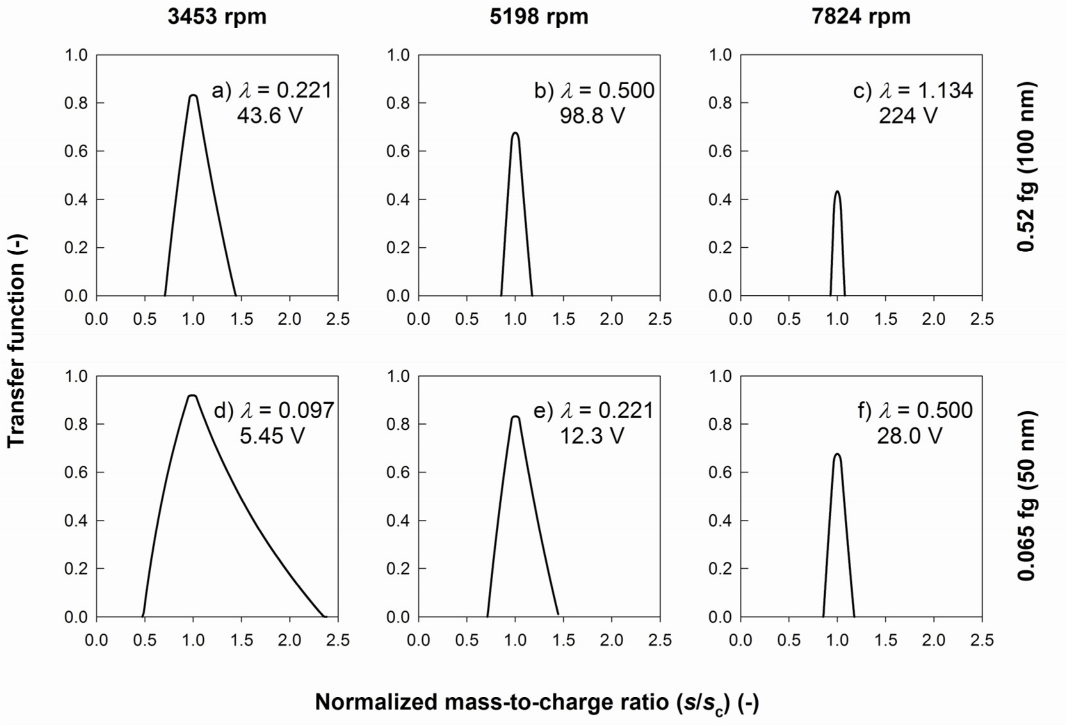

Figure 2.2 Examples of APM transfer functions obtained by a theoretical calculation assuming laminar parabolic flow. The plots are for singly-charged particles of 100 nm (top) and 50 nm (bottom) of the density of 1 g/cm^3. The voltage value in the plots corresponds to the voltage for s_c for the specified rotation speed and the λ value of each plot.

and the shape of the transfer function could be determined by the classification performance parameter

$$\lambda = \frac{2\tau \cdot \omega^2 \cdot L}{\bar{v}} \tag{2.2}$$

where V the voltage between the electrodes, ω the rotational speed, r_1 and r_2 the inner and outer radius of the electrode gap, and $r_c = (r_1 + r_2) / 2$, τ the particle relaxation time, L the axial length of the electrode gap, and $\bar{v}$ the mean velocity of the aerosol flow through the electrode gap.

Figure 2.2 illustrates APM transfer functions that were calculated for different operating conditions. The following assumptions were made for the calculation:

- Particles are singly charged. This assumption makes one-to-one correspondence of the mass-to-charge ratio s to mass m by $s = m/e$, where e represents an elementary charge, i.e., 1.602×10^{-19} C.
- Particles are spherical.
- The density of particles is 1 g/cm^3.
- The APM under consideration in this chapter is the one called "APM Model 3600" by Kanomax Japan Inc., which has the classification space of the following dimensions: $r_1 = 50$ mm, $r_2 = 52$ mm, $L = 250$ mm.
- The aerosol flow rate in the APM, Q, is 1 L/min.
- The gas is the air.
- Brownian diffusion of particles is negligible.

Note that the horizontal axes for the APM transfer functions in Figure 2.2 are normalized by s_c. The particle size corresponding to s_c is 100 nm (0.52 fg) for the plots in (a)-(c) (top row), whereas that is 50 nm (0.065 fg) for the plots in (d)-(f) (bottom row). As expressed by Equation 2.1, the mass of particles being classified by the APM depends on both angular velocity ω and voltage V, and there are many possible combinations of ω and V that result in classification of the same mass. The transfer functions shown in Figure 2.2 were calculated for classification of the two sizes at three different rotation speeds. For each plot, the λ value is shown that corresponds to each classification condition. For both particles, the λ value increases as the rotational speed becomes high. As a result, the resolution increases (i.e., the width of the transfer function becomes narrower), whereas the penetration decreases (i.e., the height of the transfer function becomes shorter). It can also be seen in Figure 2.2 that transfer functions of an essentially identical shape are obtained by adjusting the rotation speed and matching the λ values for particles of different masses when expressed in s/s_c scale, as shown by the cases of (a) and (e), or (b) and (f). As described above, the APM can classify particles of different masses with almost the same classification performance if the λ values are set equal.

2.3 Classifiable Mass Range and the Operation Diagram of the APM

Before considering the classifiable mass range of the APM, let me briefly review the constraints on the DMA that set its classifiable size limits. The maximum size limit, which is on the order of ~ 10^3 nm (i.e., ~ 1 μm) for typical DMAs, is partly determined by the dimensions of the classification space, the flow rates through the DMA, and the maximum voltage across the electrodes that can be applied without having electrical discharges. With regard to the minimum classifiable particle size, many DMAs suffer from reduction of resolution and penetration due to Brownian motion of particles and are not practically usable at ~ 1 nm. In summary, the upper and lower limits of particle size for DMA classification are affected by reasons that are not directly connected with the principle of electrical mobility classification.

Regarding the limitation of the APM, classification of particles by the APM according to their mass-to-charge ratio is also affected by factors that are not directly related to its operating principle. Since the mass-to-charge ratio for APM classification depends on ω and V as shown by Equation 2.1, operation of an APM is limited within the ranges of ω and V that are operable. For the case of APM Model 3600, the ranges are as follows:

- The range of the rotation speed is set by the constraints on the motor of the APM and is between 50 and 9500 rpm ($\omega = 0.13 - 25$ rad/s) for APM Model

3600. The rotation speed can not exceed this range.

- The voltage range for APM Model 3600 is from 0.3 V to 2 kV. The upper limit is the voltage without causing electrical discharge in the classification space of the 2-mm gap. The lower limit is the voltage determined based on the resolution of the voltage control by a computer, which is 0.031 V, which is the unit increment when the high voltage generator of -2 kV is controlled with a 16-bit resolution dc-voltage source. I set the lower limit voltage rather arbitrarily as the voltage of approximately ten times the unit increment.

The upper and lower limits of classifiable mass for APM Model 3600 can be calculated with Equation 2.1 by taking into consideration the above constraints of the rotation speed and voltage. That is, the upper mass limit is given by the lowest rotation speed and the highest voltage, whereas the lower mass limit is determined by the highest rotation speed and the lowest voltage. The upper and lower limits are 1.1×10^5 fg (equivalent to particle size of approximately 6 μm if the particle density of 1 g/cm^3 is assumed) and 4.8×10^{-4} fg (approximately 10 nm), respectively.

Figure 2.3a shows a log-log plot that visualizes the classifiable mass range for a given rotation speed. The upper and lower rotation speed limits are indicated by two vertical straight lines (marked as "50 rpm" and "9500 rpm"), whereas the upper and lower voltage limits are indicated by two parallel, downward-sloping straight lines (marked as "V = 0.3 V" and "V = 2000 V"). The downward slope indicates that the classifiable particle mass range shifts toward small values as the rotation speed increases. The area defined by the voltage and rotation speed limits forms a parallelogram in the log-log plot. The upper left corner corresponds to the upper limit of the classifiable mass, while the lower right corner corresponds to the lower limit of the classifiable mass. Hereafter, let me call this plot *the APM operation diagram*. Other lines and the cross-hatched area in Figure 2.3a will be discussed in Section 2.4.

2.4 Standard Operation Settings for Optimizing the APM Classification Performance

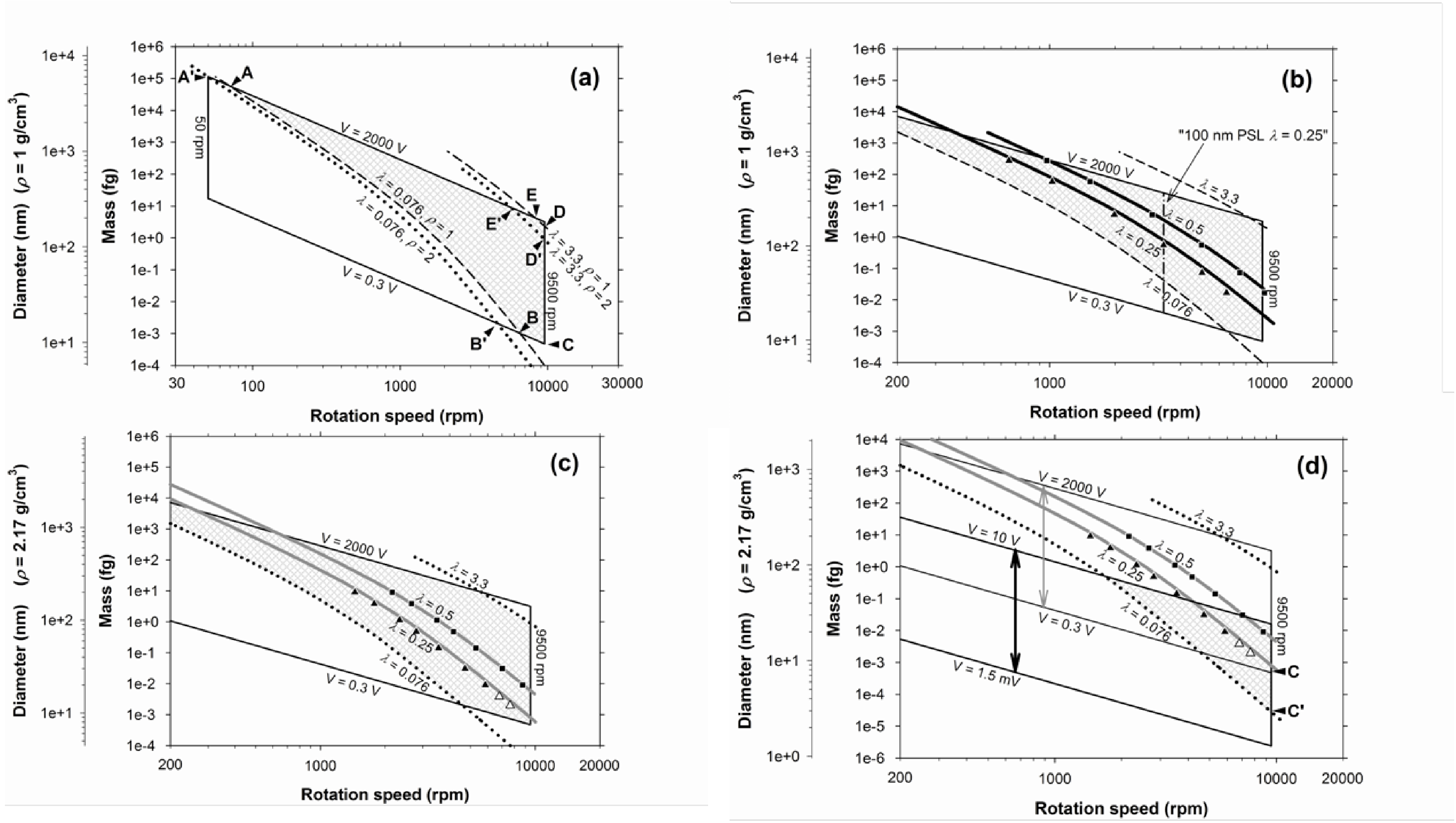

Figure 2.3 The APM operation diagrams: (a) The range that an APM can operate for mass classification bound by the constraints of the voltage and rotation speed (parallelogram), and the range with the additional restrictions regarding the resolution and penetration (cross-hatched area); (b) the operation conditions (thick solid lines) at $\lambda = 0.25, 0.5$ ($\rho = 1$ g/cm^3). The experimental conditions for PSL particles (triangles: $\lambda = 0.25$, squares: $\lambda = 0.5$); (c) the operation conditions (thick gray lines) at $\lambda = 0.25, 0.5$ ($\rho = 2.17$ g/cm^3) and the experimental conditions for NaCl particles; (d) the APM operation range (cross-hatched area) when the APM classification voltage was supplied directly by a 0-10-volt dc voltage generator on a computer.

2.4.1 Upper and Lower Limits of λ

It can be read from Figure 2.3a that classification of particles of 10 fg, as an example, can be achieved with the voltage within the operable range of 0.3 - 2000 V as long as the rotation speed falls between approximately 70 to 5000 rpm. However, as discussed in Section 2.2, the classification performance characteristics for particles of the same mass vary depending on the APM rotation speed setting. In other words, at low rotation speeds, the λ value is small, which means the penetration is high, but the resolution may be too low. In contrast, at high rotation speeds, the λ value is large, which means the resolution is high, but the penetration may be too low. The APM cannot be used as a classifier in practice if the resolution or penetration is too low. Accordingly, particle classification by the APM should be further bound by conditions that both the resolution and penetration should not be excessively low, which can be achieved by keeping the λ value within some range. In the following, let me consider the range of λ for good classification performance by the APM.

A parameter which is defined as $s_c/\Delta s$, where Δs represents the base width of a transfer function (Figure 2.1), is a good indicator to quantify the resolution, and the larger this parameter is, the higher the resolution of the APM. This parameter is called the APM resolution hereafter. Required resolution for the APM may vary depending on the application of the APM classification. For a discussion in this chapter, let me consider the case that the APM resolution should be 0.5 or greater. If the transfer function is perfectly symmetric with respect to s_c, when the APM resolution is 0.5, the left-hand-side edge of the transfer function reaches to the origin, which means particles of very small masses would penetrate through the APM with non-zero probabilities, which is not a very good classification. Since actual transfer functions are not perfectly symmetric and are somewhat skewed, the left-hand side of the transfer function falls to zero before reaching the origin. The transfer function at the APM resolution of 0.5, which corresponds to the λ value of approximately 0.076, would look similar to the transfer function shown in Figure 2.2d for which $\lambda = 0.097$ and $s_c/\Delta s = 0.56$. If I assume that the APM resolution should be 0.5 or greater, the λ value should be 0.076 or greater.

Required penetration for the APM also varies depending on the application of the APM classification. Therefore, let me consider the case that the height of transfer function, $t(s_c)$, should not be less than 0.1. This lower limit of the height corresponds to the λ value of about 3.3. By setting the λ value less than 3.3, the penetration of 0.1 or greater by $t(s_c)$ can be achieved.

The above restrictions on the λ value are illustrated in Figure 2.3a by curved lines. The λ value is a function of the APM rotation speed as expressed by Equation 2.2 and is also associated with particle mass and density through the relaxation time (τ). For a given density, a unique curve can be determined for a constant λ value. A pair of dashed curves in the APM operation diagram in Figure 2.3a represents conditions for λ values of 3.3 and 0.076 in the case that the density is 1 g/cm^3. These curves slope downward more steeply than the lines of the 0.3-V and 2-kV voltage constraints.

The range in which APM Model 3600 can operate with a sufficiently high resolution and penetration is indicated by the cross-hatched area enclosed by ABCDE, which is the area enclosed by the pair of dashed curves within the parallelogram derived from the constraints of the rotation speed and voltage. Point A in Figure 2.3a, which is the intersecting point between the upper voltage limit and the lower λ limit, corresponds to the maximum classifiable mass. (The second vertical axis in Figure 2.3a provides the relationship between mass and diameter for the stated density.) This mass is approximately 6.2×10^4 fg (equivalent to the particle size of 4.9 μm) and is slightly smaller than the maximum mass that has been determined from the previously obtained rotation speed and voltage constraints. The minimum mass is defined by Point C, which is the intersecting point between the lower voltage limit and the upper limit of the rotation speed, and is 4.8×10^{-4} fg (particle size of 9.7 nm); the λ-value restrictions did not affect the minimum mass. As pointed out above, the upper and lower limit values of λ may vary depending on the application of the APM classification, and therefore the upper and even lower masses may change. However, the above discussion provides a good illustration of how the voltage and rotation speed limits and the λ-value restrictions interact in the diagram and determine the mass range.

When a different density is assumed, the corresponding curves for λ = 3.3 and 0.076 shift in the diagram. Two dotted curves in Figure 2.3a are for the two λ values when the density is assumed to be 2 g/cm^3. When these dotted curves are compared with the dashed curves for the density of 1 g/cm^3, the curve for λ = 0.076 shifts from A - B to A' – B', while the curve for λ = 3.3 shifts from D – E to D' – E'. As a result, the area enclosed by A'B'CD'E' defines the operable range for the density of 2 g/cm^3. Though the point indicating the maximum classifiable mass shifts from Point A to Point A', the minimum mass does not change and remains at Point C. The corresponding particle size changes to 7.7 nm because the density is different, though. The mass for Point A' coincides with the upper limit of mass, 1.1 × 10^5 fg (particle sizes of 4.8 μm), that has been determined previously from the constraints of the rotation speed and voltage.

The above-described three conditions, i.e., the constraints on the rotation speed and voltage, and the somewhat arbitrary restriction on the λ value, constitute the major factors for determining the range operable for the APM and the classifiable particle mass limits. The following lists four other factors that may further narrow the APM operation range, which I do not discuss here in detail:

- When an APM is used in combination with a DMA, the usable mass range of the APM may be restricted by the classifiable particle size range of the DMA, especially at the upper limit. If, for example, the upper limit of the DMA is 1 μm, the maximum mass would be 5.2 × 10^2 fg for the density of 1 g/cm^3, or 1.1 × 10^3 fg for the density of 2 g/cm^3.
- In the low rotation speed region, the gap is narrow between the curve for λ = 0.076, which sets the lower mass limit at most of the rotation speed setting, and the line of V = 2000 V, which sets the upper mass limit at most of the rotation speed setting. This implies that the dynamic range may be too narrow in the low rotation speed range when the APM is used to obtain mass spectra by changing the voltage while the rotation speed is maintained constant. It can be seen in Figure 2.3a that a rotation speed of at least 500 rpm is required in order to have a dynamic range interval of at least a decade of the mass for particles of

the density of 1 g/cm^3.

- In curved flow paths inside the APM before and after the classification space, heavy particles having large aerodynamic diameters may be lost by impaction to wall surfaces due to their large inertia. In addition, for the Couette centrifugal particle mass analyzer (CPMA) [2], significant losses were found to occur in the instrument before and after the classification space due to the centrifugal forces at very high rotation speeds even with small particles [3]. The motion of large particles in the APM may also be affected by the gravity. These effects may reduce classification performance of the APM.
- At very small particle sizes, the resolution and penetration of the APM may decrease due to Brownian diffusion of particles, which may make the APM practically useless as a classifier. [4]

Since the last two of the above four restrictions have not been fully analyzed, they are investigated experimentally in Section 2.5 below.

2.4.2 Optimizing the APM Classification Performance

The preceding section discussed the upper and lower limits of λ, and the transfer function varies largely in this range. In this section, let me seek for optimum operations of the APM that would ensure both resolution and penetration are sufficiently high. Since the APM is often used in combination with a DMA, I consider the case that a DMA is used upstream of the APM to classify particles at some size, while a CPC is connected to the outlet of the APM so that the APM and CPC make mass spectrum measurement of particles that are classified by the DMA. In this instrument system, one possible consideration in choosing the λ value of the APM is to make the APM's resolution match the resolution of the DMA. The reason for this is because we do not gain much information by having the APM resolution much higher than that of the DMA, while we may lose some information if the APM resolution is significantly lower than that of the DMA. If I assume that the DMA is operated with the ratio of the sheath-air flow rate to the aerosol flow rate of 10:1, the mobility resolution of the DMA expressed in electrical mobility, $Z/\Delta Z$, is 10, where Z represents the centroid electrical mobility of the transfer function whereas ΔZ represents the half width of the base of the transfer function [5]. Since the slip correction coefficient is constant against and inversely proportional to particle size in the continuum and free molecular regimes, respectively, electrical mobility is inversely proportional to the first to second power of particle size depending on the flow regime. Therefore, the above ratio is equivalent in terms of particle size d to $d/\Delta d \approx 20 - 10$, i.e., nearly 20 for particles of 30 nm or smaller, and nearly 10 for particles of 1000 nm or larger. Since the particle mass m is proportional to the third power of its size, the above ratio is equivalent in terms of mass resolution to $m/\Delta m \approx 20/3 - 10/3$. This ratio is equivalent in terms of the APM resolution $s_c/\Delta s$ to $s_c/\Delta s \approx m/(2\Delta m) \approx 20/6 - 10/6 = 3.33 - 1.67$. (Note that Δs represents the full base width of the transfer function, while ΔZ, Δd and Δm represent the half base width.) The $s_c/\Delta s$ values of 3.33 and 1.67 are equivalent to λ values of approximately 0.5 and 0.25, which are shown in Figures 2.4a and 2.4b, respectively. These figures also show that the maximum penetrations, $t(s_c)$, corresponding to these λ values exceed 0.6, which is quite good. As a result, I recommend to maintain the λ value within the range between 0.25 and 0.5 for optimal classification performance of the APM.

In Figure 2.3b, curves in thick lines representing the relationship between rotation speed and mass for the λ values of 0.25 and 0.5 with the assumed particle density of 1 g/cm^3 are added to the APM operation diagram. From the diagram, the rotation speed that should be set on the APM can be read if there is some knowledge of the mass of particles to be classified (from the size and a rough idea of the density, for example). Figure 2.3b also shows how the curves of $\lambda = 0.25$ and 0.5 overlap with the operable range (i.e., the cross-hatched area) determined in the preceding section. The curves for the two λ values cover a majority of the classifiable mass range, and the mass ranges are from 0.02 to 300 fg for $\lambda = 0.5$ (equivalent to particle sizes of 36 to 800 nm with the particle density assumed to be 1 g/cm^3), and from 0.003 to 2000 fg for $\lambda = 0.25$ (equivalent to particle sizes of 20 to 1600 nm with the particle density assumed to be 1 g/cm^3).

Point C, which corresponds to the smallest classifiable mass, does not lie on the above curves of $\lambda = 0.25$ and 0.5. For the density of 1 g/cm^3, Point C corresponds to the λ value of 0.126. Figure 2.4c shows how the transfer function appears when $\lambda = 0.126$. Since the λ value is less than 0.25, the resolution is not as good as that within the optimal condition (Figures 2.4a and 2.4b).

While the λ value can be selected by the user, for many APM operations, the density of particles to be classified is often totally unknown at the very beginning. Without knowing the density, it is impossible to optimize the λ value. Therefore, optimization of the λ value requires a preliminary step of measurement according to the following procedures:

1) Carry out a measurement of the particle mass at an arbitrary rotation speed within its operable range and obtain the approximate mass.
2) With the particle mass from the above measurement and the mobility-equivalent diameter set on the DMA, calculate the particle relaxation time τ. Use the following equation to calculate τ:

$$B = \frac{C_\mathrm{c}}{3\pi\mu d_\mathrm{me}} \tag{2.3}$$

$$\tau = mB \tag{2.4}$$

   where d_me is the DMA classified particle size, μ is the dynamic viscosity of air, and B is the mechanical mobility of the particles from the DMA.
3) Using Equation 2.2, determine the APM rotation speed corresponding to $\lambda = 0.5$ (or $\lambda = 0.25$, whichever desired) for τ determined in Step 2 above.
4) By setting the APM rotation speed at the value determined in Step 3 above, an optimal operation of the APM would be achieved.

2.5. Experimental Evaluation of Classification Performance of the APM

2.5.1 Methods

In order to verify the validity of the classifiable mass ranges and the optimization of the classification performance that were theoretically derived in

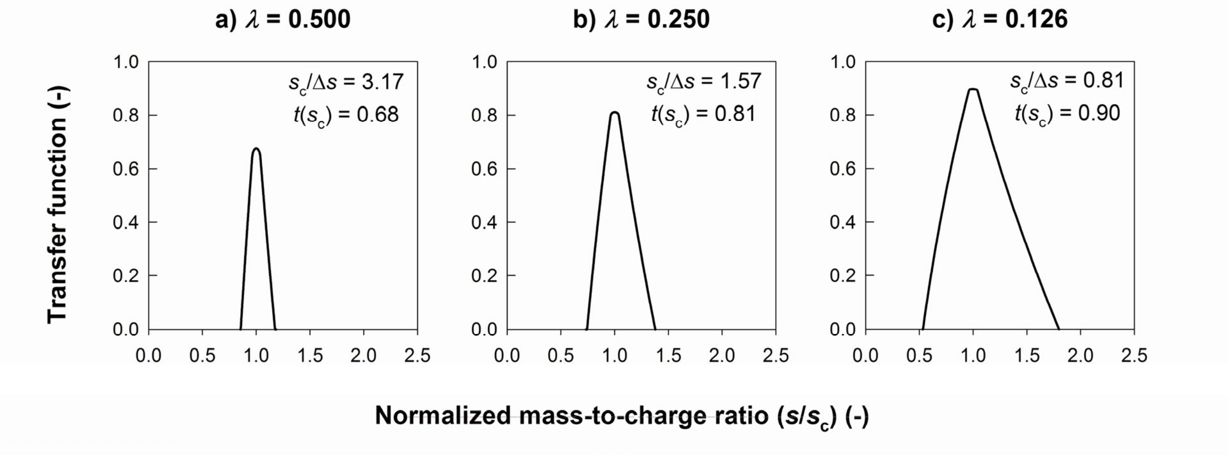

Figure 2.4 Transfer functions that correspond to the APM classification performance parameter λ of 0.5, 0.25, and 0.126, respectively.

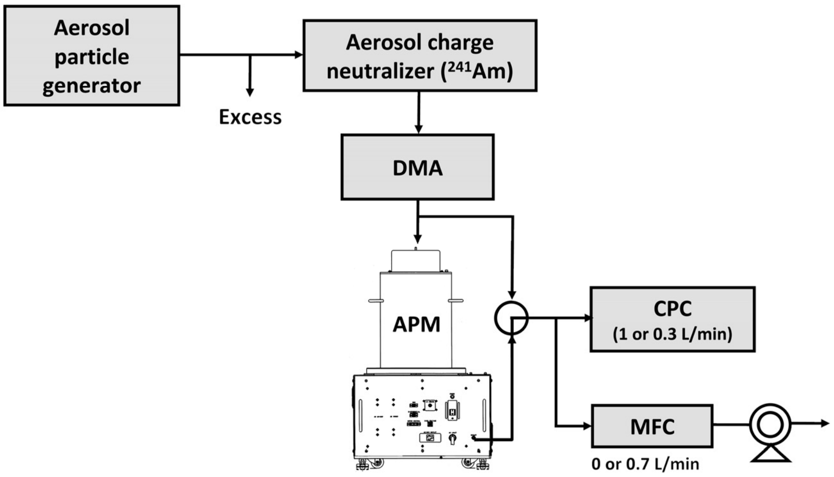

Figure 2.5 Experimental setup for evaluating the APM.

Sections 2.3 and 2.4, experimental investigations were carried out with laboratory-generated particles of masses that fell within the estimated classifiable mass range and that were able to be estimated rather easily from the knowledge of the size and the material density. In the experiments, I measured the relationship between the voltage applied to the APM, V, and the particle concentration at the APM outlet, $C_{N,}$, under a constant rotation speed condition for each particle size and material, while the particle concentration was measured at a discrete set of APM voltages. The voltage was changed stepwise and always upward in each individual measurement. A set of $C_N - V$ pairs is defined as a *system response spectrum*.

The following three levels of criteria were used to judge whether or not the APM was able to classify particles successfully:

1) Check if the obtained APM system response spectrum had a single-peak bell shape. This is a very loose criterion. However, I added this criterion because APM spectra do not have bell shapes but exhibit somewhat flat spectra even though DMA-classified quasi-monodispersed particles are introduced into the APM, which occurs sporadically, only at very high rotation speeds. I have not identified the reason for this phenomenon. This first step of the APM operation check is for detecting such abnormal behaviors.
2) Check if the particle mass found by an APM measurement matches the mass determined or estimated by other different methods. This corresponds to testing the APM performance in the 1st moment of the transfer function.
3) Check if the penetration and resolution of APM system response spectra match those predicted with the theoretically-calculated transfer function. This test is particularly important for small particles because penetration and/or resolution may be largely affected by Brownian diffusion at small sizes. The penetration and resolution tests correspond to testing the APM performance in the 0th- and 2nd moments of the transfer function, respectively.

In the experiments, six sizes of polystyrene latex (PSL) particles in the size range from 29 to 791 nm by JSR Co. (Table 2.1), and sodium chloride (NaCl) particles of sizes in the range from 12 – 200 nm were used to check whether or not an APM may meet the above three criteria. The λ value was set at 0.22 or 0.49 that roughly matched the optimum λ values determined in Section 2.4. Since the density of PSL particles are approximately 1 g/cm^3, Figure 2.3b, i.e., a diagram for the density of 1 g/cm^3, is used to illustrate the relationship between the expected masses and the rotation speed to be set for the PSL particles of the six sizes: The six triangles indicate the points for $\lambda = 0.22$, whereas the six squares indicate the points for $\lambda = 0.49$. These triangles and squares span across the most of the classifiable mass range for $\lambda = 0.22$ and $\lambda = 0.49$. In Figure 2.3b, the vertical dashed-dotted line marked by "100 nm PSL $\lambda = 0.25$" represents the operation path for measurement of 100 nm PSL particles at $\lambda = 0.25$, on which the voltage was changed between 0.3 and 2000 V while the rotation speed was fixed constant at about 3300 rpm. The APM was operated in a similar way for the other particle sizes and λ values, i.e., by changing the voltage at a constant rotation speed so as to obtain an APM system response spectrum.

For NaCl particles, their material density (2.17 g/cm^3) was used as the density for calculating the relationship between the rotation speed and expected mass. Figure 2.3c shows the several operation points for NaCl particles at $\lambda = 0.22$ and 0.49 by triangle and square symbols, respectively. In this figure, the cross-hatched area represents the classifiable mass range that was calculated for density of 2.17 g/cm^3, whereas the thick gray curves represent the optimal operation curves of $\lambda = 0.25$ and 0.5. Note that there are more triangles than squares, which is because NaCl particles of 12 and 15 nm, which correspond to the points marked by open triangles (Δ), were able to be measured only at $\lambda = 0.25$. At $\lambda = 0.5$, the rotation speed exceeded the upper limit at these sizes.

Figure 2.3c shows that the points for 12- and 15-nm NaCl particles (open triangles) are close to the "V = 0.3 V" constraint. This may result in a system response spectrum which misses several data points at voltages below 0.3 V that are needed to complete the whole spectrum. Since determining the width of the system response spectra was one of my experimental objectives, it was desirable to record the whole

Table 2.1 List of PSL particles used in this study and their literature values of diameter, density, and coefficient of variation (CV); reference mass values obtained by the electro-gravitational aerosol balance (EAB) method and by calculation as mass of spherical particles of DMA-classified size and the literature density value; mass obtained by measurement with APM; and comparison of the mass by APM to reference mass values.

JSR STADEX Product Name	Values provided by the manufacturer			Reference mass values				APM classification performance parameter λ	Mass by APM		Ratio of number-averaged mass by APM to reference value	
	Number-averaged diameter	Density	CV	Mass by EAB	Diameter by DMA	Density assumed	Mass from diameter and density		Number-averaged mass	Mode mass	Ratio to mass by EAB	Ratio to mass from diameter and density
	(nm)	(g/cm^3)	(%)	(fg)	(nm)	(g/cm^3)	(fg)	(-)	(fg)	(fg)	(-)	(-)
SC-0030-A	29	1.115	13.74		30.6	1.115	0.0167	0.22	0.0148	0.0170		0.884
								0.49	0.0157	0.0149		0.939
SC-0050-D	48	1.061	15.57		51	1.061	0.0737	0.22	0.0748	0.0743		1.015
								0.49	0.0756	0.0750		1.026
SC-0100-D	100	1.060	2.47		100	1.060	0.555	0.22	0.548	0.594		0.988
								0.49	0.559	0.552		1.008
SC-021-S	208	1.054	1.81	5.195	208	1.054	4.97	0.22	5.05	5.79	0.971	1.016
								0.49	5.10	5.21	0.982	1.027
SC-048-S	479	1.054	1.00	58.43	479	1.054	60.7	0.22	60.5	58.4	1.036	0.998
								0.49	61.0	59.9	1.044	1.006
SC-079-S	791	1.058	1.02		791	1.058	274	0.22	275	259		1.002
								0.49	270	262		0.985

spectrum including both ends. To bring down the lower voltage limit for 12- and 15-nm NaCl particles, I changed the APM voltage generator: The step-up high-voltage generator, which was the regular voltage supply of the APM, was bypassed, and the dc voltage output of 0–10 V from a digital-to-analog converter on the controlling computer was directly connected to the APM electrodes. As a result, both the upper and lower voltage limits were reduced by a factor of 1/200 to 10 V and 0.0015 V, respectively, which is illustrated in Figure 2.3d. Although the cross-hatched area became smaller, it became less likely that the voltage constraint may limit the dynamic range of measured spectra for 12- and 15-nm particles. The second voltage control method shifts the smallest classifiable mass at point C to a smaller mass at the new point C’ in the diagram, which corresponds to 2.8×10^{-5} fg (i.e., particle sizes of 3 nm for the density of 2.17 g/cm^3).

The experimental setup is shown in Figure 2.5. Particles generated by an aerosol generator were first fed into the aerosol charge neutralizer that housed a 3-MBq Am-241 alpha particle source. After the particles were classified by a DMA (Model 3071 or 3081, TSI Inc.) according to their size, they were introduced into the APM. Except 29-nm PSL particles, which was aerosolized by an electrospray aerosol generator (Model 3480, TSI Inc.), particles were aerosolized by a Collison-type atomizer (Model 3076, TSI Inc.). The DMA's sheath-air flow rate was usually set at 10 L/min, though it was 5 L/min and 3 L/min for 479-nm and 791-nm PSL particles, respectively. To maintain the aerosol flow rate in the APM at 1 L/min, either one of the following methods was employed: (a) direct connection of a CPC of 1 L/min (Model 3010, TSI Inc.) to the APM outlet, or (b) connection of a CPC of 0.3 L/min (Model 3022A in low flow mode, TSI Inc.) and a 0.7-L/min excess air flow line to the APM outlet. Direct connection of the APM’s aerosol inlet with the DMA’s mono-disperse aerosol outlet made it possible to also set the aerosol flow rate in the DMA at 1 L/min. The particle concentration was measured both at the inlet and at the outlet of the APM by turning the three-way valve shown in Figure 2.5 and switching the connecting point of the CPC between the outlet of the DMA and the outlet of the APM.

For assuring accuracy in the sizing by the DMA, I calibrated the voltage applied to the DMA and the sheath-air flow rate with a volt meter and a soap-film flow meter, respectively, both of which were calibrated against higher calibration standards. I also carried out size distribution measurement of the PSL particles with the DMA and CPC, and confirmed that the number-averaged diameter was essentially equal to values given by JSR Co., that are traceable to national standards.

In mass measurement of the PSL particles by the APM, the voltage on the DMA for each particle size was determined based on the following:

- For the 100-nm PSL particles, the voltage was set to the value that corresponded to particle size of 100 nm, since the particle concentration at the DMA outlet was found highest at this voltage. The size of 100 nm agreed well with the number-averaged size by JSR (Table 2.1).
- For the 208-nm particles, while the voltage that corresponded to particle size of 206 nm maximized the particle concentration at the DMA outlet, the voltage for the particle size of 208 nm, which is the number-averaged size by JSR (Table 2.1), was set on the DMA since the particle concentration at 208 nm was only slightly less than that at 206 nm .
- For the 479-nm and 791-nm particles, the reduced classification resolution of the DMA, which was caused by setting the sheath-air flow rate of the DMA at 5 or 3 L/min while the aerosol flow rate was maintained at 1 L/min, did not allow determination of the voltage that would maximize the particle concentration at the DMA outlet. At these sizes, the voltage was set to the value that corresponded to the number-averaged diameter by JSR.
- In the case of the 29-nm and 50-nm particles, since they have skewed, asymmetric size distributions, the particle size for the DMA voltage that maximized the particle concentration at the DMA outlet differed from the number-averaged diameter by JSR. For APM evaluation, the DMA voltage was set at the value for the maximum concentration at the DMA outlet.

Based on the observation of good agreements with the 100-nm and 208-nm particles between the particle size that maximized the concentration at the DMA outlet and the number-averaged diameter by JSR, it was concluded that the accuracy of sizing by the DMA used in this experiment was sufficiently high. Therefore, for the experiment with NaCl particles, the size of particles classified by the DMA was assumed to be accurate and was not corrected at all.

For the APM, a calibrated voltmeter was used to calibrate the voltage that was applied to the APM electrodes and generated a correction equation, which was found especially important at low voltages since there was an offset of a few volts. For the APM rotation speed, a calibrated tachometer was used to calibrate the rotation speed measured by the rotary encoder in the APM.

A calibrated soap-film flow meter was used to calibrate flow rates at several points in flow paths in the experimental setup illustrated in Figure 2.5.

2.5.2 Results

2.5.2.1 Results with PSL Particles

APM system response spectra for the PSL particles of the six sizes are shown in Figure 2.6. The spectra in Figures 2.6a and 2.6b were obtained when the operation of the APM was targeted at λ = 0.22 and 0.49, respectively. In the figures, the voltage applied to the APM is plotted on the horizontal axis, whereas the ratio of the particle concentration at the APM outlet to that at the inlet is plotted on the vertical axis. Different symbols represent data for PSLs of different sizes. It was confirmed by experimental data in Figure 2.6 that all the spectrum curves of the six sizes passed the first criterion in Section 2.5.1, i.e., "Check if the obtained APM system response spectrum had a single-peak bell shape."

Next, the measured spectra were analyzed to obtain representative values of particle mass. An APM system response spectrum can be expressed by the following integral equation that has the product of the mass distribution of incoming particles and the APM transfer function as its integral kernel as:

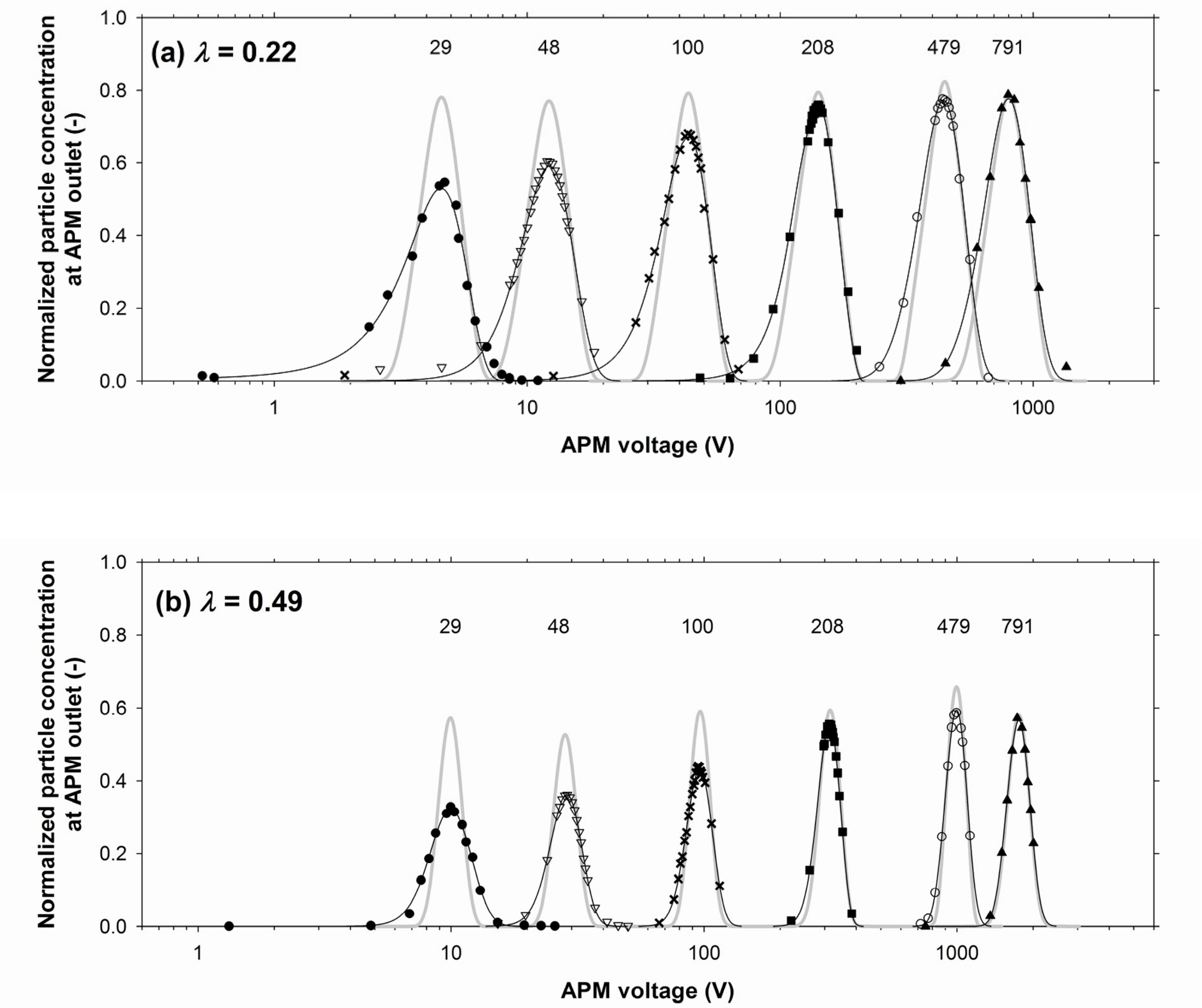

Figure 2.6 APM spectra for the PSL particles when the APM classification performance parameter λ was set at (a) 0.22 and (b) 0.49. The numbers above the spectra are the nominal sizes of the PSL particles. Experimental data are shown with symbols, while the spectra obtained by the FIT_APM and SIM_APM programs are shown with thin solid and thick gray lines, respectively (see text for details).

$$C_N(V) = \int_0^\infty n(m) \cdot \Omega_{\mathrm{APM}}(m;V)\,\mathrm{d}m \qquad (2.5)$$

where $C_N(V)$ represents the particle concentration at the APM outlet when the APM mass classification voltage is set at *V*, $n(m) = \mathrm{d}C_N / \mathrm{d}m$ the mass distribution of particles at the APM inlet, and $\Omega_{\mathrm{APM}}(m;V)$ the APM transfer function when the classification voltage is *V.* A computer program named *FIT_APM*, which was developed at National Institute of Advanced Industrial Science and Technology (AIST), was used to analyze measured APM spectra. The FIT_APM program determines parameters of a mass distribution, such as the mean and standard deviation, by applying the least square fitting method to data points of measured spectra. This program assumes either one of the following three distributions as a function of the particle mass distribution $n(m)$: (i) an asymmetric normal distribution in mass, (ii) an asymmetric normal distribution in particle size, or (iii) a lognormal distribution in mass, which is also a lognormal distribution by particle size when particle density is assumed constant. In the least square fitting, the mobility in the transfer function is determined on the assumption of constant density for liquid droplets and PSL particles, or constant mobility when a DMA is used upstream of the APM. In the analysis, I assumed an asymmetric normal distribution in mass and a constant density. The FIT_APM program gives the number-averaged mass and the mode mass as its calculation results. Among these two values, I chose to use the number-averaged mass as the representative value to be compared with reference mass values. The mass values, both number-averaged and mode, obtained by the FIT_APM program are given in “Mass by APM” column of Table 2.1.

Among the six PSL particles, the 208-nm and 479-nm particles had been measured by the electro-gravimetric aerosol balance (EAB) method [6], which I consider the most accurate method to determine the particle mass. I compared the mass values measured in this study with the values by the EAB method. For all the six PSL particles, I calculated the volume of spherical particles having the particle size classified by the DMA and estimated their mass by multiplying the volume by the density provided by JSR. The measured masses were compared with the above reference mass values, which are listed in Table 2.1. Figure 2.7 plots the ratio of measured masses to the reference mass values on the vertical axis with the DMA-classified particle size on the horizontal axis. In this figure, the solid symbols indicate that the ratios were calculated with reference mass values by the EAB method, whereas the open symbols indicate the ratios were calculated with reference mass values determined from particle size and density. Except those for the 29-nm particles, the ratios of the other five particles were about unity, and the agreement of the measured masses to the reference values were within ±5 % regardless of the λ value. As a result, it was concluded that the second criterion in Section 2.5.1 "Check if the particle mass found by an APM measurement matches the mass determined or estimated by other different methods." was fulfilled. The ratios for 208-nm and 479-nm particles were not very different between the value by the EAB method and that by size and density. On the other hand, the underestimation for the 29-nm particles was as large as about 10 %.

As a result of its calculation, the FIT_APM program outputs four parameters that describes the asymmetric normal distribution obtained by the least-square fitting, i.e., the total number concentration, mode mass, and the mean and the difference of the standard deviations for the left- and right-hand-side fractions of the distribution. The program also performs convolution of the obtained mass distribution expressed by the four parameters with the APM transfer function, so as to reconstruct the APM system response spectrum and outputs it as part of the analysis results. Thin black curves in Figure 2.6 show the reconstructed APM spectra. The reconstructed APM spectra of all particles fit the experimental data points very well.

In addition to the thin black curves, Figure 2.6 also shows thick gray curves. These curves represent the spectra that were expected to be observed if the APM's classification performed exactly as the theory predicts, assuming that the size distribution of incoming particles is known accurately. I used a computer program named *SIM_APM*, which was also developed at AIST, to calculate these spectra. The SIM_APM program calculates the mass distribution $n(m)$ on the basis of a given particle size distribution and density, and calculates the APM spectrum by Equation 2.5

by performing convolution of the mass distribution with the theoretical APM transfer function $\Omega_{\mathrm{APM}}(m;V)$. To calculate the spectra shown in Figure 2.6, I assumed that the size distribution of the PSL particles was a normal distribution with the mean particle size and the standard deviation given in the catalog by JSR. I then superimposed onto the size distribution the theoretical transfer function of the DMA which was set to classify the mean particle size with the ratio of the sheath air to the aerosol flow rate of 10:1 (or, 5:1 for 479-nm particles and 3:1 for 791-nm particles), and gave it with a certain density value to the SIM_APM program. Comparison of the spectra calculated by the SIM_APM program with those which were experimentally obtained would enable me to judge whether the third criterion in Section 2.5.1, i.e., to check if the penetration and resolution of APM system response spectra match those predicted with the theoretically-calculated transfer function., was satisfied or not. It should be noted that, for the calculation of the theoretical spectra, I used density values that were calculated with the volume by the DMA-classified size and the mass observed in the analysis for Figure 2.7, in place of the values given by JSR. The reason for this was that the theoretical spectrum calculated with a density by JSR would be shifted horizontally against the corresponding measured spectrum, making the comparison of the shape of the curves difficult. The use of the observed density allowed to align the theoretical and experimental spectra for the same particle size horizontally in the plots.

When the shape of a thin black curve was compared with that of the corresponding thick gray curve for each particle size, the difference was rather large at sizes of 29 and 48 nm and was insignificant at larger sizes for both λ values. Thin black curves tended to have wider and shorter distribution curves as particle size decreased (29, 48, and 100 nm). Since the comparison of the curves is on the system response spectrum and not on the transfer function, this is not a direct evaluation of the transfer function. However, good agreements between theoretical and measured spectra at large sizes (> 100 nm) suggests that the actual APM transfer function was close to the theoretical one, and also that the estimation of the PSL size distribution given to the SIM_APM program was accurate. In the case of the smaller particles (29, 48, and 100

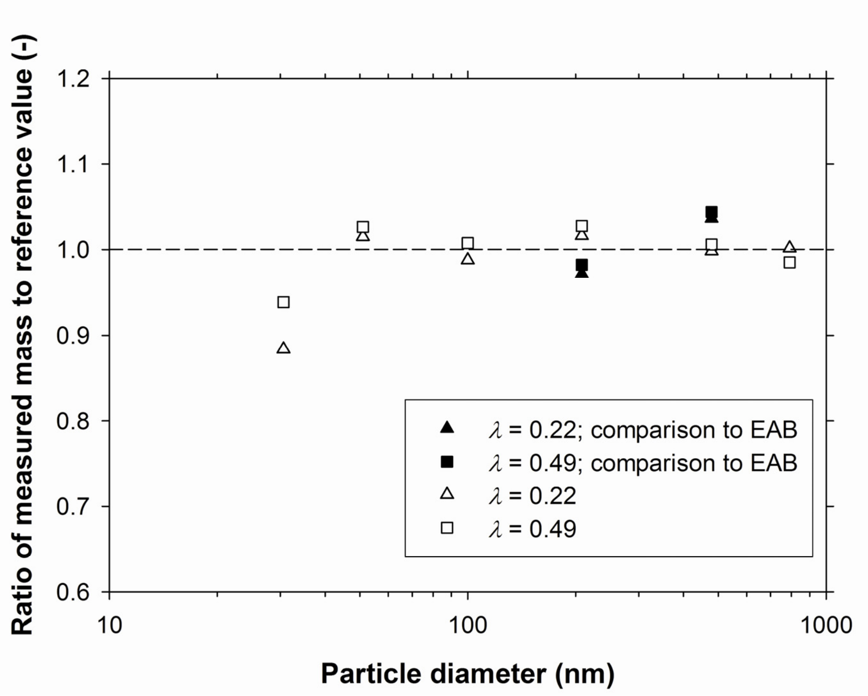

Figure 2.7 Ratio of the number-averaged mass experimentally obtained by the APM to the reference mass values for PSL particles. Note that the horizontal axis is the DMA-classified particle size listed in Table 2.1. The data for particles of nominal sizes of 29 and 48 nm are plotted at 30.6 and 51 nm, respectively.

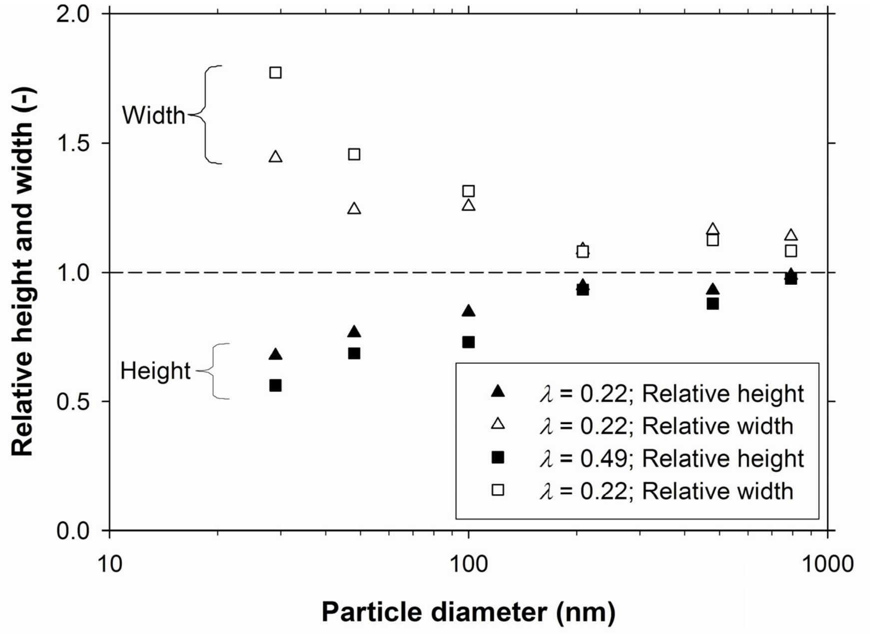

Figure 2.8 Ratio of the height and the full width at half maximum (FWHM) of the APM spectra obtained experimentally to those obtained by calculation assuming a size distribution, density, and the theoretical APM transfer function, in the case of PSL particles.

nm), while the possibility that the width of the particle size distribution was underestimated can not be totally ruled out, I believe it more likely that the reduced resolution and penetration occurred because of the Brownian diffusion of particles in the APM. The data for the largest particles (791 nm) did not show noticeable decrease of penetration, which implies that inertial losses, discussed in Section 2.4.1, did not occur in the APM even when particles as large as approximately 800 nm were classified.

Ratios of the height and the full width at the half maximum (FWHM) of the experimental APM spectra to those determined theoretically for each particle size are shown in Figure 2.8. This figure shows that the ratio approached unity as particle size increased, verifying that the spectra for larger particles can be estimated accurately by the theory. In contrast, the APM spectra became wider and shorter as particle size decreased. For the 29-nm particles, for example, the measured spectra had a width of approximately 1.5 to 1.8 times and a height of 0.5 to 0.7 times those of the theoretical spectra.

Lall et al. (2009) reported APM mass measurement results for 60-, 100-, and 300-nm NIST-standard or NIST-traceable PSL particles. They calculated the reference mass values as spherical particles having the certified size, assuming the particle density to be 1.05 g/cm^3. Comparison of the reference mass values with the masses by APM measurements revealed good agreement with an error of approximately 6 %, which is about the same as my result. Lall et al. also theoretically calculated transfer functions with Brownian diffusion of particles taken into consideration. They calculated APM spectra with the theoretical diffusive transfer functions and compared them with their measured spectra. While they discussed the effect of Brownian diffusion on the APM transfer function, their report does not discuss in detail the magnitude of the effect of Brownian diffusion on APM spectra, making it impossible to compare the results of their study with mine.

2.5.2.2 Results with NaCl Particles

Experimental results for NaCl particles are shown in Figure 2.9. As described in Section 2.5.1, particles in the range from 12 to 200 nm were size classified and used to evaluate the APM, and particles of 12 and 15 nm were used only in measurements at $\lambda = 0.22$. The experimentally obtained APM system response spectra are plotted with symbols. Although the spectra for 12 and 15 nm particles were spread widely, they form a single bell-shaped curve and barely fulfilled the first criterion in Section 2.5.1. I then calculated the number-averaged mass with the FIT_APM program in order to check whether or not the second criterion in Section 2.5.1 was satisfied. As the reference mass to be used for comparison, I initially calculated the mass of spherical particles having the DMA-classified size as their diameter and of the density of 2.17 g/cm^3 (Table 2.2). Figure 2.10a shows the ratio of the measured mass to the reference value with respect to the DMA-classified particle size. In the particle size range of 50 nm to 200 nm, where in the case of PSL particles the measured masses agreed very well with the reference values (Figure 2.7), the ratio stayed almost constant. The value of the ratio, however, was not unity but approximately 0.9. Part of the reason for this was probably because the particles were not spherical but cubic. I calculated the mass of cubic particles of the density of 2.17 g/cm^3 as another set of reference masses. This required the knowledge of the dynamic shape factor and volume-equivalent diameter of cubic particles at each DMA-classified size in the transition and free-molecular regimes. Derivation of the dynamic shape factor for cubes of a given volume-equivalent diameter was done by following the method provided by Dahneke [7-9] and equations given in DeCarlo et al. [10]. The volume-equivalent diameter for each DMA- classified size was obtained by solving the following equation:

$$\frac{d_{\mathrm{e}}\, \chi_{\mathrm{cube}}(d_{\mathrm{e}})}{C_{\mathrm{C}}(d_{\mathrm{e}})} = \frac{d_{\mathrm{DMA}}}{C_{\mathrm{C}}(d_{\mathrm{DMA}})} \qquad (2.6)$$

where d_{e} and d_{DMA} are the volume-equivalent diameter and DMA-classified size, respectively, is the slip correction coefficient at size d, and is the dynamic shape factor for cubes for the volume-equivalent diameter. The results of these calculations are summarized in Table 2.2. Figure 2.10b shows the ratio of the measured mass to the

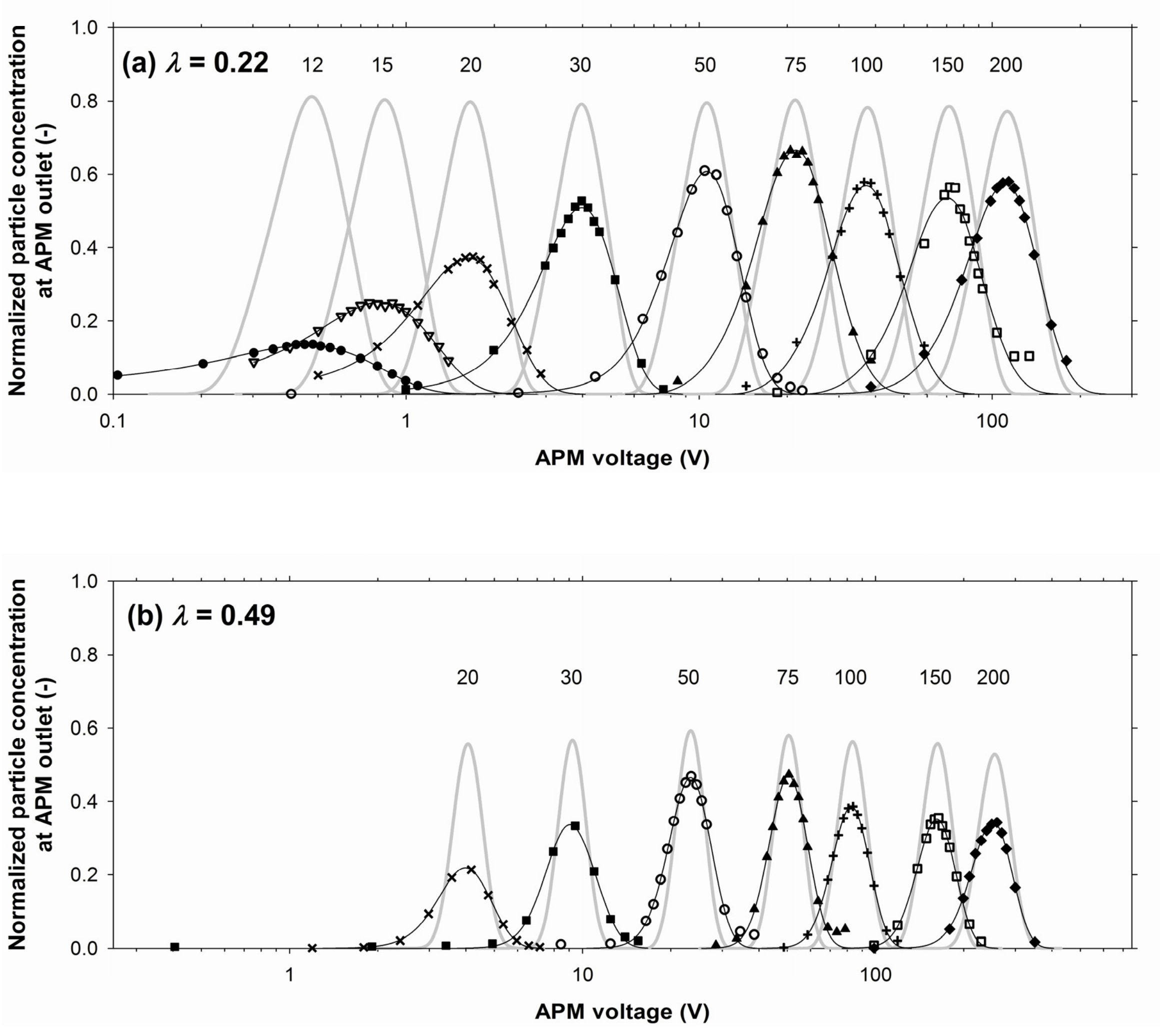

Figure 2.9 APM spectra for sodium chloride particles when the APM classification performance parameter λ was set at (a) 0.22 and (b) 0.49. The numbers above the spectra are the particle sizes at which the DMA upstream of the APM classified. Experimental data are shown with symbols, while the spectra obtained by the FIT_APM and SIM_APM programs are shown with thin solid and thick gray lines, respectively (see text for details).

Table 2.2 Results with sodium chloride particles in this study; mass obtained by measurement with APM; reference mass value calculated assuming that (a) the particles were spheres of the diameter of the DMA-classified size and of the density of sodium chloride (2.17 g/cm^3), and (b) the particles were cubes of the density of sodium chloride; and comparison of the mass by APM to reference mass values obtained with the two assumptions.

Diameter by DMA	APM classification performance parameter λ	Mass by APM		(a) Assuming spherical particles of diameter by DMA		(b) Assuming cubic particles			
		Number-averaged mass	Mode mass	Reference mass values	Ratio of number-averaged mass by APM to reference mass	Dynamic shape factor	Volume-equivalent diameter	Reference mass values	Ratio of number-averaged mass by APM to reference mass
(nm)	(-)	(fg)	(fg)	(fg)	(-)	(-)	(nm)	(fg)	(-)
12	0.22	0.00140	0.00108	0.00196	0.713	1.23	10.78	0.00142	0.984
	0.49	-	-		-				-
15	0.22	0.00274	0.00238	0.00383	0.715	1.23	13.48	0.00278	0.985
	0.49	-	-		-				-
20	0.22	0.00705	0.00653	0.00909	0.776	1.23	17.98	0.00660	1.067
	0.49	0.00773	0.00741		0.850				1.170
30	0.22	0.0263	0.0251	0.0307	0.857	1.22	26.98	0.0223	1.179
	0.49	0.0277	0.0255		0.903				1.241
50	0.22	0.124	0.116	0.142	0.873	1.21	45.02	0.104	1.196
	0.49	0.124	0.119		0.873				1.196
75	0.22	0.433	0.308	0.479	0.903	1.20	67.61	0.351	1.233
	0.49	0.427	0.405		0.891				1.216
100	0.22	1.046	0.766	1.14	0.921	1.19	90.26	0.835	1.252
	0.49	0.992	0.959		0.873				1.187
150	0.22	3.43	2.49	3.83	0.894	1.18	135.7	2.84	1.208
	0.49	3.34	3.24		0.871				1.176
200	0.22	8.00	6.74	9.09	0.880	1.16	181.4	6.78	1.180
	0.49	7.83	7.70		0.861				1.155

reference mass of cubic particles. The ratios increased by ~ 0.3 compared to those shown in Figure 2.10a, and exceeded unity at all sizes except 12 and 15 nm. I do not know why the ratios were greater than unity. Since I observed good agreements in the PSL experiment (except 29 nm) in the previous section between the APM classified mass and the reference mass value, it is unlikely that the reason for the excessive ratio was due to errors in APM mass classification. The exact reason was unknown, but perhaps because the particles were not perfectly cubic.

Although the ratio remained almost constant in the size range between 30 and 200 nm in both Figures 2.10a and 10b, it decreased as particle size decreased to 20 nm and further below. The result for the PSL particles in Figure 2.7 revealed that the ratio of the 30-nm particles was underestimated. These size dependent characteristics suggested a problem either in the accuracy of mass classification by the APM, or the calculation of reference mass values, which became worse at smaller sizes. While mass underestimation was not observed for 30 nm NaCl particles, it was observed for PSL particles of the same size. The difference may be attributable to the difference in their density, and because of the density difference the mass of NaCl particles is approximately twice that of PSL particles. The difference in the mass measurement results between the NaCl and PSL particles of the same size of 30 nm implies that the degree of mass underestimation might increase with decrease of particle mass. This issue of mass underestimation is currently under investigation.

The thin black curves in Figure 2.9 are fitted curves of the measured spectra by the FIT_APM program, and the thick gray curves in the same figure represent the theoretical spectra determined by the SIM_APM program, as in the same manner as those of Figure 2.6. The SIM_APM program calculated the mass spectra on the assumption that particle size distribution before the DMA was flat (constant) over the entire width of the DMA transfer function. The equation by Stolzenburg [11], which takes into account Brownian diffusion of particles, was used for the DMA transfer function. Similar to the measurement results for the PSL particles (Figure 2.6), the experimental and calculated spectra of the NaCl particles agreed better for large particles (50 - 200 nm) than for small particles (12 - 30 nm). When compared with calculated spectra, the experimental spectra were wider and shorter in the small particle range. However, even for large particles, the degree of agreement between measured and calculated spectra was not as good as that in the case of the large PSL particles of > 208 nm. Such difference in the agreement of the curves between the particles of the two different materials is considered to have been caused by errors in estimation of the mass distribution at the APM inlet. For example, the agreement of the experimental and calculated spectra in Figure 2.6 may have occurred unexpectedly due to underestimation of the width of the PSL's size distribution before DMA classification. Another possibility is that the experimental spectra were broader than the theoretical ones because the actual NaCl particles had a distribution of density, while the density was assumed constant in the theoretical calculation. Both of these errors may occur even if the DMA classification was perfectly ideal.

Ratios of the height and the FWHM of the experimental APM spectra to those of the predicted APM spectra are plotted in Figure 2.11 in the same manner as in Figure 2.8. For sizes of 50 nm and larger, the height ratio stayed almost constant in the range of approximately 0.7 to 0.8, whereas the FWHM ratio fell within the range of approximately 1.3 to 1.5. In contrast, for sizes of 30 nm and smaller, the APM spectra reduced the height and increased the width as the size decreased.

The inertial losses before and after the classification space due to high rotation speeds [3], which were discussed in Section 2.4.1, did not seem significant and were not the main reason for the reduction of the height. This is based on the observation that the heights were about the same in Figure 2.11 at each size between the two λ settings (i.e., the measurements were carried out at different rotation speeds). In Figure 2.8 for data with the PSL particles, on the other hand, slightly lower heights were observed at sizes below 100 nm for $\lambda = 0.49$ (i.e., higher rotation speeds compared to $\lambda = 0.22$). However, since the reduced heights were accompanied with broadened widths, the reduced heights do not necessarily indicate losses. Therefore a significant difference in inertial losses does not seem to exist between the two λ settings.

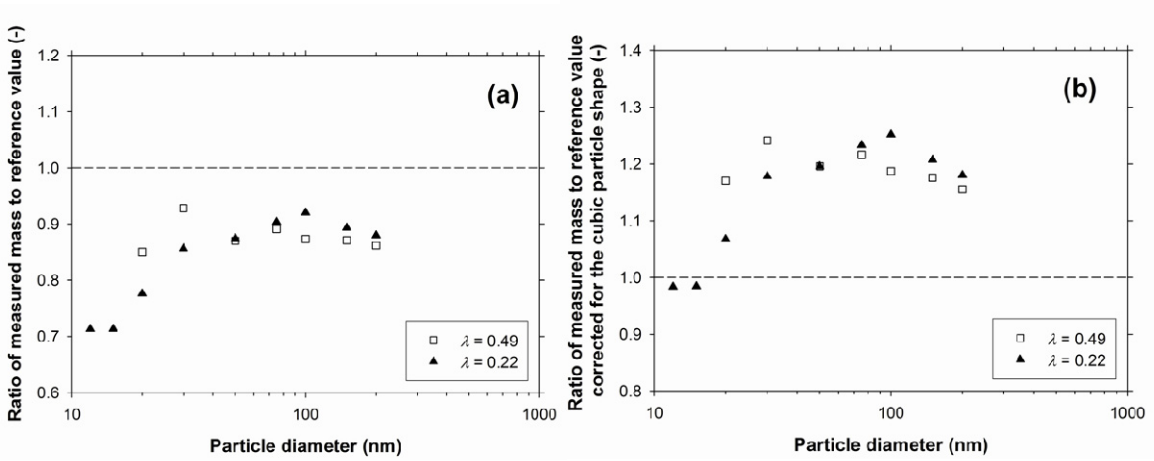

Figure 2.10 Ratio of the number-averaged mass experimentally obtained by the APM to the reference mass values for sodium chloride particles, assuming that (a) the particles were spheres of the diameter of the DMA-classified size and of the density of sodium chloride (2.17 g/cm^3), and (b) the particles were cubes of the density of sodium chloride.

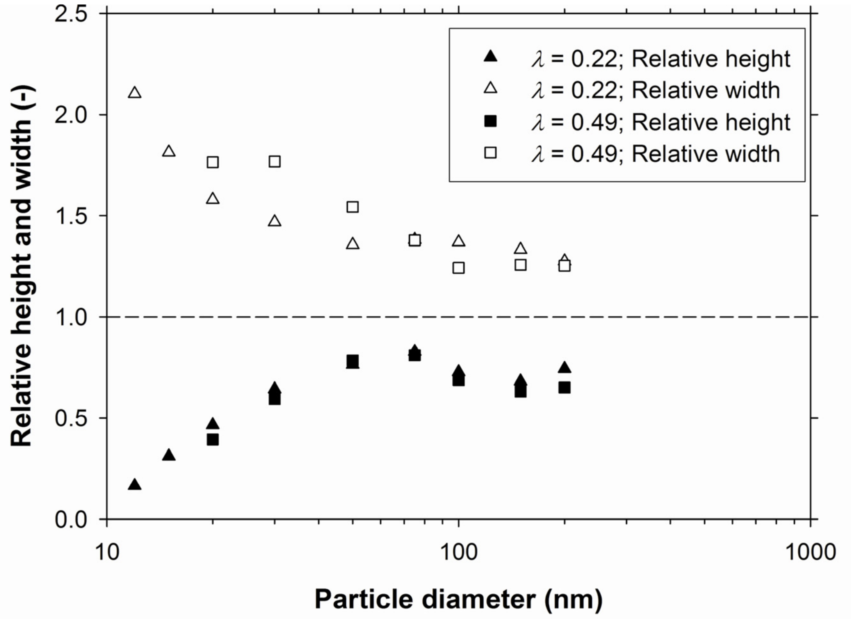

Figure 2.11 Ratio of the height and the FWHM of the APM spectra obtained experimentally to those obtained by calculation assuming a size distribution, density, and the theoretical APM transfer function, in the case of sodium chloride particles.

Figure 2.12 shows the experimental results for evaluation of particle losses in the APM. In the experimental setup shown in Figure 2.5, DMA-classified charged particles were passed through the APM at a flow rate of 1 L/min while the APM was under a still condition without rotation and with the voltage set at zero. The ratio of the particle concentration at the APM outlet to that at the APM inlet, which is an indicator for the penetration efficiency through the APM, is plotted in Figure 2.12. The ratio decreased as particle size decreased, from ~ 100 % for 100 nm and larger particles, to ~ 10 % for 10 nm particles, the size dependence of which implies that the losses are due to Brownian diffusion of particles. The ratio for 12 nm particles was approximately 20 %, which is close to the height ratio of 15 % at 12 nm in Figure 2.11. This implies that the reduction of the height of the experimental spectrum with respect to the height of the predicted spectrum was mainly due to losses of particles in the APM by Brownian diffusion.

The purpose of the experiment with NaCl particles was to evaluate the APM classification characteristics at particle sizes of less than 30 nm, which was not possible with PSL particles I had. Classification of particles of 30 nm or smaller by the APM revealed the issues of underestimation of the mass and degradation of the resolution and penetration, which makes it difficult to use the APM for absolute determination of a mass or mass distributions, and suggests to develop a procedure of relative measurements in which the mass by the APM is corrected with reference mass values of some standard particles. On the other hand, classification of particles of less than 30 nm by the APM may still be useful in applications which do not require absolute accuracy of mass, for example a measurement of change in particle mass or a semi-quantitative comparison of masses of different particles, in which only the first criterion in Section 2.5.1 must be satisfied.

2.6 Conclusions

I inquired into the conditions that ensure good particle classification performance over a wide mass range for the APM that was considered in this study. I

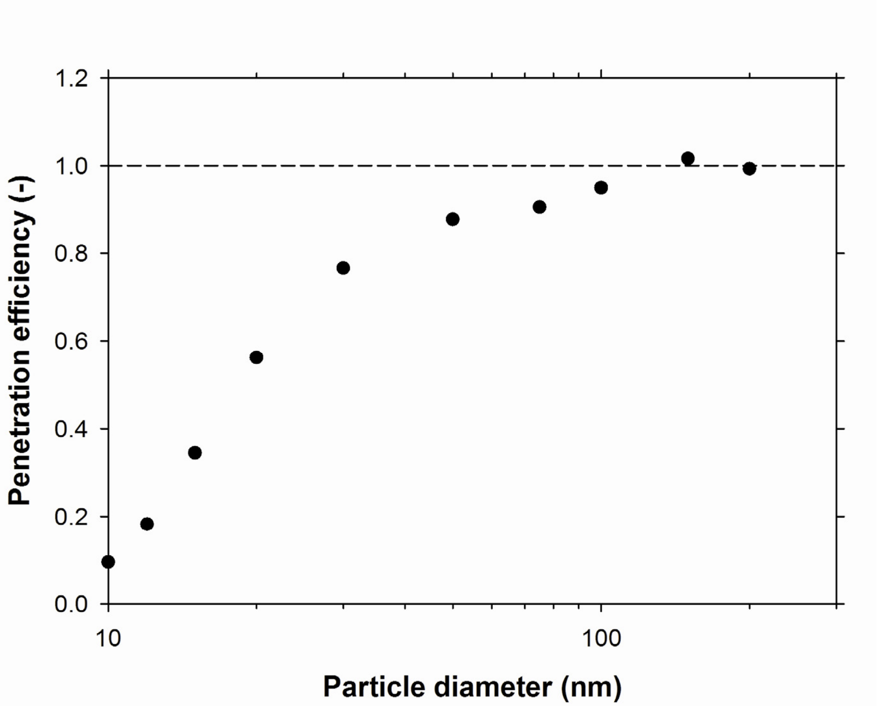

Figure 2.12 Penetration efficiency, i.e., the ratio of the concentration at the APM outlet to that at the inlet, for particles that flew through the APM at 1 L/min when the APM is not rotating.

also carried out experiments to verify the validity of the theoretical considerations. In the investigation of the classifiable mass range, a boundary condition was determined from the design specification and the λ value of the APM. For balancing even better resolution and penetration, it was found that the λ value should be maintained within the range between 0.25 and 0.5. The mass range that the APM was able to cover while maintaining the λ value between 0.25 and 0.5 was from 0.003 to 2000 fg, which corresponded to the diameter range from 20 to 1600 nm if the density of particles is 1 g/cm^3.

In the experimental verification of the APM classification performance with PSL particles (density of about 1 g/cm^3), I compared mass values determined by measurement with the APM with mass values by the EAB method or by estimation with size and density, and found that the values agreed with each other within 5 % in the size range from 50 to 800 nm for both λ-value settings. For evaluation of the APM at smaller sizes, experiments were performed with sodium chloride particles (density of about 2 g/cm^3). It was found that the mass was accurately obtained in the size range between 30 and 200 nm, and that even at sizes as small as 12 nm the APM classification was possible. While the difference in shape between the theoretically predicted and experimentally obtained system response spectra implies that the actual transfer functions were somewhat wider and shorter than the theoretical ones, the difference was not very large at sizes of 50 nm and above. Therefore, the optimization of the classification performance by setting the λ value within a certain range was thought to be achieved successfully. On the other hand, however, systematic underestimation of mass was observed at sizes below 30 nm for PSL, and size below 20 nm for NaCl. In addition, for particles smaller than 50 or 100 nm, the APM system response spectra were considerably wider and shorter than theoretically predicted, suggesting effects of Brownian diffusion of particles in the APM.

2.7 References

[1] Ehara, K., Hagwood, C. and Coakley, K. J. Novel method to classify aerosol

particles according to their mass-to-charge ratio - Aerosol particle mass analyzer. *J. Aerosol Sci.* (1996) 27, 217.

[2] Olfert, J. S. and Collings, N. New method for particle mass classification - the Couette centrifugal particle mass analyzer. *J. Aerosol Sci.* (2005) 36, 1338.

[3] Olfert, J. S., Reavell, K. StJ., Rushton, M. G. and Collings, N. The experimental transfer function of the Couette centrifugal particle mass analyzer. *J. Aerosol Sci.* (2006) 37, 1840.

[4] Hagwood, C.,Coakley, K., Negiz, A. and Ehara, K. Stochastic modeling of a new spectrometer. *Aerosol Sci. Technol.* (1995) 23, 611.

[5] Knutson, E. O. and Whitby, K. T. Aerosol classification by electric mobility: Apparatus, theory, and applications. *J. Aerosol Sci.* (1975) 6, 443.

[6] Ehara, K., Takahata, K. and Koike, M. Absolute mass and size measurement of monodisperse particles using a modified Millikan's method: Part II - Application of electro-gravitational aerosol balance to polystyrene latex particles of 100 nm to 1 μm in average diameter. *Aerosol Sci. Technol.* (2006) 40, 521.

[7] Dahneke, B. E. Slip correction factors for nonspherical bodies - I Introduction and continuum flow. *J. Aerosol Sci.* (1973) 4, 139.

[8] Dahneke, B. E. Slip correction factors for nonspherical bodies - II Free molecular flow. *J. Aerosol Sci.* (1973) 4, 147.

[9] Dahneke, B. E. Slip correction factors for nonspherical bodies - III The form of the general law. *J. Aerosol Sci.* (1973) 4, 163.

[10] DeCarlo, P. F., Slowik, J. G., Worsnop, D. R., Davidovits, P. and Jimenez, J. L. Particle morphology and density characterization by combined mobility and aerodynamic diameter measurements. Part 1: Theory. *Aerosol Sci. Technol.* (2004) 38, 1185.

[11] Stolzenburg, M. R. An ultrafine aerosol size distribution measuring system, in *Department of Mechanical Engineering*, University of Minnesota, Minneapolis, MN. (1988)

Chapter 3

Design considerations and performance evaluation of a compact aerosol particle mass analyzer

3.1 Introduction

Chapter 2 described the appropriate mass range and desired operating conditions for the first commercial instrument, Model 3600 APM (Kanomax Japan Inc.), from the viewpoint of maximizing the mass classification performance. This model of APM is, however, significantly large in size, and hence it is not very suitable for field measurements. Therefore, an APM, which is significantly compact and more suitable for use in field measurements compared to the Model 3600 APM, has been developed.

In Section 3.2, starting with laying out a set of requirements for mass classification performance, I derive constraint formulae for the design parameters of the APM. I then determine a combination of the design parameters realizing an APM which is significantly smaller in size than and yet comparable in performance to the Model 3600 APM. In Section 3.3, I present experimentally evaluated performance of a prototype APM that was constructed according to the determined set of design parameters. The performance in terms of the accuracy and resolution in classifying particle mass and of the particle penetration through the APM is compared with that of the Model 3600 APM.

3.2 Theoretical considerations

3.2.1 Design and operation parameters

The APM operates by balancing the electrostatic and centrifugal forces acting on charged particles introduced in rotating cylindrical electrodes. In the theoretical analysis that follows, I assume for simplicity that particles carry a single elementary charge. Under the assumption of single charge, it may be considered that the APM classifies particles according to the mass.

The performance of mass classification by the APM is characterized by the transfer function, which is defined as the ratio of the number flux of particles with a specified mass m at the outlet of the APM to that at the inlet when the APM is operated at a constant voltage V and angular velocity ω of the electrodes. The APM transfer function derived theoretically under the assumption that the velocity profile of the aerosol flow through the electrode gap is either uniform or parabolic is shown in Figure 3.1. The center of the mass band of the transfer function m_c (to be more strict, the particle mass at which the centrifugal force acting on a particle at the radial distance r_c balances with the electrostatic force) is given by

$$m_c = \frac{e\,V}{r_c^2\,\omega^2\,\ln(r_2/r_1)}, \tag{3.1}$$

where e is the elementary charge, r_1 and r_2 are the inner and outer radius of the electrode gap, and $r_c = (r_1 + r_2) / 2$. In order for the classification resolution to be reasonably high, it is required that $\delta / r_c \ll 1$, where $\delta = (r_2 - r_1) / 2$ (see Equation 3.5 below). I assume in the following analyses that this condition is satisfied. Equation 3.1 is then approximated as

$$m_c \cong \frac{e\,V}{2\,r_c\,\delta\,\omega^2}. \tag{3.2}$$

The trajectories of particles having a mass m and a mechanical mobility B through the electrode gap, and hence the shape of the transfer function, are determined solely by the non-dimensional quantity termed the classification performance parameter

$$\lambda = \frac{2\,m\,B\,\omega^2\,L}{\bar{v}}, \tag{3.3}$$

where L is the axial length of the electrode gap, and $\bar{v}$ is the mean velocity of the aerosol flow through the electrode gap. The latter is given approximately by $\bar{v} = Q/(4\pi r_c \delta)$ with Q being the aerosol volumetric flow rate. It should be noted that λ depends on the particle properties m and B. I am interested only in particles whose mass is located within the mass band of the transfer function. When the width of this band is sufficiently smaller than m_c, which I assume in the following, I can replace m in Equation 3.3 with m_c. In addition, I replace the mobility B of particles whose mass is in this band with a constant value B_c. This approximation is valid either when the particle density is uniform and there is one-to-one correspondence between m and B, or when a DMA is installed upstream of the APM and the mobility is precisely specified. In the present study, I assume the former case; to be more specific, I assume that particles are spheres having the density of 1 g/cm^3. Under these assumptions, λ can be approximated by

$$\lambda_c = \frac{8\pi\, m_c\, B(m_c)\, \omega^2 r_c\, \delta\, L}{Q}, \tag{3.4}$$

where $B(m_c)$ denotes the mechanical mobility corresponding to m_c. Note that, unlike λ, the value of λ_c is determined uniquely once the operating conditions are specified, and that it does not depend on particle properties.

Because the uniform flow model for the aerosol velocity profile allows me an analytical expression for the theoretical transfer function, I adopt this model in the following analysis. Later in Section 3.2.5, I will confirm that the result obtained in this model is also valid for the parabolic flow model. Let the resolution, R, be defined as the ratio of m_c to the *full* base length of the transfer function band, Δm. As Figure 3.1 indicates, R is given by

$$R = \frac{r_c}{4\delta}\tanh(\lambda_c/2). \tag{3.5}$$

Let me define the particle penetration, T, as the maximum height of the transfer function, which is given by

$$T = \exp(-\lambda_c). \tag{3.6}$$

In general, I consider that the larger the values of R and T are, the better the APM performance is.

The parameters that determine m_c, R, and T can be categorized into the following two groups.

Operation parameters: ω and V

Design parameters: r_c, δ, L, and Q

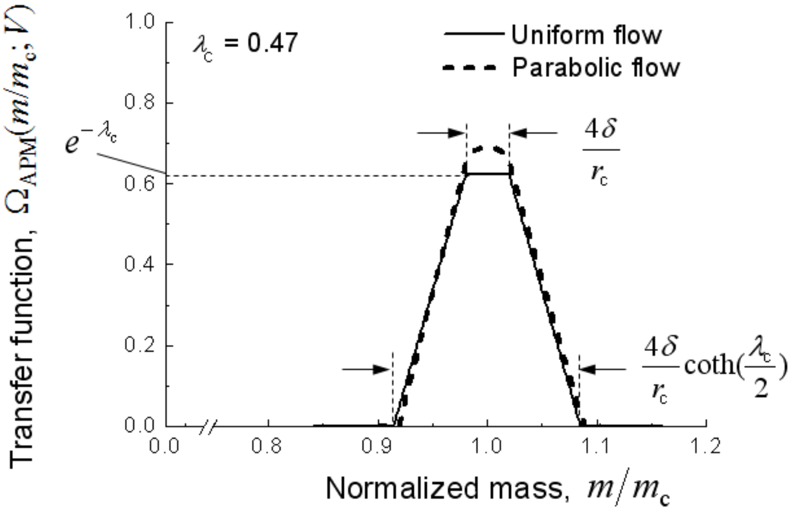

Figure 3.1 Theoretical APM transfer functions when the velocity profile of the aerosol flow is assumed uniform (solid line) and parabolic (dashed line). The transfer functions for λ_c = 0.47 are shown in this figure.

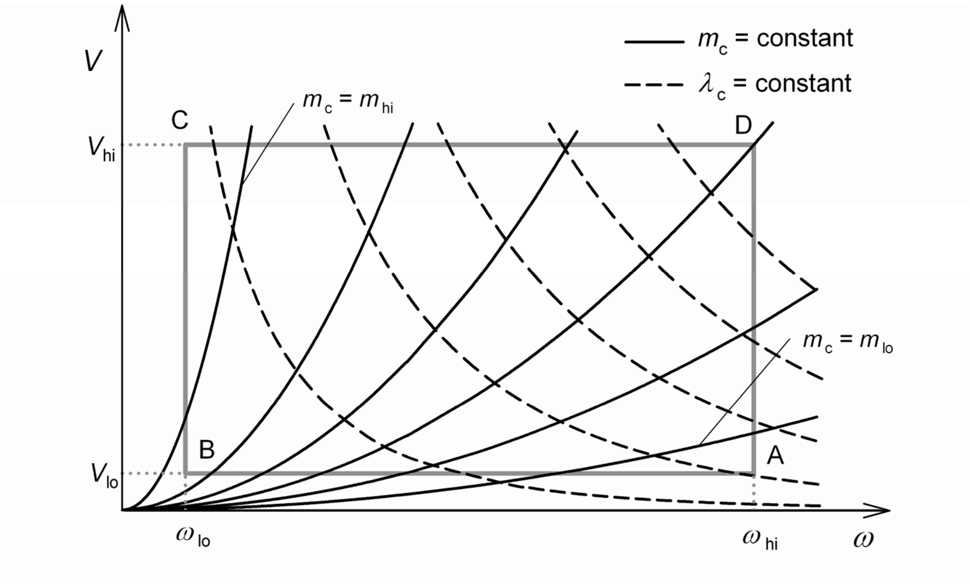

Figure 3.2 Typical contours of m_c (solid curves) and λ_c (dashed curves) in the (ω, V) plane. The rectangle ABCD indicates the operation region.

The parameters in the first group are those which can be selected at each operation from within certain limits; the limits are formally represented by

$$V_{\mathrm{lo}} \leq V \leq V_{\mathrm{hi}}\,, \tag{3.7}$$

$$\omega_{\mathrm{lo}} \leq \omega \leq \omega_{\mathrm{hi}}\,. \tag{3.8}$$

I chose the values of these limits as

$$(V_{\mathrm{lo}}, V_{\mathrm{hi}}) = (0.3\ \mathrm{V}, 2000\ \mathrm{V}), \tag{3.9}$$

$$(\omega_{\mathrm{lo}}, \omega_{\mathrm{hi}}) = (500\ \mathrm{rpm}, 14000\ \mathrm{rpm}). \tag{3.10}$$

The value of V_{hi} was chosen to avoid dielectric breakdown between the APM electrodes, and the value of V_{lo} was set roughly at ten times the resolution of a readily available digital-to-analog converter to be used for controlling the electrode voltage. The value of ω_{hi} was roughly the maximum capacity of a relatively compact motor typically used to rotate the electrodes. Finally, the value of ω_{lo} was determined from the requirement that the relative precision of the motor in controlling the rotational velocity of the electrodes be better than 3%, as the rotational velocity fluctuates unacceptably when the electrode is rotated even slower.

Determining the second group parameters is the target of the present study; their values are determined in the following analysis. The two parameters, L and Q, can be reduced to a single parameter $l = L/Q$, because L and Q appear only in the combined form L/Q in λ_{c}.

3.2.2 Performance requirements

I set forth the following formal requirements that need to be satisfied by a compact APM.

Requirement A: The variable range of m_{c} covers entirely a specified range (m_{lo}, m_{hi}).

Requirement B: For any m_{c} in (m_{lo}, m_{hi}), there exists an operating condition under which R is larger than or equal to a specified value R_{lo}.

Requirement C: For any m_{c} in (m_{lo}, m_{hi}), there exists an operating condition under which T is larger than or equal to a specified value T_{lo}.

Here, it is understood in Requirements B and C that there must be an operating condition such that these two requirements are *simultaneously* satisfied. The actual values of m_{lo}, m_{hi}, R_{lo}, and T_{lo} are chosen so that the performance of the compact APM is comparable to that of the Model 3600 APM; namely,

$$(m_{\mathrm{lo}}, m_{\mathrm{hi}}) = (0.001\ \mathrm{fg}, 1000\ \mathrm{fg}), \tag{3.11}$$

$$(R_{\mathrm{lo}}, T_{\mathrm{lo}}) = (0.5, 0.1). \tag{3.12}$$

The mass interval in Equation 3.11 corresponds approximately to the size interval of (12 nm, 1.2 μm) for spherical particles having the density of 1 g/cm^3.

Because the three requirements above do not result in a unique combination of design parameter values, it is desirable to introduce additionally a performance measure that can further narrow the range of the desired parameter values. Such a measure could be the product RT, or a product of certain powers of R and T. It would be, however, significantly complicated, though not impossible, to optimize such a quantity while satisfying the Requirements A to C, because these quantities depend not only on the design parameters but on the operation parameters. Based on Equations 3.5 and 3.6, if there are multiple combinations of the design parameters that realize the same value of T, a smaller value of δ/r_c leads to a larger value of R. Hence δ/r_c is simply used as such an additional performance measure.

3.2.3 Constraints on design parameters

In this section, a theoretical framework is developed to derive possible combinations of the design parameters that satisfy the above three requirements. First it is noted that, for fixed design parameters, the values of m_c and λ_c are fully determined from ω and V. Figure 3.2 shows typical contours of m_c and of λ_c in the (ω, V) plane. The rectangle in Figure 3.2 shows the operation region specified by Inequalities 3.7 and (3.8). Any two parameters can be selected out of the four parameters, m_c, λ_c, ω, and V, as independent variables, and regard the remaining parameters as functions of the independent variables. Here I chose (m_c, λ_c) as independent variables. The operation region in the (m_c, λ_c) plane appears a distorted parallelogram as shown in Figure 3.3.

Let Min(m_c) and Max(m_c) denote the minimum and maximum values of m_c in the operation region. Requirement A can be written as

$$\mathrm{Min}(m_\mathrm{c}) \leq m_\mathrm{lo}, \tag{3.13}$$

$$\mathrm{Max}(m_\mathrm{c}) \geq m_\mathrm{hi}, \tag{3.14}$$

with the understanding that these two conditions must be simultaneously satisfied. As is obvious from Figure 3.3, Min(m_c) occurs at point A where $(\omega, V) = (\omega_\mathrm{hi}, V_\mathrm{lo})$; namely, Min($m_\mathrm{c}$) = m_c(A). Since $m_\mathrm{c}(\mathrm{A}) = eV_\mathrm{lo}/(2r_\mathrm{c}\delta\omega_\mathrm{hi}{}^2)$ from Equation 3.2, Inequality 3.13 is rewritten as

$$[\mathrm{RA1}] \quad r_\mathrm{c}\delta \geq \frac{eV_\mathrm{lo}}{2\omega_\mathrm{hi}{}^2 m_\mathrm{lo}} \quad . \tag{3.13'}$$

Similarly, since $\mathrm{Max}(m_\mathrm{c}) = m_\mathrm{c}(\mathrm{C}) = eV_\mathrm{hi}/(2r_\mathrm{c}\delta\omega_\mathrm{lo}{}^2)$, Inequality 3.14 is rewritten as

$$[\mathrm{RA2}] \quad r_\mathrm{c}\delta \leq \frac{eV_\mathrm{hi}}{2\omega_\mathrm{lo}{}^2 m_\mathrm{hi}}. \tag{3.14'}$$

The symbols [RA1] and [RA2] are to indicate that these are conditions derived from Requirement A.

In order for Requirements B and C to be satisfied, there must exist in the operation region some value of λ_c such that the inequalities

$$R(\lambda_\mathrm{c}) \geq R_\mathrm{lo}, \tag{3.15}$$

$$T(\lambda_\mathrm{c}) \geq T_\mathrm{lo} \tag{3.16}$$

simultaneously hold true for any m_c in (m_lo, m_hi). Here, the symbols $R(\lambda_\mathrm{c})$ and $T(\lambda_\mathrm{c})$ indicate explicitly that R and T are functions of λ_c, as expressed by Equations 3.5 and 3.6. Since $R(\lambda_\mathrm{c})$ and $T(\lambda_\mathrm{c})$ are monotonically increasing and decreasing functions of λ_c, respectively, Inequalities 3.15 and 3.16 can be replaced with

$$\lambda_\mathrm{c} \geq \lambda_\mathrm{lo}, \tag{3.15'}$$

$$\lambda_\mathrm{c} \leq \lambda_\mathrm{hi}, \tag{3.16'}$$

where

$$(\lambda_\mathrm{lo}, \lambda_\mathrm{hi}) = (2\,\mathrm{atanh}(4\delta R_\mathrm{lo}/r_\mathrm{c}),\ \ln(1/T_\mathrm{lo})). \tag{3.17}$$

As seen in Figure 3.3, for a given m_c, λ_c spans across a range from Min(λ_c |m_c) to Max(λ_c |m_c) under the constraints of Inequalities 3.7 and 3.8, such as from points F to E in the figure. Here Max(|m_c) and Min(|m_c) indicate, respectively, the conditional maximum and minimum for a given m_c. For a given m_c, if the inequality

$$\mathrm{Max}(\lambda_c \mid m_c) \geq \lambda_{lo}, \tag{3.15''}$$

is met, then there exists λ_c that satisfies Inequality 3.15'. Similarly, if

$$\mathrm{Min}(\lambda_c \mid m_c) \leq \lambda_{hi}, \tag{3.16''}$$

is met, then there exists λ_c that satisfies Inequality 3.16'. If

$$\lambda_{lo} \leq \lambda_{hi}, \tag{3.18}$$

holds true in addition to Inequalities 3.15" and 3.16", there exists an operating condition such that Inequalities 3.15' and 3.16' are *simultaneously* satisfied. In other words, the three inequalities, 3.15", 3.16" and 3.18, are necessary and sufficient conditions for Requirements B and C to be satisfied simultaneously.

Now the conditions 3.15" and 3.16" are rewriten into inequalities in terms of the design parameters. For Inequality 3.15", as Figure 3.3 shows, if Inequality 3.15" holds both at $m_c = m_{hi}$ and at $m_c = m_{lo}$, it automatically holds at any m_c within (m_{lo}, m_{hi}). Hence Inequality 3.15" is expressed by

$$\mathrm{Max}(\lambda_c \mid m_{lo}) \geq \lambda_{lo}, \tag{3.15''-1}$$

$$\mathrm{Max}(\lambda_c \mid m_{hi}) \geq \lambda_{lo}. \tag{3.15''-2}$$

Since $\mathrm{Max}(\lambda_c \mid m_{lo})$ occurs at point E in Figure 3.3, it can be expressed by $\mathrm{Max}(\lambda_c \mid m_{lo}) = \lambda_c(\mathrm{E}) = 8\pi m_{lo} B(m_{lo}) \omega_{hi}^2 r_c \delta l$, while λ_{lo} can be approximated as $\lambda_{lo} \cong 8R_{lo}\delta / r_c$ from the assumption $\delta / r_c << 1$. Hence Inequality 3.15"-1 is rewritten as

$$[\mathrm{RB1}] \quad r_c^{\,2}\, l \geq R_{lo}/(\pi m_{lo} B(m_{lo}) \omega_{hi}^2)\ . \tag{3.15'''-1}$$

Similarly, noting that $\mathrm{Max}(\lambda_c \mid m_{hi}) = \lambda_c(\mathrm{H}) = 4\pi e V_{hi} B(m_{hi}) l$, Inequality 3.15"-2 can be rewriten as

$$[\mathrm{RB2}] \quad r_c\, l / \delta \geq 2R_{lo}/(\pi e V_{hi} B(m_{hi}))\ . \tag{3.15'''-2}$$

The symbols [RB1] and [RB2] indicate that these are conditions derived from Requirement B. In the same manner, Inequality 3.16" can be rewritten into

$$[\mathrm{RC1}] \quad l \leq \ln(1/T_{lo})/(4\pi e V_{lo} B(m_{lo})), \tag{3.16'''-1}$$

$$[\mathrm{RC2}] \quad r_c \delta l \leq \ln(1/T_{lo})/(8\pi m_{hi} B(m_{hi}) \omega_{lo}^2). \tag{3.16'''-2}$$

Finally, Inequality 3.18 can be rewritten from Equation 3.17 as

$$[\mathrm{RBC}] \quad \delta / r_c \leq \tanh(\ln(1/\sqrt{T_{lo}}))/(4R_{lo})\ . \tag{3.18'}$$

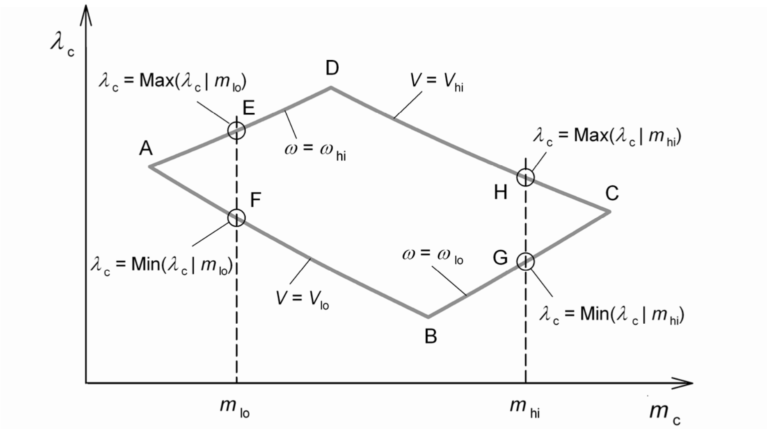

Figure 3.3 Schematic illustration of the operation region in the (m_c, λ_c) plane with both axes represented in logarithmic scale. The distorted parallelogram ABCD corresponds to the rectangle ABCD in Figure 3.2.

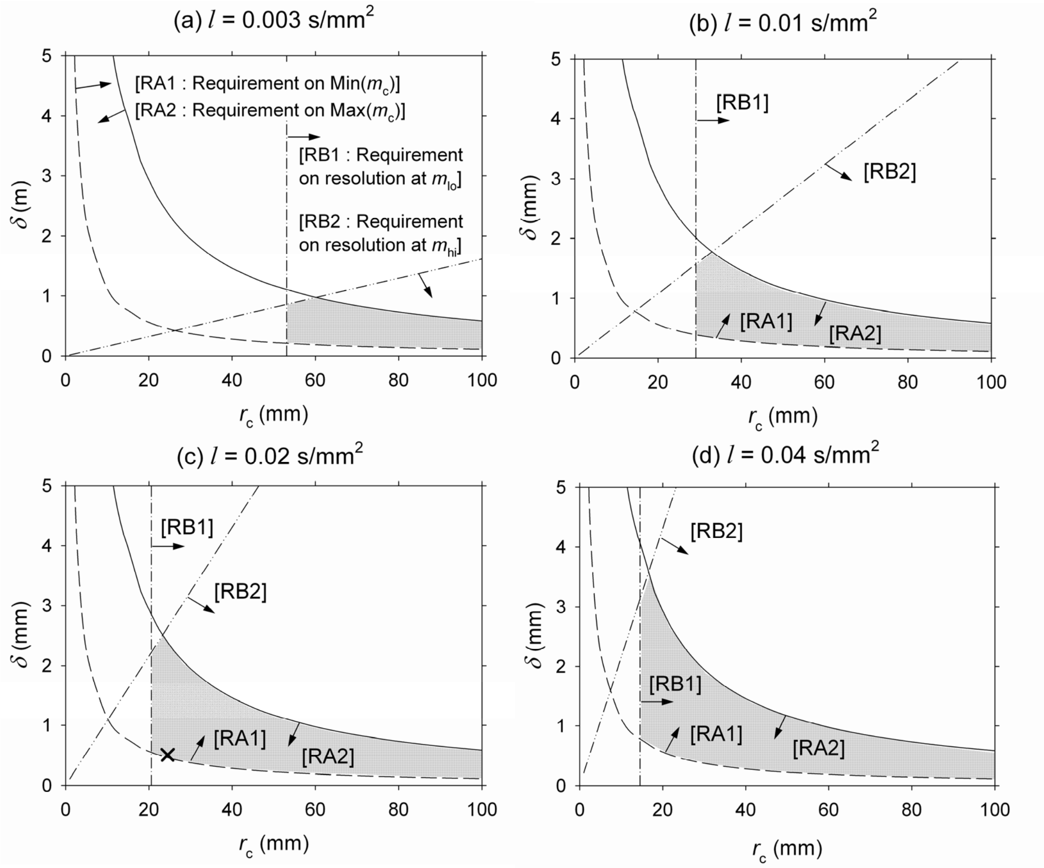

Figure 3.4 Regions in the (r_c, δ) plane satisfying the four conditions for (a) l = 0.003 s/mm^2, (b) 0.01 s/mm^2, (c) 0.02 s/mm^2, and (d) 0.04 s/mm^2. The hatched areas indicate the regions in which all the four conditions are satisfied. The cross mark in panel (c) represents the combination of the design parameters finally selected.

The symbol [RBC] indicates that this condition is related to the simultaneousness of Requirements B and C.

In summary, the design parameters must satisfy [RA1], [RA2], [RB1], [RB2], [RC1], [RC2], and [RBC], in order for Requirements A, B, and C to be fulfilled.

3.2.4 Optimum design

Substituting the limit values given in Equations 3.9 to 3.12 into the conditions [RA1] to [RBC], these are

[RA1] $r_c\delta \geq 11.18\ \mathrm{mm}^2$,
[RA2] $r_c\delta \leq 58.44\ \mathrm{mm}^2$,
[RB1] $r_c^{\ 2}\, l \geq 8.390\ \mathrm{s}$,
[RB2] $r_c\, l\,/\delta \geq 0.1894\ \mathrm{s/mm}^2$,
[RC1] $l \leq 0.4320\ \mathrm{s/mm}^2$,
[RC2] $r_c\delta l \leq 6.371\ \mathrm{s}$,
[RBC] $\delta/r_c \leq 0.4091$.

The condition [RBC] need not be considered, because it is automatically satisfied under the assumption $\delta/r_c << 1$. I additionally assume here that practically appropriate values of L and Q are, respectively, in the ranges of 40 - 200 mm and of 0.3 - 1.0 L/min. The corresponding range of l is then 0.003 - 0.040 s/mm^2. The condition [RC1] is automatically satisfied, if l is in this range. In addition, the condition [RC2] is automatically satisfied, if [RA2] is satisfied and l is in this range. From these arguments, the conditions I have to consider are now reduced to [RA1], [RA2], [RB1], and [RB2]. It may be worth pointing out here that the conditions [RA1] and [RA2] were derived from the requirement on m_c, while the conditions [RB1] and [RB2] were from the requirement on R.

The regions in the (r_c, δ) plane that satisfy the conditions [RA1] to [RB2] for fixed values of l are shown in Figures 3.4a to 3.4d. As l increases, the lower boundary of r_c decreases. If Q = 0.3 L/min is adopted which is an aerosol flow rate often employed for relatively small flow rate CPCs and optical particle counters, and if L = 100 mm is chosen as a reasonably short electrode length, l = 0.02 s/mm^2 can be obtained. Considering that a small r_c is desirable in realizing a compact APM, and that a small value of the performance measure, δ/r_c, is desirable, I chose the final combination of the design parameter values as l = 0.02 s/mm^2 (L = 100 mm, Q = 0.3 L/min), r_c = 24.5 mm, and δ= 0.5 mm. With this value of δ, the maximum electric field strength that may occur in the electrode gap, $V_\mathrm{hi}/(2\delta)$, is 2×10^6 V/m, which is smaller than the commonly accepted threshold value of the dielectric breakdown of air, 3×10^6 V/m (CRC Handbook of Chemistry and Physics, 2008). The chosen combination of the design parameter values is marked by a cross in Figure 3.4c. In this choice, the value of the performance measure, δ/r_c, is 0.0204, which is comparable to the value, 0.0196, for the value for the Model 3600 APM. Note that this value of δ/r_c is consistent with $\delta/r_\mathrm{c} \ll 1$ assumed in the above analysis.

It is noted from Figure 3.4c that the conditions [RA2] and [RB2] are satisfied by wide margins. Taking advantage of this fact, the value of ω_lo is reselected at 1000 rpm, instead of 500 rpm as initially assumed. The operation region of the APM with this value of ω_lo is shown in Figure 3.5. A summary of comparison between the APM thus designed and the Model 3600 APM is given in Table 3.1.

3.2.5 Validity in the parabolic flow model

The preceding analysis is based on the uniform flow model for the velocity distribution of the aerosol flow in the electrode gap. A more realistic model of the flow profile is the parabolic flow model. In this section, I examine whether the design parameters chosen above satisfy Requirements A to C in the parabolic flow model.

First it is noted that the expressions of m_c and λ_c (Equations 3.2 and 3.4), and hence the location of the operation region in the (m_c, λ_c) plane are model independent. Consequently, Requirement A is satisfied irrespective of the flow model. On the other hand, $R(\lambda_\mathrm{c})$ and $T(\lambda_\mathrm{c})$, and hence the values of λ_lo and λ_hi, depend on the flow model. Equation 3.17 gives λ_lo and λ_hi in the uniform flow model, and with the chosen values of the design parameters, these are

Table 3.1 Comparison between the compact APM developed in the present study and the Model 3600 APM.

		Compact APM	Original APM MODEL 3600
Electrode Dimensions			
Radius, r_c	(mm)	24.5	51
Gap, 2δ	(mm)	1	2
Length, L	(mm)	100	250
Rotational velocity	(rpm)	1000 – 14000	50 - 9500
Electrode voltage	(V)	0.3 – 2000	0.3 - 2000
Aerosol flow rate (recommended value)	(L/min)	0.3	0.3 – 1.5
Particle mass range [a]	(fg)	$9.1\times10^{-4} - 1.2\times10^{3}$	$4.8\times10^{-4} - 5.9\times10^{4}$ [c]
Particle size range [b]	(nm)	12 - 1300	9.7 - 4800

[a] Theoretical range satisfying R (resolution) > 0.5 and T (penetration) > 0.1, simultaneously.

[b] Derived from the mass range assuming that the density is 1 g/cm^3.

[c] Range calculated for the aerosol flow rate of 1.0 L/min.

$(\lambda_{\mathrm{lo}}, \lambda_{\mathrm{hi}}) = (0.0817, 2.30)$. [uniform flow]

In the parabolic flow model, $R(\lambda_c)$ and $T(\lambda_c)$ need to be calculated numerically. By performing this calculation, these are

$(\lambda_{\mathrm{lo}}, \lambda_{\mathrm{hi}}) = (0.0791, 3.31)$. [parabolic flow]

Because the interval $(\lambda_{\mathrm{lo}}, \lambda_{\mathrm{hi}})$ of the parabolic flow model encompasses that of the uniform flow model, it is obvious that Inequalities 3.15", 3.16", and 3.18, and hence Requirements B and C, are satisfied also in the parabolic flow model.

3.3 Experimental verification

3.3.1 Method

To confirm the validity of the preceding theoretical treatment, an APM having the values of the design parameters thus determined was constructed, and its performance was experimentally evaluated and compared to that of the Model 3600 APM. Similar to Chapter 2, I compare experimental APM system response spectra obtained for particles with a known mass to the corresponding theoretically predicted spectra. The experiment was carried out in either of the two configurations illustrated in Figures 3.6a and 3.6b. In configuration (a), the particle concentration at the APM inlet was measured before and after data collection of the particle concentration at the APM outlet C_N by switching a three-way valve connected to the inlet of a CPC. In configuration (b), two CPCs were used to measure the concentrations at the inlet and outlet of the APM simultaneously. In either configuration, the electrode voltage was swept linearly with time.

I proposed a scheme to select an appropriate value of λ_c for APM operations, which may be termed the "resolution matching scheme" in Section 2.4.2. This scheme assumes the use of a DMA in combination with the APM, and the value of λ_c is so selected that the resolution of the APM expressed in terms of particle mobility matches the resolution of the DMA. In the present study, the ratio of the aerosol to sheath air flow rates of the DMA was set at 0.1, and the corresponding λ_c for the compact APM

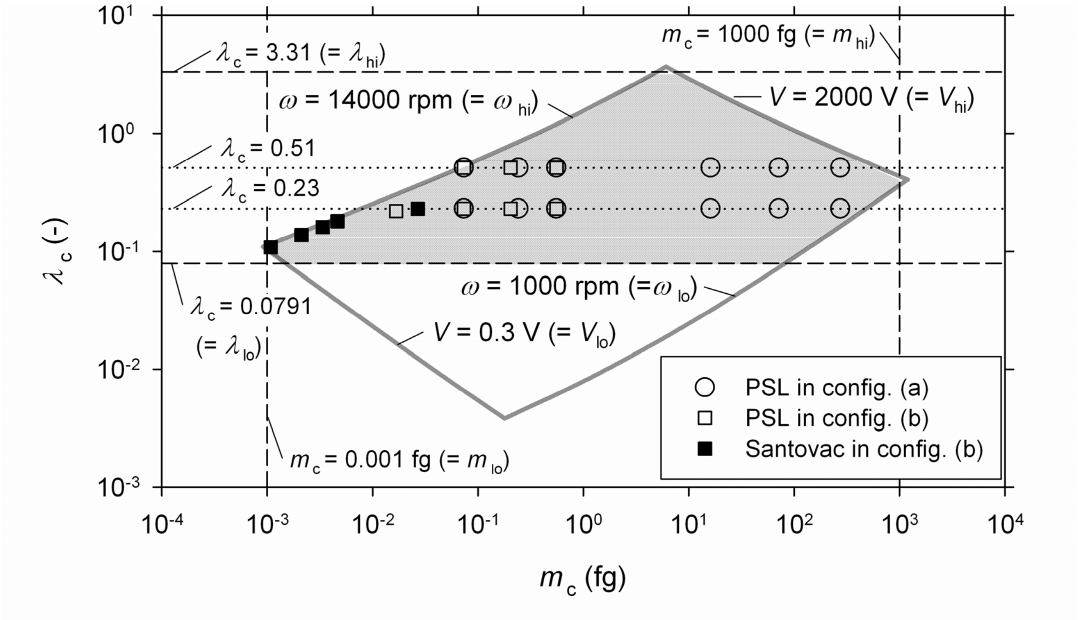

Figure 3.5 Operation region of the compact APM constructed in the present study (distorted parallelogram). The hatched area indicates the region in which Requirements A, B, and C are all satisfied. The symbols ○, □, and ■ represent the points on which APM spectra were experimentally obtained, where ○ represents an experiment conducted in configuration (a) with PSL particles used as test particles; □ in configuration (b) with PSL particles; and ■ in configuration (b) with Santovac oil particles. See Figure 6 for configurations (a) and (b).

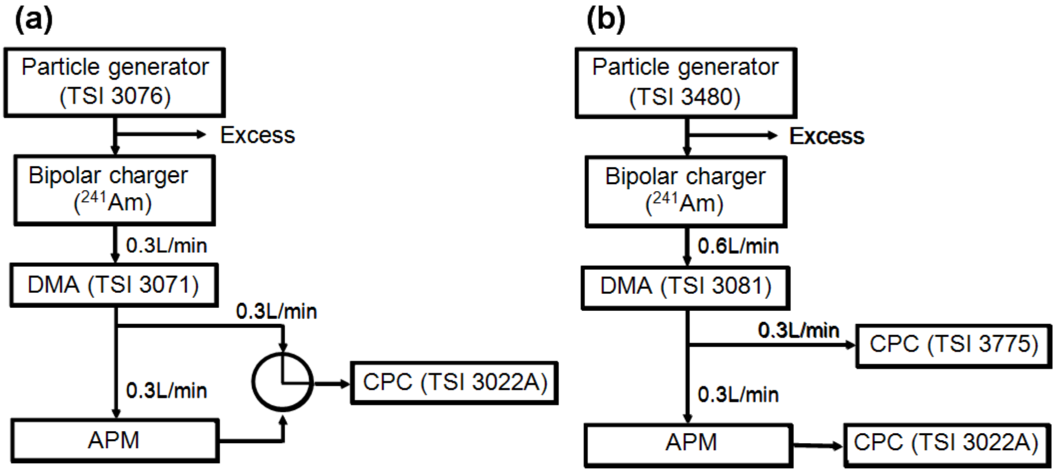

Figure 3.6 Two experimental configurations.

calculated according to the resolution matching scheme ranged from 0.25 to 0.5 depending on the particle size. The experiments were carried out at $\lambda_c = 0.23$ and $\lambda_c = 0.51$, the values roughly equal to the limits of this range, as long as they were inside the operation region (see Figure 3.5).

Polystyrene latex (PSL) particles of eight sizes; 29, 48, 70, 76, 100, 309, 506, and 791 nm (STADEX; JSR Co.), and Santovac oil particles were aerosolized to be used for test particles. When PSL particles were used, the DMA voltage was adjusted so that the highest particle concentration was attained at the DMA outlet. The density of each PSL particle type is given by the manufacturer, and is in the range from 1.054 to 1.115 g/cm^3. Santovac oil particles were aerosolized by an electrospray aerosol generator (Model 3480, TSI Inc.), and were selected by the DMA at five different sizes ranging from 12 to 35 nm. I assume that the density of the Santovac particles is identical to that of a bulk liquid, 1.198 g/cm^3. The mass of the test particles ranges from 0.0011 fg to 274 fg, which covers a major part of the interval specified by Equation 3.11.

The symbols in Figure 3.5 (○, □, and ■) indicate the points on which APM spectra were collected in the experiment. Since the line $\lambda_c = 0.23$ for m_c smaller than about 10^{-2} fg is outside the operation region, the operation conditions for particles with such small m_c were chosen so that ω took its maximum possible value, ω_{hi} (= 14000 rpm).

Prior to the experiment, continuous operations at 14000 rpm longer than 10 h were conducted several times, and it was confirmed that the constructed APM worked stably at this maximum rotational speed. Also, it was confirmed that at the maximum voltage (2000 V), the electrostatic breakdown did not occur during the operations.

3.3.2 Results

The APM spectra obtained experimentally are shown in Figures 3.7a (PSL particles with $\lambda_c = 0.51$), 3.7b (PSL particles with $\lambda_c = 0.23$), and 3.7c (Santovac oil particles). Theoretically, an APM spectrum can be calculated according to

$$C_N(V) = \int n(m) \cdot \Omega_{APM}(m; V)\mathrm{d}m, \qquad (3.19)$$

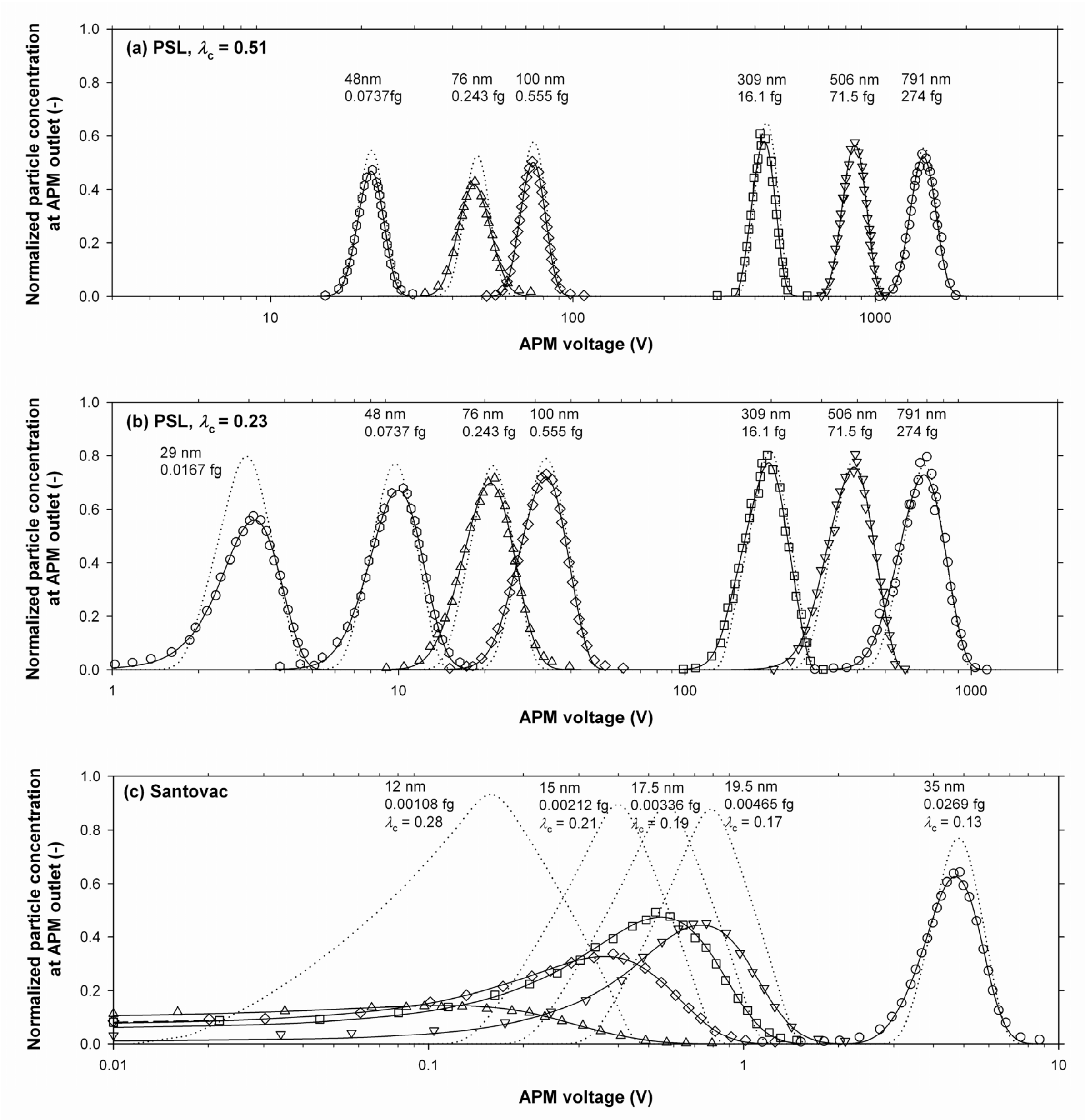

Figure 3.7 APM spectra for (a) PSL particles with λ_c = 0.51, (b) PSL particles with λ_c = 0.23, and (c) Santovac oil particles. Experimental spectra are shown with symbols, calculated spectra obtained by the least square fitting method shown with solid curves, and theoretically predicted spectra shown with dotted curves. Associated with each experimental spectrum is the values of the DMA-classified diameter and of the number-averaged mass. For spectra of Santovac oil particles, the values of λ_c are also shown.

where $n(m) = \mathrm{d}C_\mathrm{N}/\mathrm{d}m$ is the mass distribution of particles at the APM inlet, and $\Omega_\mathrm{APM}(m; V)$ is a function of m with V as a parameter, representing the APM transfer function for singly-charged particles when the classification voltage is V. Here the effects of particle Brownian motion on the transfer function is neglected [1], and an asymmetric normal distribution for $n(m)$ is adopted. For more details of the procedure of determining $n(m)$, see Section 2.5.2.1. The solid curves in Figure 3.7 represent $C_\mathrm{N}(V)$ after the least square fitting was performed by the FIT_APM. Almost exact agreement between $C_\mathrm{N}(V)$ and the experimental spectra observed in Figure 3.7 suggests the appropriateness of adopting the asymmetric normal distribution as $n(m)$.

The number-averaged mass can be calculated from $n(m)$ thus determined. Figure 3.8 shows the ratio of the number-averaged mass obtained in this way to that predicted theoretically. The latter was derived from the volume of a sphere having the DMA-classified diameter multiplied by the known particle density. Because no noticeable systematic differences in the experimental results were observed between the two experimental configurations depicted in Figures 3.6a and 3.6b, as well as between the two choices of λ_c, the data in Figure 3.8 were plotted without discrimination between these experimental conditions. For the purpose of comparison, Figure 3.8 also shows the data obtained in our previous study using the Model 3600 APM operated at the aerosol flow rate of 1 L/min for PSL and NaCl particles (see Section 2.5.2).

Figure 3.8 shows that the experimentally determined mass is in good agreement with the theoretically predicted mass for particles larger than 50 nm (approximately 0.1 fg in mass); the ratio between them is within the interval of 1 ± 0.1, with a slightly larger scatter among data for the prototype compact APM than for the Model 3600 APM. However, for particles smaller than 30 nm (approximately 0.02 fg in mass), a systematic deviation of the ratio from unity is observed, with the measured mass smaller than the predicted mass. This phenomenon is similarly observed for the Model 3600 APM, although quantitative comparison is not possible because different types of particles, especially in terms of their shape, were used in the present and previous studies. It is noted that the disagreement between theory and experiment in the relatively smaller mass range is observed regardless of the operating conditions as represented by λ_c, as well as regardless of the APM design.

Particle Brownian motion within the APM is expected to shift the APM transfer function to the larger mass side [1], and hence it cannot explain the observed disagreement. In my separate study [2], we investigated size change of Stantovac and poly-alpha-olefin (PAO) particles before and after the APM by using a scanning mobility particle sizer, but observed no size change even at 10 nm. Therefore, evaporation of the oil particles is not considered to be the major cause of the disagreement. Although no definitive explanation is obtained yet, the observed disagreement might be ascribable to non-sphericity of the test particles in the relatively small size range, which can lead to an increase in mobility equivalent diameter as compared to the diameter of spherical particles having the same mass. It is recently reported on the basis of observation with a scanning electron microscope that the sphericity of the 30 nm PSL particles is not as good as the 50 nm and larger PSL particles [3]. Also, oil droplets moving through the sheath air of a DMA could be distorted depending on their sizes, although I am unable at present to quantitatively estimate this effect.

Besides the locations of the APM spectra, their shapes, especially the widths of the spectra, are of my concern, because they reflect the actual resolution of the instrument. If a reasonable estimate of the shape of $n(m)$ is available, I can calculate a theoretical spectrum according to Equation 3.19 and compare it with experiment. Because the difference in number-averaged mass between the theoretical prediction and the experimental observation is significant for particles smaller than 30 nm, as I have just seen above, I temporarily use here an effective density such that the predicted number-averaged mass reproduces the observed number-averaged mass. In addition, I assume that the shape of $n(m)$ is derived from the DMA transfer function multiplied by the size distribution at the DMA inlet; the latter for the PSL particles is approximated by a normal distribution having the size standard deviation provided by the particle manufacturer, or for Santovac particles approximated by a uniform distribution (see

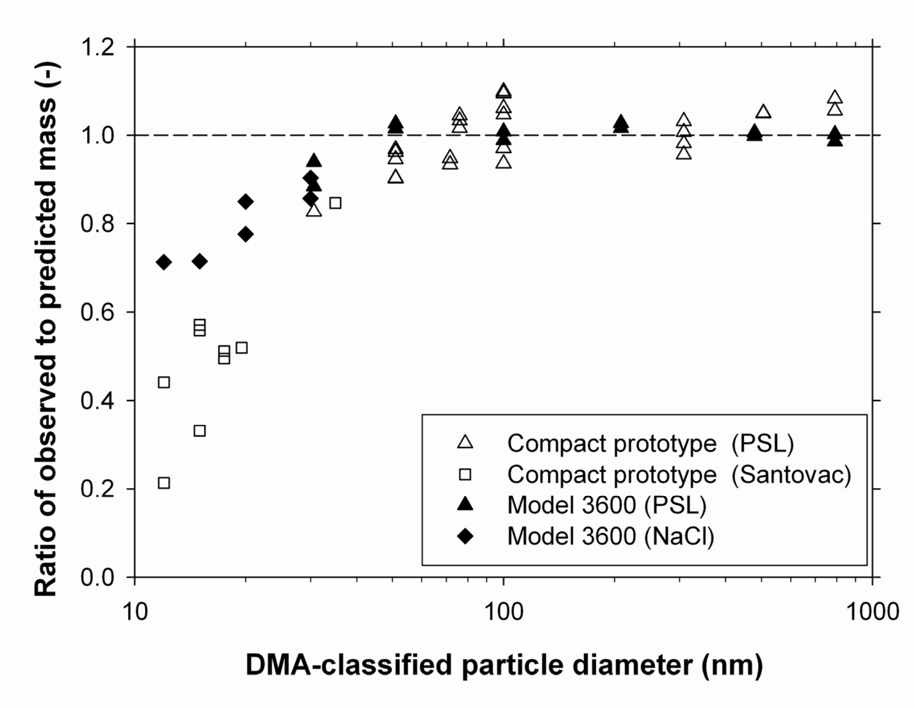

Figure 3.8 Ratio of the number-averaged mass obtained experimentally to that predicted theoretically. The theoretically predicted mass values were based on the assumption that particles, including NaCl particles in the experiment with the Model 3600 APM, are spherical.

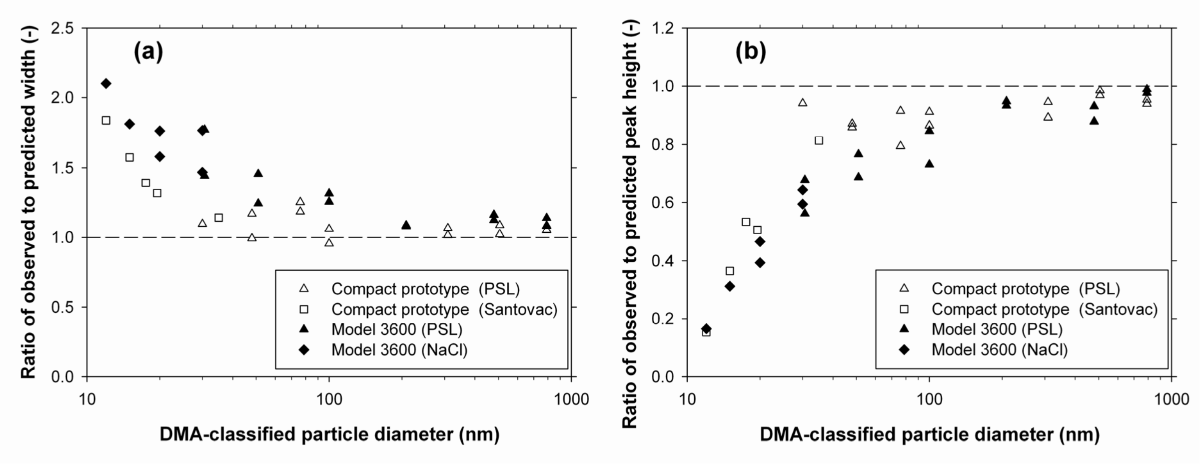

Figure 3.9. Ratios of (a) the full width at half maximum and (b) the peak height of the experimental spectra to those of the theoretically predicted spectra.

Section 2.5.2). The theoretical spectra thus obtained are shown by the dotted lines in Figure 3.7.

Figure 3.7 shows that the shapes of the experimental spectra for particles larger than 100 nm are in excellent agreement, both in their widths and heights, with those of the theoretical spectra. The agreement is still good for particles as small as about 50 nm, but for even smaller particles, especially particles smaller than 20 nm, notable broadening is observed in the experimental spectra. Again, the reason for this broadening is not identified at this moment. It should be pointed out that the apparently sharp spectrum for 48 nm PSL particles in Figure 3.7a was obtained at the rotational velocity almost equal to the maximum velocity ω_{hi} (see also Figure 3.5 for the operation conditions). This indicates that an instability of the aerosol flow through the APM does not occur even at ω_{hi}, and is not the reason for the broadening observed below 20 nm.

The ratios of the full width at half maximum and the peak height of the experimental spectra to those of the theoretically predicted spectra, plotted in Figure 3.9a and 3.9b respectively, confirm that for particles larger than 50 nm the spectral broadening is not significant. Figures 3.9a and 3.9b also show that both the widths and heights of the spectra obtained with the compact APM are in slightly better agreement with the theoretical predictions than those with the Model 3600 APM.

The analyses here demonstrate that the constructed APM operated at the aerosol flow rate of 0.3 L/min has a performance comparable to that of the Model 3600 APM operated at 1.0 L/min.

3.4 Conclusions

A theoretical framework was formulated that determines the design parameters of an APM which is significantly smaller than the existing Model 3600 APM and yet satisfies several performance criteria. A prototype compact APM having the design parameters determined according to this formulation was constructed, and its performance was experimentally evaluated.

The number-averaged mass of particles larger than 50 nm (approximately 0.1 fg in mass) determined experimentally was in good agreement with theoretically predicted values. The scatter of the experimentally obtained number-averaged mass around the theoretical prediction was slightly larger than that obtained with the Model 3600 APM. For particles smaller than 30 nm (approximately 0.02 fg), a systematic and significant underestimate of the number-averaged mass as compared with theoretical prediction was observed. This phenomenon was observed also for the Model 3600 APM, and regardless of the operating conditions. Although the exact reason for this phenomenon is not identified yet, a possible role of the non-sphericity of the test particles in the observed phenomenon is suggested.

The shape of the observed spectra was in excellent agreement with theoretical prediction, both in terms of their widths and heights, for particles larger than 100 nm, and in fairly good agreement for particles larger than 50 nm. Agreement of the spectral shape between theory and experiment was somewhat better than that of the Model 3600 APM.

These analyses show that the performance in classifying particle mass of the compact APM operated at the aerosol flow rate of 0.3 L/min is approximately the same as that of the Model 3600 APM operated at 1.0 L/min. With the external dimensions of the electrodes being 140 mm in length and 60 mm in diameter, the new compact model of APM can be adopted easily to field measurements.

3.5 References

[1] Hagwood, C., Coakley, K., Negiz, A. and Ehara, K. Stochastic modeling of a new spectrometer. *Aerosol Sci. Technol.* (1995) 23, 611-627.

[2] Sakurai, H., Ehara, K., Tajima, N. and Fukushima, N. Investigation on the cause for underestimation of density measured by the DMA-APM method In *American Association for Aerosol Research 2010 annual conference*, Poster (2010).

[3] Hayashida, M. Private communication (2013).

Chapter 4

Measurements of density and porosity using DMA–APM system for high-porosity Pt/TiN nanoparticle aggregates

4.1 Introduction

The development of new materials for use in polymer-electrolyte fuel-cells (PEFCs) is important. PEFCs have become one of the most promising energy sources because they have advantages such as environmental friendliness and high efficiency. A catalyst support with high electrical conductivity and good durability is necessary for a PEFC. Carbon black is the most commonly used catalyst support material, as it has desirable characteristics such as high electronic conductivity and a high surface area [1-6]. However, the durability of a carbon-based catalyst is relatively low because carbon is thermodynamically unstable under highly acidic PEFC operating conditions [7, 8]. Alternative materials with high porosities, high electronic conductivities, and acid resistance are therefore needed to replace carbon supports.

Titanium nitride (TiN) is known to have excellent resistance under acidic conditions. Furthermore, the electronic conductivity of TiN has been reported to be comparable to or even higher than that of carbon black [9]. Recently, Kakinuma et al. succeeded in producing TiN-supported platinum (Pt/TiN) catalyst nanoparticles using an ex situ method [10]. The prepared Pt/TiN catalyst had good durability. However, the electrochemical performance was unsatisfactory. In order to increase the electrochemical performance, Pt/TiN was restructured into a packed form using acetylene black, which naturally has an agglomerated structure. This strategy improved the electrochemically active surface area. However, acetylene black itself is a carbon black, and is unstable under acidic conditions, which therefore again leads to durability issues. The development of a strategy for producing aggregated Pt/TiN without using carbon black is challenging.

An oxide layer of TiN nanoparticles and incomplete Pt reduction are also reasons for the low electrochemical performances of Pt/TiN catalysts. As is widely known, the outer surfaces of TiN nanoparticles are easily oxidized, and this influences the interactions of Pt nanoparticles with a TiN catalyst support, and decreases the catalyst activity. However, this issue has not yet been specifically addressed. In this work, the effect of the addition of formic acid (HCOOH) as a reducing agent to the precursor was evaluated in detail. Wang et al. found that HCOOH can efficiently reduce Ni nanoparticle surfaces in spray pyrolysis [11].

Balgis et al. have also reported the effect of catalyst support morphologies on electrocatalytic performances, using a self-assembly-assisted spray pyrolysis method [12-15]. Self-assembly-assisted spray pyrolysis is a promising method for the design of nanostructured particles. This method efficiently produces a dry powder from a nanoparticle sol and precursor solution, and has potential advantages for many applications [16, 17]. The obtained nanoparticle aggregates are on the sub-micrometer scale, and are easier to handle than nanoparticles. In particular, sub-micrometer- or micrometer-scale catalysts with controlled morphologies give better transport of reactants and products from the active catalytic sites to the bulk of the fluid than is obtained with nanometer-scale catalysts.

Based on this background, in this chapter, I describe self-assembly-assisted spray pyrolysis for the preparation of Pt/TiN nanoparticle aggregate catalysts with high porosities. The porosities and densities of the TiN nanoparticle aggregates were measured by in situ aerosol technology using a DMA-APM system. To the best of my knowledge, this is the first examination of the physical properties of TiN nanoparticle aggregates in suspension. Given the important role that such particles play in many industrial materials applications, I believe that the evaluation of the physicochemical properties of nanoparticle materials is of great importance.

4.2 Experimental

Figure 4.1 shows the overall experimental procedure for the synthesis of Pt-deposited TiN (Pt/TiN) nanoparticle aggregates by self-assembly-assisted spray pyrolysis. Details of the procedure are as follows. 1) TiN nanoparticles were mixed with an $H_2PtCl_6·6H_2O$ precursor solution. 2) The obtained solution was sprayed using an ultrasonic nebulizer. 3) The generated droplets were introduced into a multi-stage furnace for self-organization of the TiN nanoparticles, followed by thermal decomposition of the Pt precursor for Pt nanoparticle deposition on the TiN nanoparticle aggregates. 4) The synthesized particles were collected using an electrostatic precipitator in order to determine their particle morphologies, crystal structures, chemical components, electronic structures, and catalytic activities as shown in Figure 4.1a. The effective densities and porosities of the synthesized nanoparticle aggregates were also investigated by in situ aerosol technology using a DMA–APM system, as shown in Figure 4.1b.

4.2.1 Preparation of Pt/TiN catalyst

TiN nanoparticles synthesized using a plasma process (Nishin Engineering Inc., Tokyo, Japan) and an $H_2PtCl_6·6H_2O$ dispersion were used as the starting solution. All of chemical materials used in this work were dispersed in ultrapure-water. The Pt/TiN nanoparticle aggregates were synthesized using a self-assembly-assisted spray pyrolysis process. The spray pyrolysis apparatus consisted of an ultrasonic nebulizer (1.7 MHz, NE-U17, Omron Healthcare Co., Ltd., Kyoto, Japan) for droplet generation and an electrical tubular furnace that had two temperature zones, namely 120 °C and 600 °C, as shown in Figure 4.2 [18]. In the low-temperature zone, the solvent evaporated from the droplets, generating a composite of TiN nanoparticles and Pt ions (Pt precursor). In the high-temperature zone, the Pt ions were reduced. The precursor contained a mixture of a 0.5 wt% TiN nanoparticle dispersion solution and an 8.0 wt% $H_2PtCl_6·6H_2O$ dispersion; the theoretical amount of added Pt was 20 wt%, based on TiN, and was used in the generation of Pt/TiN nanoparticle aggregate samples without HCOOH, denoted by $Pt/TiN_{w/o\text{-}HCOOH}$. The samples with HCOOH, denoted by $Pt/TiN_{w/HCOOH}$, were obtained

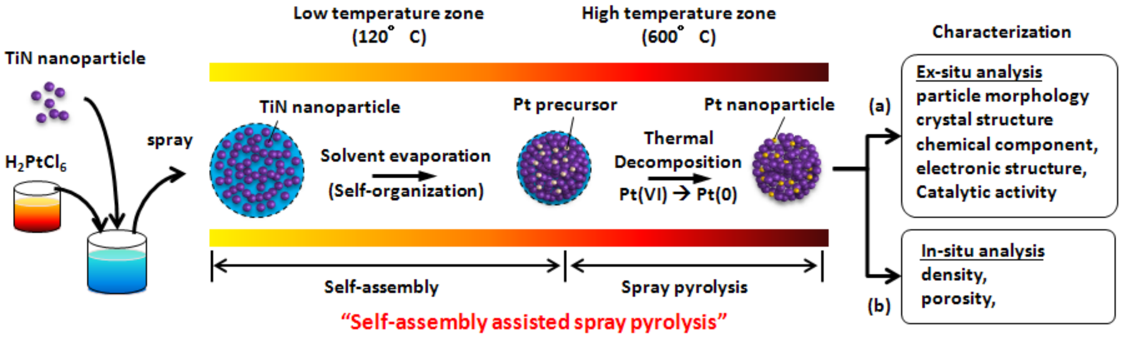

Figure 4.1 Overall experimental procedure for synthesis of Pt-deposited TiN aggregates by self-assembly-assisted spray pyrolysis.

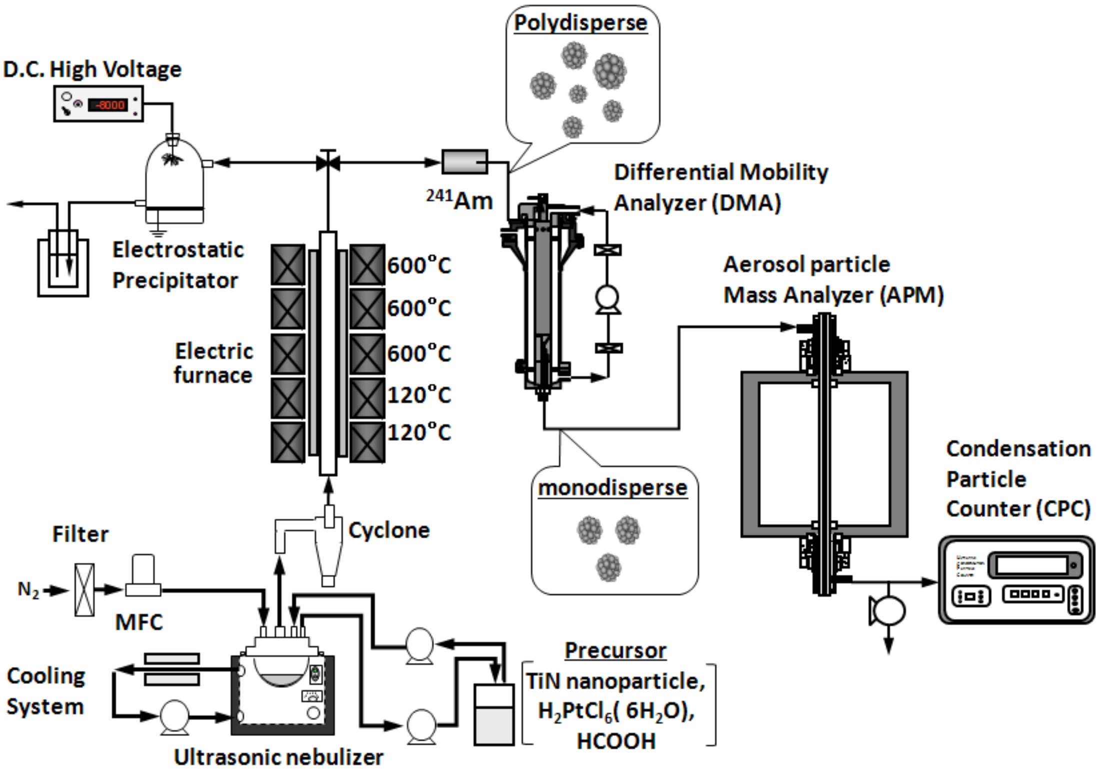

Figure 4.2 Schematic diagram of the experimental setup.

by adding 0.6 wt% HCOOH, based on the TiN dispersion solution, to the precursor. HCOOH was used to simultaneously reduce the oxygen bonded on the TiN surfaces and Pt ions to Pt nanoparticles.

4.2.2 Density and porosity characterization

The porosities of the TiN nanoparticle aggregates were obtained from density measurements. The prepared aggregates were directly passed through a density measurement system. This system consisted of a DMA (Model 3081, TSI Inc., Minneapolis, USA), an APM Model 3600 and a CPC (Model 3022, TSI Inc., Minneapolis, USA), as shown in Figure 4.2. The function of the DMA and APM were explained in our previous work [19]. The APM classifies particles based on the mass-to-charge ratio. The particle mass, at which the centrifugal force acting on a particle at the radial distance r_c balances with the electrostatic force, is given by

$$m_c = \frac{eV}{r_c^2\,\omega^2\,ln(r_2/r_1)}, \tag{4.1}$$

where e is the elementary charge, V the voltage between the electrodes, ω the rotational speed, r_1 and r_2 are the inner and outer radius of the electrode gap, and $r_c = (r_1 + r_2) / 2$.

The particle effective density, ρ, is obtained from both the electrical mobility equivalent diameter, d_{me}, measured by the DMA, and the mass, m_c, measured by the APM, using the following equation:

$$\rho = m\Big/\left(\pi d_{me}{}^{3}/6\right). \tag{4.2}$$

TiN nanoparticle aggregates of diameter 350 nm, classified using the DMA, were introduced into the APM to obtain their effective densities. The particle porosity is defined as the pore space in a particle, and can vary from 0 to 100%. The particle porosity is stated as:

$$\phi = 1 - \frac{\rho}{\rho_{true}} \tag{4.3}$$

where ρ is the effective density of the generated particles, measured using the DMA–APM method, and ρ_{true} is the true density of the dense particles.

Catalyst porosity is one of the most important factors in electrocatalytic performance. The higher the catalyst porosity is, the better the three-boundary phase among the catalyst, gas phase, and electrolyte will be. This permeable layer allows effective gas/water diffusion and proton/electron transport to and from the catalytic sites. Although, nitrogen adsorption/desorption is the method commonly used to measure particle density, a large amount of sample is necessary for measurements using this method, and this is a problem when dealing with small rate of samples production. Measurements of particle effective densities using the DMA−APM method, which only needs a small amount of sample and can be performed in situ, is preferable for particles prepared by some methods. If the theoretical density of the particle is known, the particle porosity can be calculated using Equation 4.3.

4.2.3 Pt/TiN material characterization

The morphologies of the catalyst particles were observed using field-emission scanning electron microscopy (FE-SEM; Hitachi, S-5000, 20 kV) and transmission electron microscopy (TEM; JEOL-JEM-2010, 200 kV). TEM observations were also used for chemical mapping of catalyst particles, which shows the elements contained in the particles and their dispersion patterns. The electronic structures of the TiN nanoparticles were observed using X-ray absorption fine-structure (XAFS) spectroscopy. Measurements were conducted at the BL27SU line in the Japan Synchrotron Radiation Research Institute (JASRI) in Hyogo, Japan. The crystal structures were determined using X-ray diffraction (XRD, Rigaku, RINT2000). The Pt contents in the catalysts were measured using inductively coupled plasma-mass spectrometry (SII, SPS-3000).

4.2.4 Electrochemical characterization

Electrochemical characterizations of the prepared catalysts were performed using cyclic voltammetry (CV) and rotating disk electrode (RDE) measurements (Hokuto-denko, HR-301). Catalyst ink was prepared using the procedure reported elsewhere [12]. The required amount of catalyst ink was transferred to a polished glassy carbon disk (Ø = 5 mm, geometric area = 0.196 cm^2) and dried to form a thin catalyst layer. The amounts of Pt on the glassy carbon were 7.5 and 5.6 μg-Pt/cm^2 for the Pt/TiN catalysts without and with the addition of HCOOH, respectively. The measurements were performed at room temperature (~25 °C) using a freshly prepared 0.1 M $HClO_4$ electrolyte solution (Cica-reagent, Kanto Chemical Co., Inc., Japan). A nitrogen gas flow at 100 mL/min was passed through the electrolyte solution for 30 min before each CV measurement to deoxygenate the environment. The CV measurements were obtained by scanning between 0 and 1.2 V vs. RHE with a sweep rate of 100 mV/s. The saturating gas was switched to oxygen for the RDE measurements, and the electrolyte was saturated using the same conditions as those for the CV measurements. The rotation rates were controlled at 400, 900, 1600, 2500, and 3600 rpm to collect data for Koutecký−Levich plots. Measurements were carried out at 10 mV/s sweep rates in a typical polarization program of 0.2 V → 1.2 V. The background current was measured by running an oxygen-reduction reaction (ORR) sweep profile, without any rotation, in nitrogen-gas-purged 0.1 M $HClO_4$ before the ORR measurement to eliminate any contributions from capacitive current.

4.3 Results and Discussion

4.3.1 Measurements of density and porosity using DMA–APM system

The FE-SEM and TEM images in Figure 4.3a–c show the morphological structure of the TiN nanoparticles. It can be seen that the TiN nanoparticles are cubic and of size around 40 nm; aggregate particles are formed from these nanoparticles. The cubic shape of the primary particles results in a lot of space between particles in the aggregated form; therefore, the aggregates have high porosity. The high-magnification TEM image in Figure 4.3c shows the appearance of amorphous areas on the particle surfaces, indicating that the TiN surfaces were oxidized, forming TiON.

The FE-SEM image of mono-dispersed TiN particle aggregates classified as 350-nm particles using DMA is shown in Figure 4.4. The obtained aggregates were spherical although they consisted of cubic primary particles. This figure also shows the

APM system response spectrum that plots APM outlet concentration as a function of response voltage. The APM rotational speed was kept constant at 1500 rpm, and the peak response voltage that corresponded to the maximum APM outlet concentration of the 350-nm TiN particles was 458.0 V. This voltage corresponds to a measured density of 1292.2 kg/m^3, calculated using Equation 4.1 and Equation 4.2. The measured density of the TiN nanoparticle aggregates was much less than that of the theoretical (bulk) density of TiN, 5400 kg/m^3, which indicates that in the TiN nanoparticle aggregates, there are many empty spaces among the primary particles. The porosity of the aggregate particles, calculated using Equation 4.3 was 76.21%.

Figure 4.5 shows XAFS spectra of TiN and TiO_2 samples. Unlike other analytical methods, XAFS analysis can detect specific elements in the particle surface and the bulk form, and these are shown as a total electron yield [Figure 4.5a and 4.5b] and fluorescence yield [Figure 4.5c and 4.5d], respectively. The Ti 2p XAFS spectra of a TiN sample in the surface and in the bulk are shown in Figure 4.5a and 4.5c. TiO_2 particles were also investigated under the same conditions to examine the oxidation level of the TiN sample. The spectra show a complex structure split by a spin–orbit interaction of the Ti 2p levels, with two main features at around 460 and 465 eV. The spectrum of the TiN surface shows rather sharp structures similar to those of the TiO_2 spectra; these are characteristic of transition-metal oxides with large intra-atomic interactions. This provides evidence of the formation of TiO_2 on the surfaces of the TiN nanoparticles. The Ti 2p XAFS spectrum of bulk TiN presents a much broader structure and is different from that of the TiO_2 spectrum. This spectrum corresponds to the previously reported spectrum of TiN [20].

4.3.2 Morphological characteristics of Pt/TiN catalysts

The morphology of the Pt/TiN catalyst prepared with the addition of HCOOH is presented in Figure 4.6a and 4.6b; the figure shows that the prepared catalyst had a spherical aggregate morphology with many pores on the surface. Figure 4.6c shows the chemical mapping of Pt/$TiN_{w/HCOOH}$; it can be seen that Pt nanoparticles, represented in

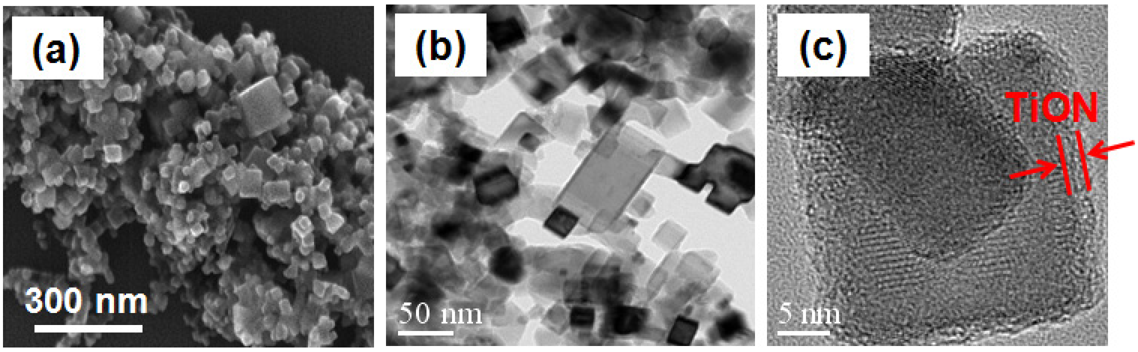

Figure 4.3 (a) SEM image and (b) TEM image of TiN nanoparticles, and (c) HR-TEM image of single-crystal TiN nanoparticles.

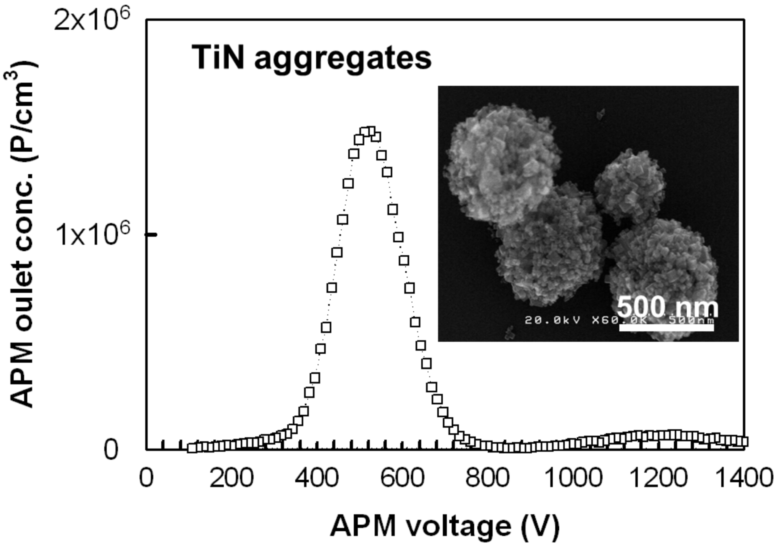

Figure 4.4 SEM image and APM outlet concentration as a function of response voltage of 350-nm TiN.

yellow, were dispersed uniformly on the TiN surface. A detailed examination of the Pt nanoparticle dispersion was performed using TEM, and the image is shown in Figure 4.7a. The image confirms a homogeneous distribution of Pt nanoparticles of average size 2.15 nm, as shown in the histogram in Figure 4.7b. In the catalyst formation process, HCOOH addition is the first step in Pt ion reduction and oxygen reduction on the surfaces of the TiN nanoparticles. The completion of Pt ion reduction to Pt nanoparticles was achieved simultaneously with the formation of catalyst particles, using a spray pyrolysis process. Pt nanoparticles are trapped between compacted TiN nanoparticles, inhibiting Pt particle growth. These phenomena explain the formation of well-dispersed and agglomeration-free Pt nanoparticles.

Figure 4.8 shows the XRD patterns of $Pt/TiN_{w/o\text{-}HCOOH}$ and $Pt/TiN_{w/HCOOH}$. The diffraction peaks of Pt were observed at 39°, 46°, and 68° (2θ), corresponding to the (111), (200), and (220) crystalline planes, respectively (JCPDS Card no. 4-0802), with a face-centered-cubic crystal structure. The XRD patterns also had sharp peaks at around 36°, 42°, 61°, 74°, and 78° (2θ), which correspond to the diffraction peaks of highly crystalline TiN. It is clear that the reduction of $H_2PtCl_6{\cdot}6H_2O$ and the oxidized surfaces of TiN by high-temperature spray pyrolysis was achieved under a nitrogen atmosphere. The addition of HCOOH plays an important role in the TiN crystallinity. The TiN crystal intensity obtained with the addition of HCOOH was bigger than those obtained without HCOOH addition. This is because the pre-reduction treatment using HCOOH successfully cleaned the TiN surface, leaving pure TiN particles, and, during XRD characterization, the real Ti and N atoms arrangement in the crystal can be measured without any disturbance from O atoms.

4.3.3 Electrochemical characterization of Pt/TiN catalysts

The electrochemical characteristics of the prepared Pt/TiN catalysts are presented as CV and ORR polarization curves. Figure 4.9a shows the typical hydrogen adsorption/desorption characteristics of Pt/TiN catalysts with and without the addition of HCOOH. The electrochemical surface area (ECSA) values of Pt in the working

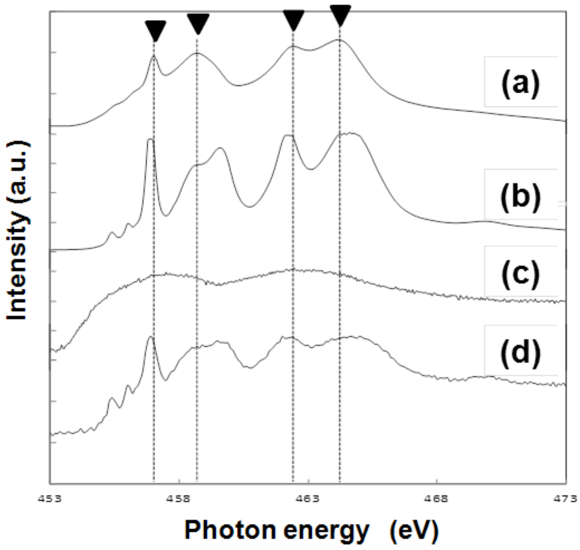

Figure 4.5 XAFS spectra of TiN and TiO2 samples: total electron yield analysis (a) TiN sample, (b) TiO2 sample; fluorescence yield analysis (c) TiN sample, (d) TiO2 sample.

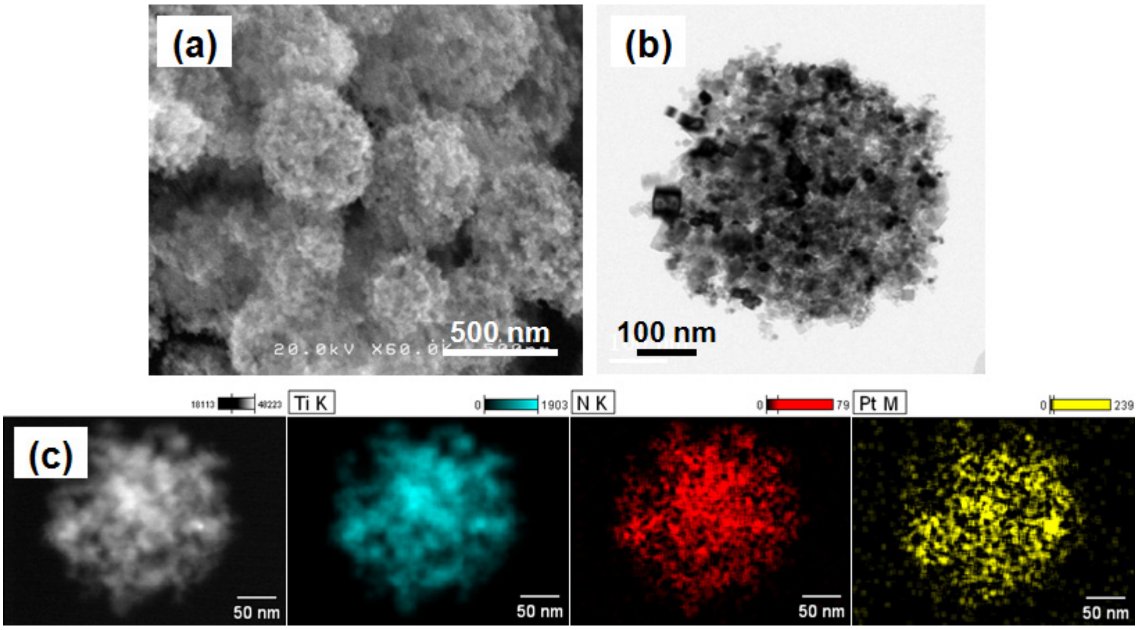

Figure 4.6 Images of Pt/TiN catalyst aggregate: (a) SEM and (b) TEM, and (c) chemical mapping of Pt/TiN catalyst.

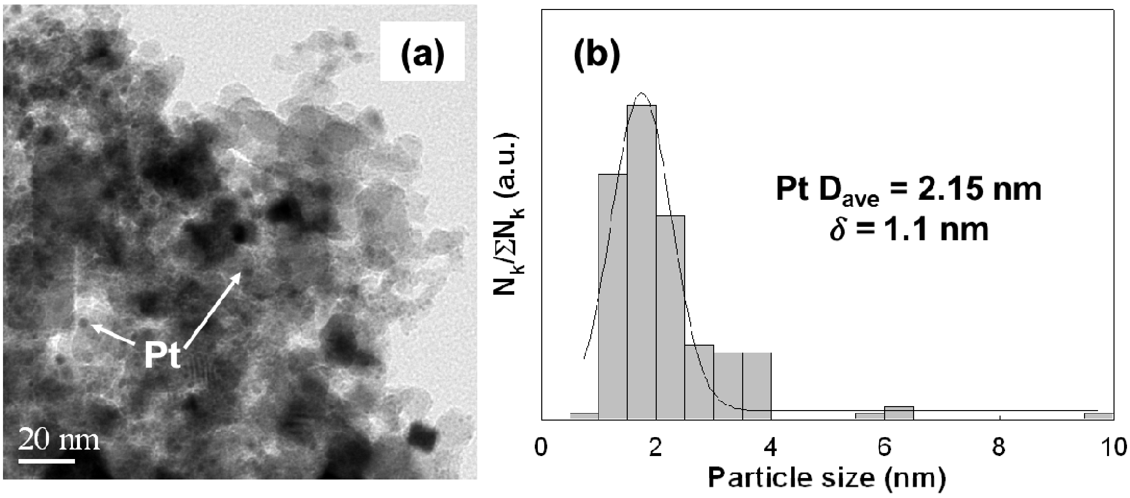

Figure 4.7 (a) Pt dispersion on TiN surface and (b) Pt nanoparticle size distribution.

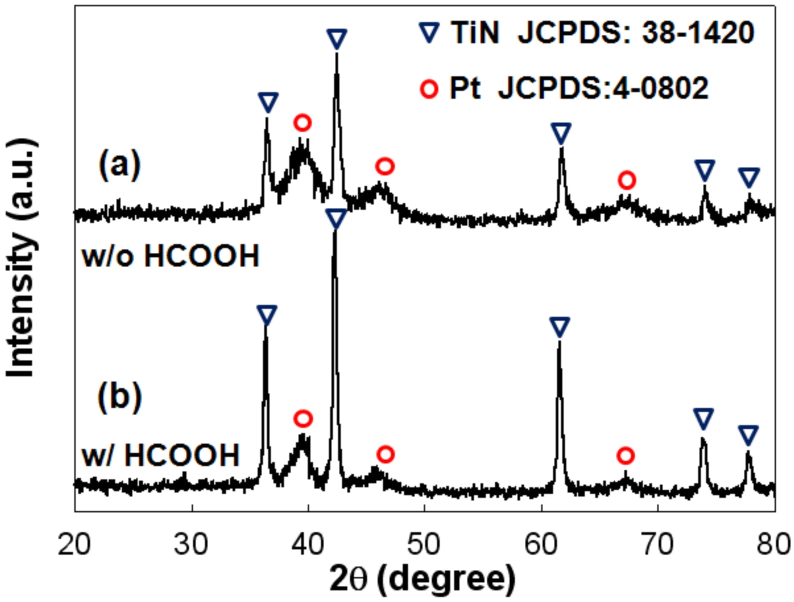

Figure 4.8 XRD patterns for Pt/TiN catalysts: (a) without HCOOH and (b) with HCOOH.

electrode were about 63.51 and 87.15 m^2/g-Pt under the initial condition (10 cycles) for Pt/$TiN_{w/o\text{-}HCOOH}$ and Pt/$TiN_{w/HCOOH}$, respectively, calculated using the hydrogen adsorption charge ($Q_{\text{H-adsorption}}$) area. Both of ECSA value for Pt/$TiN_{w/o\text{-}HCOOH}$ and Pt/$TiN_{w/HCOOH}$ were higher than that of Pt/TiN prepared via liquid phase method (58 m^2/g-Pt) under the initial condition. The ECSA value for Pt/$TiN_{w/HCOOH}$ alone was also higher than that of modified Pt/TiN which was composited with acetylene black (79.2 m^2/g-Pt).[10] The formation of self-assembly Pt/TiN nanoparticle aggregates with its well-developed agglomerate structure could support the electrical conductivity between TiN particles without sacrificing its porosity. More active Pt surface area was presented in this morphology due to the easier access of fuel gas flow through the catalyst.

The durabilities of both prepared catalysts were analyzed up to 1000 cycles, as shown in Figure 4.9b. Figure 4.9c shows that the ECSA of Pt/$TiN_{w/HCOOH}$ was more stable than that of Pt/$TiN_{w/o\text{-}HCOOH}$; the total degradation values from 10 to 1000 cycles were 36.7% and 60.9% for Pt/$TiN_{w/HCOOH}$ and Pt/$TiN_{w/o\text{-}HCOOH}$, respectively. The ECSA of Pt/$TiN_{w/o\text{-}HCOOH}$ was lower than that of Pt/$TiN_{w/HCOOH}$ as a result of incomplete Pt reduction, and of oxygen atoms remaining on the TiN surfaces; this accelerates PtO formation and lowers the electrocatalytic activity. The incomplete reduction of Pt ions also decreased the amount of active Pt catalyst, and chloride ions remaining in the catalyst could act as impurities during catalytic activity measurements. This phenomenon explains the low durability of the Pt/$TiN_{w/o\text{-}HCOOH}$ catalyst, which was twice as low as that of Pt/$TiN_{w/HCOOH}$. However, it should be noted that the appropriate amount of HCOOH is a requirement which can only be used to enhance the electrocatalytic activity. Figure 4.SI.1 (Supporting Information) shows the enhancement of CV polarization curve with the increase of HCOOH concentration from 0.15 wt% to 0.6 wt%. However, further increment of HCOOH concentration, up to 1.8 wt%, leads to the extreme degradation of catalyst performance. High amount of HCOOH increases the precursor acidity, which results in some TiN nanoparticle agglomeration and sedimentation in a precursor. This aggregated TiN nanoparticle cannot be sprayed, and the concentration of TiN nanoparticle in the droplet is decreased. As a result, during

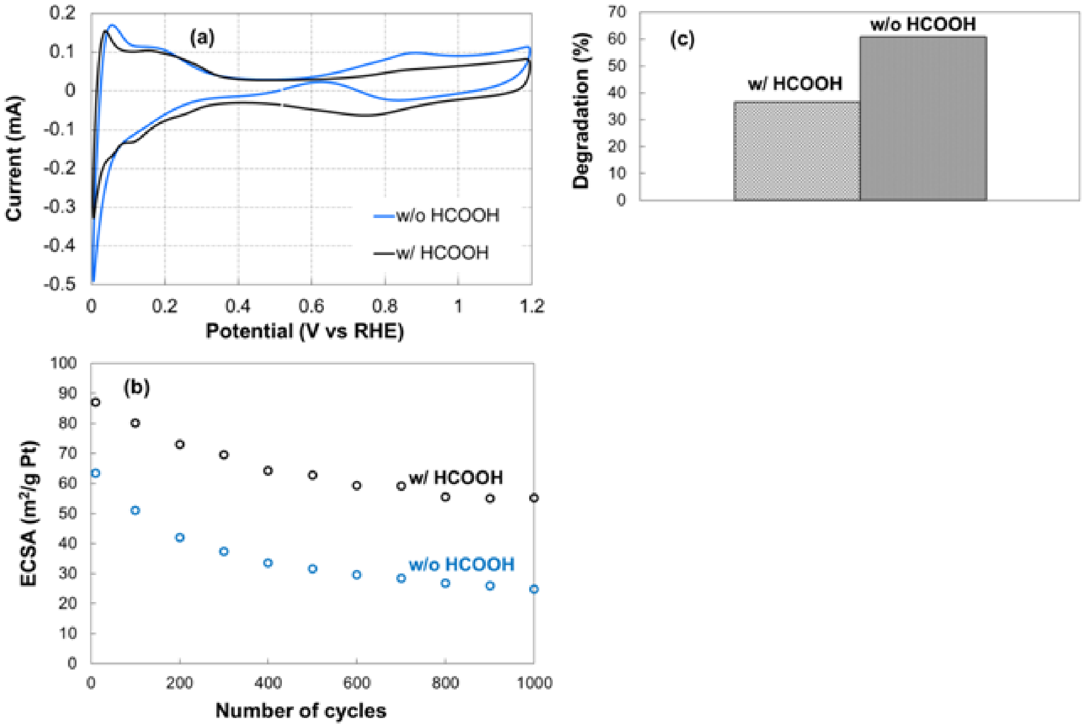

Figure 4.9 (a) Cyclic voltammograms of Pt/TiN catalysts with and without HCOOH, for 10 cycles in oxygen-free 0.1 M HClO4 (cycling between 0 and 1.2 V at 100 mV/s sweep rate), (b) change in ECSA as a function of number of cycles, and (c) ECSA degradation rates for catalysts.

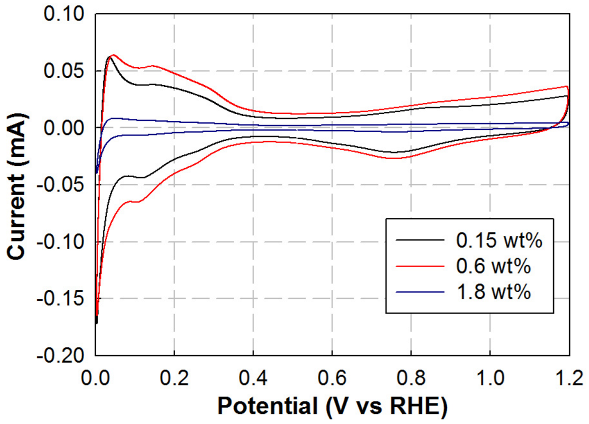

Figure 4.SI.1 Cyclic voltammograms of Pt/TiN catalysts with the addition of various concentration of HCOOH, for 3 cycles in oxygen-free 0.1 M HClO4 (cycling between 0 and 1.2 V at 50 mV/s sweep rate).

reduction process, the Pt nanoparticles tend to agglomerate on the surface of small size of TiN nanoparticle aggregates, due to the smaller surface area. It shows that the optimum concentration of HCOOH for enhancing the electrocatalytic performance was existed.

The ORR polarization curves of Pt/TiN$_{w/HCOOH}$ and Pt/TiN$_{w/o\text{-}HCOOH}$ recorded at different rotational speeds are shown in Figure 4.10a and 4.10b, respectively; these were used to obtain Koutecký–Levich plots. The target potential for the calculation of the mass activity and specific activity was E = 0.85 V. The mass activity and specific activity were evaluated from the Koutecký–Levich plots using the limiting current method. The Pt mass activity values were calculated by normalizing the Pt loading of the disk electrode, and the specific activity values were estimated by calculating the mass–specific activities and normalizing them to the Pt ECSA. The mass activity values of the Pt/TiN$_{w/HCOOH}$ and Pt/TiN$_{w/o\text{-}HCOOH}$ catalysts under the initial conditions (10 cycles) were 496.90 and 224.51 mA/mg-Pt, respectively, whereas their specific activity values were 570.14 and 353.52 μA/cm^2-Pt, respectively, as summarized in Table 4.1. The mass and specific activities of the Pt/TiN$_{w/HCOOH}$ catalyst were higher than those of Pt/TiN$_{w/o\text{-}HCOOH}$ after the stability tests (1000 cycles). The ORR currents were degraded by 79.5% and 86.8% for Pt/TiN$_{w/HCOOH}$ and Pt/TiN$_{w/o\text{-}HCOOH}$, respectively, as shown in Figure 4.10c. From the catalytic performance results, it is clear that the addition of HCOOH has a significant influence on the reduction of Pt ions and the TiN surfaces. Oxide-free TiN surfaces enhance the electrocatalytic performance. This investigation clearly indicates that the design/engineering and complete reduction of the catalyst/substrate material are very important in achieving high performance.

4.4 Conclusions

It was confirmed that the effective density of the TiN nanoparticle aggregates was 1292.2 kg/m^3 and its porosity was 76.21%. Measurements of particle effective densities using the DMA−APM method, which only needs a small amount of sample and can be performed in a short time in situ, is preferable for particles prepared by some

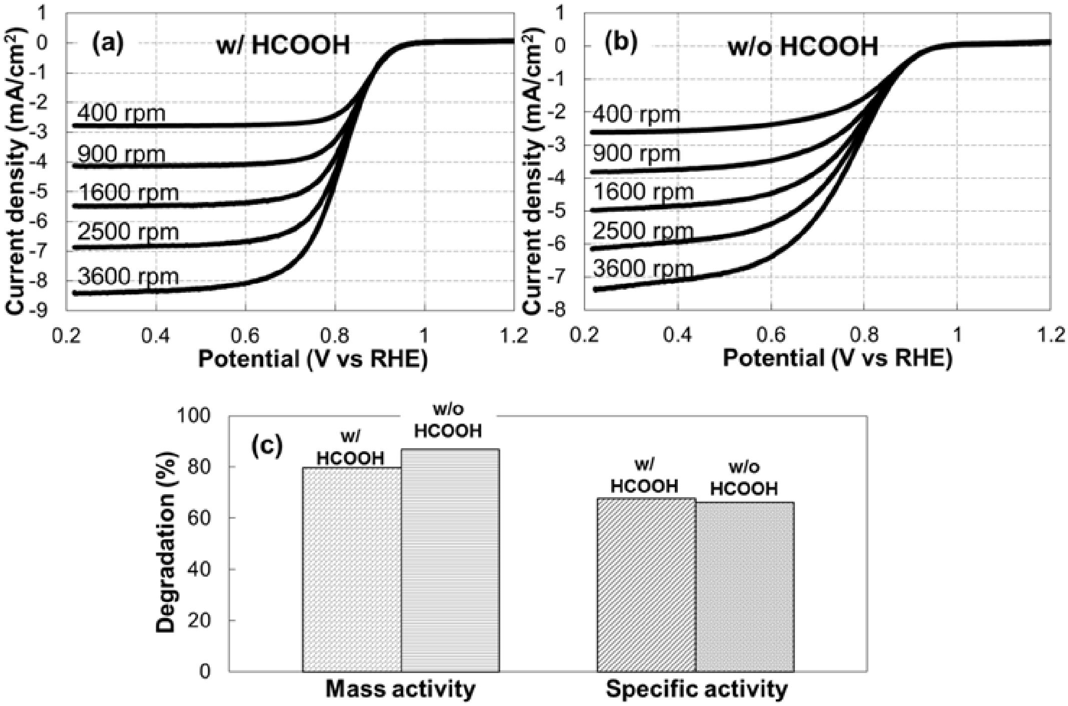

Figure 4.10 ORR polarization curves at different rotation rates for (a) Pt/TiNw/HCOOH and (b) Pt/TiNw/o-HCOOH in oxygen-saturated 0.1 M HClO4 at a sweep rate 10 mV/s, and (c) degradation rate of mass and specific activities of catalysts at 0.85 V (vs. RHE).

Table 4.1 Catalyst characterization results for Pt/TiN with HCOOH.

Sample	Pt loading (wt%)	Pt size (nm)	Pt amount on RDE (μg-Pt/cm^2)	ECSA (m^2/g-Pt)	Mass activity (mA/mg-Pt)
Pt/TiN$_{w/HCOOH}$	**15**	**3**	**5.6**	**87.15**	**496.90**
Pt/TiN$_{w/o-HCOOH}$	**19.8**	**5**	**7.5**	**63.51**	**224.51**

methods. If the theoretical density of the particle is known, the particle porosity can be calculated.

This study also demonstrated a facile strategy for controlling the morphologies of high-porosity Pt/TiN nanoparticle aggregates and simultaneously reducing Pt ions and oxidized TiN surfaces to increase the electrochemical activity of the catalyst. The addition of HCOOH increases the ECSA of the Pt/TiN catalyst to 87.15 m^2/g-Pt, and its durability is twice that of Pt/TiN without HCOOH addition. The combination of simplicity of preparation and excellent electrochemical properties make this a promising method for the preparation of carbon-free catalysts for high-performance fuel-cell applications.

4.5 References

[1] Schmidt, T. J., Noeske, M., Gasteiger, H. A., Behm, R. J., Britz, P. and Bönnemann, H. PtRu alloy colloids as precursors for fuel cell catalysts a combined XPS, AFM, HRTEM, and RDE study. *J. Electrochem. Soc.* (1998) 145, 925-931.

[2] Paulus, U. A., Endruschat, U., Feldmeyer, G. J., Schmidt, T. J., Bönnemann, H. and Behm, R. J. New PtRu alloy colloids as precursors for fuel cell catalysts. *J. Catal.* (2000) 195, 383-393.

[3] Wang, X. and Hsing, I. M. Surfactant stabilized Pt and Pt alloy electrocatalyst for polymer electrolyte fuel cells. *Electrochim. Acta* (2002) 47, 2981-2987.

[4] Prabhuram, J., Zhao, T. S., Wong, C. W. and Guo, J. W. Synthesis and physical characterization of Pt/C nanocatalyst for polymer electrolyte fuel cells. *J. Power Sources* (2004) 134, 1-6.

[5] Wang, Z. B., Zhao, C. R., Shi, P. F., Yang, Y. S., Yu, Z. B., Wang, W. K. and Yin, G. P. Effect of a carbon support containing large mesoporous on the performance of a Pt-Ru-Ni/C catalyst for direct methanol fuel cells. *J. Phys. Chem. C* (2010) 114, 672-677.

[6] Jiang, Z. Z., Wang, Z. B., Chu, Y. Y., Gu, D. M. and Yin, G. P. Ultrahigh stable

carbon riveted Pt/TiO_2-C catalyst prepared by *in situ* carbonized glucose for proton exchange membrane fuel cell. *Energy Environ. Sci.* (2011) 4, 728-735.

[7] Mitsushima, S., Koizumi, Y., Uzuka, S. and Ota, K. Dissolution of platinum in acidic media. *Electrochim. Acta* (2008) 54, 455-460.

[8] Yasuda, K., Taniguchi, A., Akita, T., Ioroi, T. and Siroma, Z. Platinum dissolution and deposition in the polymer electrolyte membrane of a PEM fuel cell as studied by potential cycling. *Phys. Chem. Chem. Phys.* (2006) 8, 746-752.

[9] Avasarala, B. and Haldar, P. Electrochemical oxidation behavior of titanium nitride based electrocatalyst under PEM fuel cell conditions. *Electrochim. Acta* (2010) 55, 9024-9034.

[10] Kakinuma, K., Wakasugi, Y., Uchida, M., Kamino, T., Uchida, H., Deki, S. and Watanabe, M. Preparation of titanium nitride-supported platinum catalyst with well controlled morphology and their properties relevant to polymer electrolyte fuel cells. *Electrochim. Acta* (2012) 77, 279-284.

[11] Wang, W. N., Itoh, Y., Lenggoro, I. W. and Okuyama, K. Nickel and nickel oxide nanoparticles prepared from nickel nitrate hexahydrate by a low pressure spray pyrolysis. *Mater. Sci. Eng. B* (2004) 111, 69-76.

[12] Balgis, R., Anilkumar, G. M., Sago, S., Ogi, T. and Okuyama, K. Nanostructured design of electrocatalyst support materials for high-performance PEM fuel cell application. *J. Power Sources* (2012) 203, 26-33.

[13] Balgis, R., Anilkumar, G. M., Sago, S., Ogi, T. and Okuyama, K. Rapid *in situ* synthesis of spherical microflower Pt/C catalyst *via* spray pyrolysis for high performance fuel cell application. *Fuel Cells* (2012) 12 (4), 665-669.

[14] Balgis, R., Iskandar, F., Ogi, T., Purwanto, A. and Okuyama, K. Synthesis of uniformly porous NiO/ZrO_2 particles. *Mater. Res. Bull.* (2011) 46, 708-715.

[15] Balgis, R., Anilkumar, G. M., Sago, S., Ogi, T. and Okuyama, K. Ultrahigh oxygen reduction activity of Pt/nitrogen-doped porous carbon microspheres prepared via spray-drying. *J. Power Sources* (2013) 229, 58-64.

[16] Pratsinis, S. E. and Vemury, S. Particle formation in gases: a review. *Powder*

Technol. (1996) 88, 267-273.

[17] Pratsinis, S. E. Aerosol-based technologies in nanoscale manufacturing: from functional materials to devices through core chemical engineering. *AIChe* (2010) 56, 3028-3035.

[18] Iskandar, F., Lenggoro, I. W., Kim, T. O., Nakao, N., Shimada, M. and Okuyama, K. Fabrication and characterization of SiO_2 particles generated by spray method for standards aerosol. *J. Chem. Eng. Jpn.* (2001) 34, 1285-1292.

[19] Lee, S. Y., Widiyastuti, W., Tajima, N., Iskandar, F. and Okuyama, K. Measurement of the effective density of both spherical aggregated and ordered porous aerosol particles using mobility- and mass-analyzers. *Aerosol Science and Technology* (2009) 43, 136-144.

[20] Soriano, L., Abbate, M., Fuggle, J. C., Prieto, P., Jimenez, C., Sanz, J. M., Galan, L. and Hofmann, S. Thermal oxidation of TiN studied by means of soft x-ray absorption spectroscopy. *J. Vac. Sci. Technol. A* (1993) 11, 47-51.

Chapter 5

Conclusions

The development and performance evaluation of aerosol particle mass analyzer (APM), and the application as aerosol measurement instrument for nanoparticle physical properties are studied. The major conclusions obtained in the thesis are as follows:

1) I inquired into the conditions that ensure good particle classification performance over a wide mass range for the first commercial model of APM (Model 3600). Experiments were also carried out to verify the validity of the theoretical considerations. In the investigation of the classifiable mass range, a boundary condition from the design specification and the λ value of the APM were determined. For balancing even better resolution and penetration, it was found that the λ value should be maintained within the range between 0.25 and 0.5. The mass range that the APM was able to cover while maintaining the λ value between 0.25 and 0.5 was from 0.003 to 2000 fg, which corresponded to the diameter range from 20 to 1600 nm if the density of particles is 1 g/cm^3.

In the experimental verification of the APM classification performance with PSL particles (density of about 1 g/cm^3), I compared mass values determined by measurement with the APM with mass values by the electro-gravimetric aerosol balance method or by estimation with size and density, and found that the values agreed with each other within 5% in the size range from 50 to 800 nm for $\lambda = 0.22$ and $\lambda = 0.49$ settings. For evaluation of the APM at smaller sizes, experiments were performed with sodium chloride particles (density of about 2 g/cm^3). It was found that the mass was accurately obtained in the size range between 30 and 200 nm, and that even at sizes as small as 12 nm the APM classification was possible. While the difference in shape between the theoretically predicted and experimentally obtained system response spectra implies that the actual transfer functions were somewhat wider and shorter than the theoretical ones, the difference was not very large at sizes of 50 nm and above. Therefore, it can be said that the optimization of the classification performance by setting the λ value within a certain range was achieved successfully. On the other hand, however, systematic underestimation of mass was observed at sizes below 30 nm for PSL, and size below 20 nm for NaCl. In addition, for particles smaller than 50 or 100 nm, the APM system response spectra were considerably wider and shorter than theoretically predicted, suggesting effects of Brownian diffusion of particles in the APM.

2) A theoretical framework was formulated that determines the design parameters of an APM which is significantly smaller than the existing Model 3600 APM and yet satisfies several performance criteria. A prototype compact APM having the design parameters determined according to this formulation was constructed, and its performance was experimentally evaluated.

The number-averaged mass of particles larger than 50 nm (approximately 0.1 fg in mass) determined experimentally was in good agreement with theoretically predicted values. The scattering of the experimentally obtained number-averaged mass around the theoretical prediction was slightly larger than that obtained with the Model 3600 APM. For particles smaller than 30 nm (approximately 0.02 fg), a systematic and significant underestimate of the number-averaged mass as compared with theoretical prediction was observed. This phenomenon was observed also for the Model 3600 APM, and regardless of the operating conditions. Although the exact reason for this phenomenon is not identified yet, a possible role of the non-sphericity of the test particles in the observed phenomenon is suggested.

The shape of the observed spectra was in excellent agreement with theoretical prediction, both in terms of their widths and heights, for particles larger than 100 nm, and in fairly good agreement for particles larger than 50 nm. Agreement of the spectral shape between theory and experiment was somewhat better than that of the Model 3600 APM.

These analyses show that the performance in classifying particle mass of the compact APM operated at the aerosol flow rate of 0.3 L/min is approximately the same as that of the Model 3600 APM operated at 1.0 L/min. With the external dimensions of the electrodes being 140 mm in length and 60 mm in diameter, the new compact model of APM can be adopted easily to field measurements.

3) As the application of APM, the effective density and porosity of nanoparticle agglomerates were measured using the DMA−APM system. It was confirmed that the effective density of the TiN nanoparticle aggregates generated using a spray-drying process was 1292.2 kg/m^3 and its porosity was calculated to be 76.21% from the effective density. Combined use of the APM and a DMA makes it possible to measure the size and mass of particles at the same time, thereby determining their effective density. It can be said that the APM is an invaluable instrument to evaluate various particle properties such as the porosity, the mass-mobility exponent, the shape factor, and the mixing ratio of internally-mixed particles.

Acknowledgement

First of all, I would like to express my sincere gratitude to my supervisor, Professor Kikuo Okuyama, Department Chemical Engineering, Graduate School of Engineering, Hiroshima University, for his continuing support both personally and professionally since I joined my company, and giving me an opportunity to learn a doctoral course in Hiroshima University.

I wish to thank you Assistant Professor Takashi Ogi, Dr. Ratna Balgis, for their support and various advice. Thanks are expressed to Professor Akihiro Yabuki, Professor Syuuji Sakohara, and Professor Tsuneji Sano for their patience, wisdom, and support as committee members of my efforts.

My deepest appreciation goes to Dr. Ehara, who is the inventor of the APM, and Dr. Sakurai, National Institute of Advanced Industrial Science and Technology, for their insightful discussions, comments and suggestions on the design and evaluation in the development of APM. They also offered me valuable, detailed advice and guidance during the writing of my first and second papers. Without their support, development of APM would not have been successful.

Special thanks are sent to Emeritus Professor Hitoshi Emi and Professor Yoshio Otani, Particle processing laboratory, Kanazawa University, for their generous support and encouragement in public and private even after I graduated from their department. I was able to get involved in aerosol measurement over a long period of time. I have also received sincere encouragement from Emeritus Professor Toshiaki Yamamoto, Osaka Prefecture University.

I give recognition to Kanomax Japan Inc. and co-workers. I have been able to develop many aerosol measuring instruments, and to meet with many researchers not only in Japan but also overseas. I appreciate that I was provided with the learning opportunity of my doctoral course. Thanks are expressed to Mr. Atsuhiko Kondo, Representative Director of KONDO KO-SHA co., for his technical support and enormous contribution in the commercialization of two APMs, that I was in charge of product development.

Finally, I would like to show my cordial gratitude to my husband for his understanding and support of my university.

NAOKO HATASHITA TAJIMA

Hiroshima, September 2013